



저작자표시-비영리-변경금지 2.0 대한민국

이용자는 아래의 조건을 따르는 경우에 한하여 자유롭게

- 이 저작물을 복제, 배포, 전송, 전시, 공연 및 방송할 수 있습니다.

다음과 같은 조건을 따라야 합니다:



저작자표시. 귀하는 원저작자를 표시하여야 합니다.



비영리. 귀하는 이 저작물을 영리 목적으로 이용할 수 없습니다.



변경금지. 귀하는 이 저작물을 개작, 변형 또는 가공할 수 없습니다.

- 귀하는, 이 저작물의 재이용이나 배포의 경우, 이 저작물에 적용된 이용허락조건을 명확하게 나타내어야 합니다.
- 저작권자로부터 별도의 허가를 받으면 이러한 조건들은 적용되지 않습니다.

저작권법에 따른 이용자의 권리는 위의 내용에 의하여 영향을 받지 않습니다.

이것은 [이용허락규약\(Legal Code\)](#)을 이해하기 쉽게 요약한 것입니다.

[Disclaimer](#)

공학박사학위논문

Ph.D. Thesis

**An Experimental Study on Flame Transfer Function and
Combustion Instability Mechanism
in a Gas Turbine Combustor**

가스터빈 연소기에서 화염전달함수 및
연소불안정 발현 원인에 대한 실험적 연구

2019 년 8 월

서울대학교 대학원

기계항공공학부

주 성 필

ABSTRACT

Recently, the interests for energy depletion and rapid climate change have emerged around the world. To address the problems, the research about clean coal technology has been conducted actively. The business, which gasification accounting for a large proportion of the technology, has been performed in USA, China, Korea, etc. Gasification technology can generate synthetic gas which is spotlighted as a next generation of fuel from solid coal through carbon capture and storage technique (CCS). However, the study is still not enough to investigate the combustion characteristics. For this reason, there are many researchers studying about fuel flexibilities and combustion characteristics of the synthesis gas. In this study, combustion experiment was performed to investigate the combustion characteristics for H_2/CH_4 SNG gas in the partially premixed model gas turbine combustor equipped 1/3 scaled down GE 7EA nozzle. Chemiluminescence measurements were performed to study the flame structure and characteristics of syngas combustion over various equivalence ratio. Abel inversion method was applied to obtain 2-D chemiluminescence flame images from 3-D accumulated chemiluminescence image.

NO_x emission characteristics is similar at the same heat load because of the same Wobbe index based on higher heating values of the fuel compositions. Moreover, NO_x increases with increasing equivalence ratio and heat load. This characteristics investigate that major NO_x mechanism is thermal NO_x . CO emission rapidly peaks near stoichiometric condition and it is affected OH radical in chemical reaction. Carbon dioxide is more effective to NO_x reduction than nitrogen diluent because of its high diluent heat capacity. Combustion instability should avoid in order to prevent the combustor liner thermal and fatigue damage.

Combustion instability and emission characteristics of flames of different H_2/CH_4 compositions were investigated in a partially premixed model gas turbine combustor. A mode shift in the frequency of instability occurred under varying experimental conditions from the first to the seventh mode of longitudinal frequency in the combustor, and a parametric study was conducted to determine the reasons for this shift by using the length of the combustor, a factor that determines the mode frequency of longitudinal instability, as

the main parameter. Furthermore, heat load and fuel composition (H_2 ratio) were considered as parameters to compare the phenomenon under different conditions. The GRI-3.0 CANTERA code, OH chemiluminescence, and the Abel inversion process were applied to analyse the frequency mode shift. NO_x emissions, which occurred through the thermal NO_x mechanism, increased with increasing heat load and H_2 ratio. The instability frequency shifted from the first to the seventh mode as the H_2 ratio increased in the H_2/CH_4 mixture. However, 100% H_2 as fuel did not cause combustion instability because it has a higher burning velocity and extinction stretch rate than CH_4 . Furthermore, the laminar flame speed influenced the frequency mode shift. These phenomena were confirmed by the flame shapes. The Abel inversion process was applied to obtain the cross section of the flames from averaged OH chemiluminescence images. Stable and unstable flames were identified from the radial profile of OH concentration. The combustor length was found to not influence frequency mode shift, whereas the H_2 ratio significantly influenced it as well as the flame shape.

Combustion dynamic characteristics of hydrogen/methane flames and the flame response to fuel flow fluctuation in a model lean-direct injection gas turbine combustor. The results show that the higher frequency longitudinal thermoacoustic instability is triggered as hydrogen/methane ratios increase. The mode shift is accompanied by shortening flame length and hence decreasing convection time delay between fuel injection and flame location. Flame transfer function (FTF) subject to fuel flow rate modulation is determined over a range of frequency for hydrogen/methane volume ratios of 25:75, 50:50, and 75:25 at a fixed equivalence ratio of 0.55. The input/output function of FTF is the velocity fluctuation of fuel flow at the inlet of combustor/the heat release fluctuation of whole flame, respectively. Due to the difficulty of measuring fuel flow velocity at the inlet of combustor while flame exists, the fuel transfer function (FLTF) is measured and used along with the intermediate flame transfer function (ITF) to determine the FTF. The transfer functions are measured at frequency up to 600 Hz and the FTF above 600 Hz is determined from flame response at the higher harmonic frequency. Results of the FLTF measurement show that an acoustic resonance is formed within fuel injector and the resonance frequency changes as the hydrogen/methane ratio as well as the length of fuel feedline changes. The gain of FTF

at a given frequency decrease as the hydrogen content increases and the absolute value of the slope of phase plot which is related to the convection time delay between fuel injector tip and flame location decreases as the hydrogen enrichment ratio increases. Using the measured flame transfer function as input to an open-source code (OSCILOS), the occurrence of instability is predicted and compared with experimental results. Modelling results agree very well with experimental data in predicting the occurrence of unstable combustion, the frequency at which unstable combustion occurs and the acoustic mode inside combustor.

Keywords: Non-premixed Flame, Turbulent Flame, EINOx, Flame Stability, Flame Length, LDI combustor, Thermo-acoustic instability, PIV, OH-PLIF, Flame transfer function, OSCILOS, Higher transition, SNG Combustion.

Student Number: 2014-30362

LIST

ABSTRACT	i
LIST	iv
LIST OF FIGURES	vii
LIST OF TABLES	xi
NOMENCLATURE	xii
CHAPTER 1	
INTRODUCTION.....	1
CHAPTER 2	
EXPERIMENT AND MEASUREMENT SYSTEMS	9
2.1 Combustor and Nozzles	9
2.2 Flame Imaging	12
2.2.1 Chemiluminescence Spectroscopy	12
2.2.2 Abel Transform.....	14
2.3 Laser Diagnostics.....	15
2.3.1 OH-PLIF Measurements	15
2.3.2 PIV Measurements	20
2.4 Flame Transfer Function Measurement.....	24
2.5 Instability Prediction by 1-D Lumped Network Model.....	27
2.5.1 Combustor Geometry	28
2.5.2 Flame Position.....	29
2.5.3 Thermal Properties	32
2.5.4 Flame Model	32
2.5.5 Boundary Condition	34

CHAPTER 3	
STATIC (NO _x & FLAME STRUCTURE) CHARACTERISTICS	
OF SNG COMBUSTION	35
3.1 Background and Test Conditions	35
3.2 Emission (NO _x and CO) Characteristic of SNG Combustion without	
N ₂ and CO ₂ dilutions	38
3.3 NO _x Reduction Characteristics of SNG Combustion with	
N ₂ and CO ₂ Dilution.....	40
3.4 Dump Plane Temperature and Flame Structure.....	42
 CHAPTER 4	
HIGH FREQUENCY TRANSITION CHARACTERISTICS OF	
SYNTHETIC NATURAL GAS (H ₂ /CH ₄) COMBUSTION.....	44
4.1 Background and Test Conditions	44
4.2 Experimental Methods	48
4.3 Exhaust Gas Emission.....	50
4.4 Mode Shift Phenomenon in Combustion Instability	
with Respect to the H ₂ Ratio	53
4.5 Combustion Instability Mode Shift for Different Heat Loads	56
4.6 OH* Chemiluminescence (Flame) Characteristics.....	60
 CHAPTER 5	
THERMO-ACOUSTIC INSTABILITY AND FLAME TRANSFER	
FUNCTION MEASUREMENT	65
5.1 Background and Objectives	65
5.2 Description of Experimental and Modeling Approach.....	68
5.2.1 Model Gas Turbine Combustor and Instrumentations	68
5.2.2 Experimental Conditions	70
5.2.3 Measurement of Flame Transfer Function (FTF)	71
5.2.4 Combustion Instability Modeling	76

5.3 Results and Discussions	78
5.3.1 Characterization of Naturally Occurring Combustion Instability	78
5.3.2 Flame Transfer Function (FTF)	81
5.3.3 Modeling of Thermo-acoustic instability.....	90
5.4 Flame Structure in Flame Transfer Function.....	101
CHAPTER 6	
CONCLUSION	104
REFERENCES.....	107
ABSTRACT IN KOREAN	114

LIST OF FIGURES

Fig. 1.1	CAEP combustion technology review.	2
Fig. 1.2	Different combustion type for gas turbine combustor.	3
Fig. 2.1	Schematic diagram of the partially premixed gas turbine test facility.	9
Fig. 2.2	Schematic diagram of measurements sensor location (a) model combustor (b) cross-sectional view of fuel nozzle (c) direct photo of tested fuel nozzle.	11
Fig. 2.3	Schematic of relaxation processes emission of photons.	15
Fig. 2.4	OH excitation spectrum; In this study, $Q_1(6)$ was used for OH PLIF.	16
Fig. 2.5	OH fluorescence spectrum for $Q_1(6)$.	17
Fig. 2.6	Transmittance of filter (a) WG-305 (b) UG-11.	18
Fig. 2.7	Schematic diagram of OH-PLIF measurement system.	18
Fig. 2.8	Schematic diagram of PIV measurement system.	20
Fig. 2.9	Principle of typical PIV system.	21
Fig. 2.10	Field of view of PIV and OH-PLIF measurement.	23
Fig. 2.11	Schematic diagram of the FTF measurement system.	25
Fig. 2.12	Modulation amplitude effects on FTF characteristics.	26
Fig. 2.13	Software structure of OSCILOS.	27
Fig. 2.14	Schematic of the gas turbine combustor.	29
Fig. 2.15	Schematic of the gas turbine combustor modeling.	29
Fig. 2.16	Average flame image measured by the OH chemiluminescence.	30
Fig. 2.17	Average flame image measured by the OH-PLIF.	31
Fig. 2.18	(a) Velocity, and (b) temperature for 25% H_2 , 75% CH_4 fuel composition.	32
Fig. 2.19	FTF for 25% H_2 , 75% CH_4 fuel composition.	34
Fig. 3.1	NO_x emission characteristics of SNG combustion without N_2 and CO_2 diluents with hydrogen compositions. (a) 25.4kW, (b) 38.1kW, (c)	38

50.8kW, (d) 63.5kW.

Fig. 3.2	NO _x reduction with diluent of N ₂ and CO.	40
Fig. 3.3	NO _x reduction with respect to the diluent heat capacity of N ₂ and CO ₂ .	41
Fig. 3.4	Dump plane temperature on combustion instability.	42
Fig. 4.1	Time-averaged OH chemiluminescence and Abel-inverted image at a heat load of 40 kW, H ₂ ratio of 75%, and combustor length of 1,400 mm.	50
Fig. 4.2	Characteristics of eiNO _x emission with respect to H ₂ ratio and heat load.	51
Fig. 4.3	(a) Mode analysis based on the amplitude of a dynamic sensor, and (b) flame structure with respect to H ₂ /CH ₄ ratio and combustor length at a heat load of 40 kW.	53
Fig. 4.4	Frequencies of combustion instability for various combustor lengths with a heat load of 35 kW and H ₂ ratio of 37.5%.	55
Fig. 4.5	(a) Mode analysis based on the amplitude of a dynamic sensor with respect to the heat load, and (b) a detailed view of the combustion instability of the 4 th mode of longitudinal frequency.	56
Fig. 4.6	Length and structure of the flame at varying heat loads (35, 40, and 45 kW).	58
Fig. 4.7	Instability frequency with respect to the speed of the laminar flame for different (a) H ₂ ratios and (b) heat loads	59
Fig. 4.8	(a) Flame-structure characteristics between CH ₄ and H ₂ flames (b) Time-averaged OH*chemiluminescence and Abel-inverted images at a combustor heat load of 40 kW and a length of 1,400 mm.	60
Fig. 4.9	Radial profiles of OH radical concentrations of the flame at a combustor length of 1,400 mm for H ₂ ratios of (a) y = 8 mm, (b) y = 11 mm, and (c) y = 14 mm.	62
Fig. 4.10	Radial profiles of OH concentration of the flame for different H ₂ ratios at y = 11 mm from the dump plane. (a) H ₂ ratio = 50%, (b) H ₂ ratio = 100%.	63
Fig. 4.11	Average error of the radial profiles of OH concentrations of flame for	64

	different H ₂ ratios at y = 11 mm from the dump plane.	
Fig. 5.1	(a) Schematic of model gas turbine combustor and sensor position and (b) lean direct injector (LDI).	68
Fig. 5.2	Schematic of experimental setup for flame transfer function. (a) open boundary gas turbine combustor, (b) flame transfer function setup.	71
Fig. 5.3	Summation of OH* intensity of the flame with respect to the equivalence ratio for direct injection.	71
Fig. 5.4	Schematic of experimental setup for fuel transfer function (FLTF).	72
Fig. 5.5	(a) Block diagram and (b) input/output parameters of the relationship between ITF, FLTF and FTF.	73
Fig. 5.6	Schematic of the acoustic multi elements for OSCILOS.	76
Fig. 5.7	Flame characteristics (a) Time-averaged OH-PLIF images with respect to H ₂ /CH ₄ composition (upper side), (b) Phase-locked instantaneous OH-PLIF images for H ₂ /CH ₄ ratios of 25:75, 50:50, and 75:25.	79
Fig. 5.8	Combustion instability (a) amplitude, (b) frequency with respect to various parametric conditions, and (c) pressure spectrum for H ₂ /CH ₄ ratios of 25:75, 50:50, and 75:25.	80
Fig. 5.9	Combustion instability amplitude in acoustically open boundary.	81
Fig. 5.10	Gain and phase of intermediate transfer function (ITF) with respect to the H ₂ /CH ₄ composition.	82
Fig. 5.11	Gain and phase of fuel transfer function (FLTF) with respect to the H ₂ /CH ₄ composition.	84
Fig. 5.12	Schematic of the fuel feedline and siren (top) and pressure wave mode shape (bottom).	85
Fig. 5.13	(a) Schematic of FLTF measurement setup and fuel feeding line and (b) the effect of feeding-line length on FLTF gain.	87
Fig. 5.14	Gain and phase of FTF with respect to the H ₂ /CH ₄ composition.	88
Fig. 5.15	Simplified combustor dimension in OSCILOS.	90
Fig. 5.16	(a) Axial heat release of the OH-intensity distribution and (b) Flame	92

length with respect to the H_2/CH_4 composition.

- Fig. 5.17 FFT result of raw data by location in high modulation frequency modes using higher harmonic responses of ITF and FLTF at $H_2:CH_4 = 25:75$, 500 Hz fuel modulation: 94
- (a) velocity fluctuation of ITF measured at HWA#1,
 - (b) OH-chemiluminescence fluctuation of ITF measured at PMT,
 - (c) velocity fluctuation of FLTF measured at HWA#2, and
 - (d) velocity fluctuation of FLTF measured at HWA#2.
- Fig. 5.18 $Gain_{FTF}$ and $phase_{FTF}$ from experimental data (line), higher harmonic response in fuel modulation (dot) and linear curve fitting (dash line). 95
- Fig. 5.19 Comparison of experimental results and prediction of pressure mode shape. (a) $H_2:CH_4 = 25:75$, (b) $H_2:CH_4 = 50:50$, and (c) $H_2:CH_4 = 75:25$ 98
- Fig. 5.20 Phase-locked instantaneous velocity field mapped with OH-PLIF images. 101
- Fig. 5.22 Schematic of attribution for fluctuated flame structure. 101

LIST OF TABLES

Table 1.1	Categorized combustion instability prediction research.	6
Table 2.1	Formation and destruction of OH radical.	15
Table 2.2	High-speed PLIF application research summary.	19
Table 2.3	Summary of flow modulation device and application.	24
Table 2.4	Prediction of instability frequency according to the flame position.	31
Table 3.1	Combustor load test condition	37
Table 3.2	Diluent specific heat on 500K	41
Table 3.3	Abel-inversed OH-chemiluminescence images in 63.5kW heat load without dilution.	43
Table 4.1	Experimental test conditions.	48
Table 5.1	Experimental test conditions.	70
Table 5.2	Comparison between calculated quarter wave frequency and measured frequency of peak gain _{FLTF} at 600 mm fuel feedline.	85
Table 5.3	Comparison between measured and calculated quarter wave frequency with respect to the fuel feedline at H ₂ :CH ₄ =25:75.	88
Table 5.4	Density ratio in the fuel feedline and combustion zone with respect to the fuel composition.	89
Table 5.5	Phase slope gradient and time delay of FTF with respect to fuel composition.	89
Table 5.6	Inlet thermal properties for longitudinal mode in OSCILOS	93
Table 5.7	Estimation results (Eigen frequency and growth rate) of OSCILOS with respect to the H ₂ :CH ₄ ratio using FTF.	97
Table 5.8	Comparison between FTF combustion instability frequency prediction and experimental instability frequency.	97

Table 5.9	Estimation results (Eigen frequency and growth rate) of OSCILOS with respect to the H ₂ :CH ₄ ratio using ITF.	99
Table 5.10	Comparison between ITF combustion instability frequency prediction and experimental instability frequency.	100

NOMENCLATURE

Alphabet

A_0	averaged flame area
A_T	wrinkled flame area
D	diffusivity
Da	Damkohler number
d_a	diameter of coaxial nozzle
d_f	diameter of fuel nozzle
d_f^*	effective diameter of jet, $m/(\pi\rho_a J/4)^{1/2}$
$EINO_x$	emission index of nitrogen oxides
Fr_f	characteristic fuel jet Froude number
f_{st}	stoichiometric air-fuel mass ratio, $(m_a/m_f)_{st}$
g	gravitational acceleration
J	jet momentum flux, $\Sigma\rho U^2$
L	flame length
l	rim thickness of fuel nozzle
m	jet mass flowrate, $\Sigma\rho U$
m_a	air mass flowrate
$m_{a,st}$	stoichiometric air mass flowrate corresponding to m_f
m_f	fuel mass flowrate
m_{N_2}	nitrogen mass flowrate
m_{NO_x}	mass production rate of NO _x
MW	molecular weight
r	radial distance
Re_a	coaxial air Reynolds number, $U_a\{d_a-(d_f+2l)\}/2\nu_a$
Re_f	fuel Reynolds number, $U_f d_f/\nu_f$
S_I	extensive principal strain rate
$S_{NO}(Z_b)$	maximum reaction rate
S_{rx}	shear strain rate, $1/2(\partial U_r/\partial x + \partial U_x/\partial r)$

$S_{u,max}$	maximum laminar flame speed
T_{st}	stoichiometric flame temperature
T_{∞}	ambient temperature
U_a	bulk exit velocity of coaxial nozzle
$U_{a,bo}$	detachment velocity of coaxial air
U_{co}	coflow air velocity
U_f	bulk exit velocity of fuel
$U_{f,c}$	critical fuel jet velocity
U_r	r -direction component of velocity
U_s	stoichiometric mixture axial velocity, $Z_s U_f + (1-Z_s) U_a$
U_x	x -direction component of velocity
V	flame volume
x	axial distance
Z	mixture fraction, $m_f/(m_a+m_f)$
Z_s	stoichiometric mixture fraction
IGCC	Integrated gasification combined cycle
IGFC	Integrated Gasification Fuel Cell
MFC	Mass flow controller
OECD	Organization for Economic Co-operation and Development
PLIF	Planar Laser Induced Fluorescence
PIV	Particle Image Velocimetry
PMT	Photon multiplier tube
RMS	Root Mean Square
SNG	Synthetic Natural Gas
FTF	Flame transfer function
ITF	Intermediate flame transfer function
FLTF	Fuel line transfer function
POD	Proper orthogonal decomposition
DMD	Dynamic mode decomposition

Greek

α	thermal diffusivity
δ_{OH}	OH layer thickness
λ	wavelength
μ_a	viscosity of air
μ_f	viscosity of fuel
ν_a	kinematic viscosity of air
ν_f	kinematic viscosity of fuel
ρ_a	air density
ρ_f	fuel density
ρ_∞	ambient gas density
Φ_G	global equivalence ratio, $(m_a/m_f)_{st}/(m_a/m_f)$
χ	scalar dissipation rate
χ^{NOx}	NOx concentration

Subscript

a	air
f	fuel
st	stoichiometric
∞	ambient

CHAPTER 1

INTRODUCTION

Gas turbine engines consist of compressors, combustors, and turbines. Combustion engines are a key part of the engine's eco-friendliness. Especially, it is difficult to install additional air pollutant abatement equipment due to various constraints such as space and weight. Therefore, it is necessary to develop eco-friendly combustion technology that can minimize the emission of air pollutants. Regulations on engine emissions are intensifying as the global awareness of the need for air pollution increases. For airplanes, regulations on major air pollutants such as NO_x were issued by the Committee on Aviation Environmental Protection (CAEP) of the International Civil Aviation Organization (ICAO) have been established and applied (CAEP/2, CAEP/4, CAEP/6, CAEP/8 and so on). Recently, more stringent CAEP/8 regulations were applied to aircraft engines with a thrust of 26.7 kN or more, which are small and medium-sized. Therefore, in order to enter the civil engine market, it is essential to develop combustor technology that meets environmental regulations. In CAEP/2, revised in 1996, NO_x emissions were reduced by 20%, with CAEP/4 (16% in 2004, CAEP/6 in 2008 and 12% in 2008) [1]. Therefore, NASA is strongly promoting the development of next-generation combustion technology to reduce NO_x emissions significantly compared to the current standards, and is supporting project costs for GE aviation and Pratt & Whitney [2–6].

In recent years, many energy consumption, higher ozone concentration and average temperature interest are the issue for many research group [7]. Actually, lots of researches have been conducted to reduce NO_x emissions, increased combustion efficiency and developed alternative clean fuel. Meanwhile, energy production industry have hailed these technology, especially synthetic gas and natural gas market share are on the rise widely. However, the application of using the new fuel is necessary to change the design of the combustion system, and therefore previous research and such basis is need because operation mode and combustion characteristics vary with fuel composition. In this study,

prior to the application of this new fuel in gas turbine combustor, combustion characteristics should be understood to be stable operation and increase performance by revealing the significant operational problems at early stage.

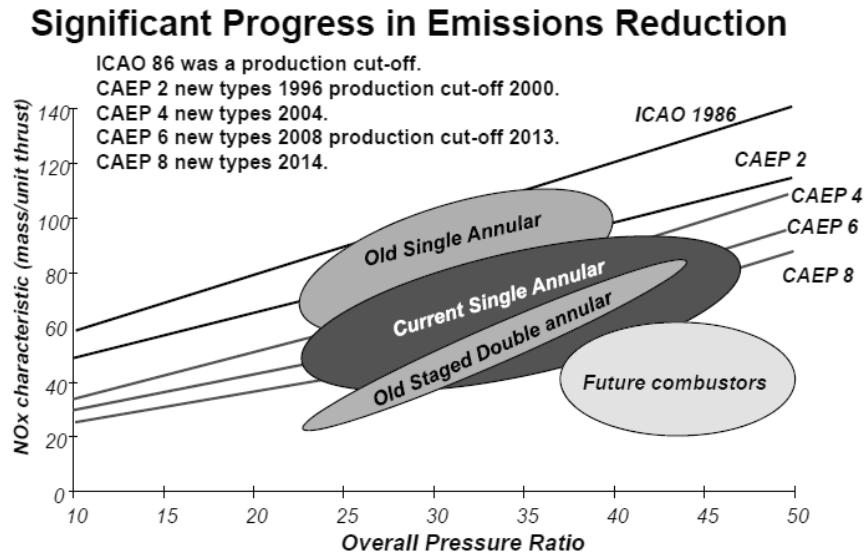


Fig. 1.1 CAEP combustion technology review.

Lean premixed gas turbine combustors are an effective means of controlling exhaust gases such as NO_x, and are widely used in aviation and industrial energy production systems because they offer relatively high efficiency compared with diffusion burners [8]. The gas turbines are popular because of the availability of various renewable and alternative fuels such as synthetic gas (composed of H₂ and CO) and synthetic natural gas (composed of H₂ and CH₄). However, premixed combustors may cause burner damage from the flash-back of flame and combustion instability, problems that have been studied by various research groups. To date, computational and analytic solutions have been preferred to experimental studies to reduce costs and time consumption, but highly accurate experimental values are required so that computational estimations can provide accurate predicted values.

The mechanism of combustion instability, which is acoustically amplified by the coupling of pressure and heat-release fluctuations in the combustion field, is not fully understood [9]. Various parametric studies have been conducted using high-speed laser diagnostics and other techniques to identify the cause of combustion instability, and experimental research has attempted to predict the combustion instability frequency and investigate the combustion instability phenomenon.

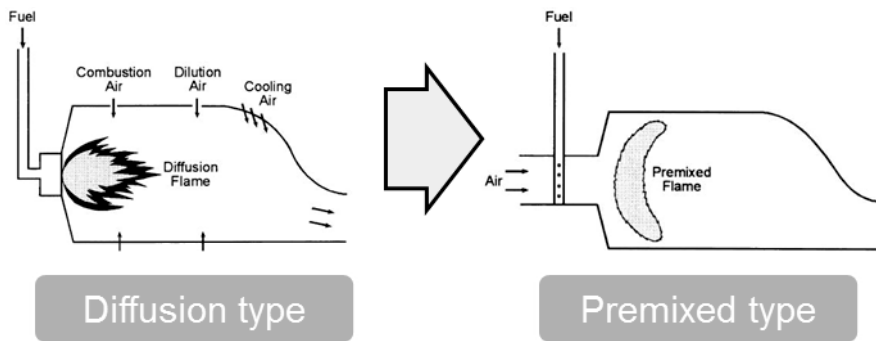


Fig. 1.2 Different combustion type for gas turbine combustor.

The purpose of this study is to investigate how the frequency of combustion instability is influenced by the hydrogen flow rate in a methane flame and to investigate the characteristics of the flame shape by varying the equivalence ratio and air supply flow rate. In addition, to simulate the actual combustion environment, the air supply was heated to 200°C and a plug nozzle was installed to form an acoustic boundary by the turbine blade at the exhaust duct of the combustor.

Lean direct injection (LDI) combustors supply the fuel to operate the gas turbine without a rich flame in the combustion zone, thus reducing NO_x emissions by minimizing the flame temperature and reducing the thermal stress of the combustor by eliminating local hot spots [10]. The direct injector used in this study injects fuel directly into the combustion chamber, achieving very high combustion efficiency through the high fuel-air mixing produced by the strong swirling effect. However, as little research on flame

transfer function (FTF) measurements in LDI gas turbines has been conducted, the measurement of the FTF in the present combustor is unique in terms of experimental research.

The combustion instability frequency/mode shifting (FMS) phenomenon was also found during the airflow rate variation in a premixed natural gas combustor [11]. However, most researchers [5–7] have either reported FMS only phenomenologically or the FMS phenomenon was not the main topic. Therefore, the present study was conducted to investigate the characteristics of FMS, as well as to identify the reason for FMS from the longitudinal fundamental mode to other modes.

In addition, High multi-mode instability is not a well-known part of instability research. The cause of instability mode shifting based on various test parameters and FTF characteristics was identified in previous research [15]. Some studies have been conducted on higher mode characteristics during the combustion instability. Mullter et al. conducted an experimental study on self-excited combustion instability and compared the ratio between the 1st, 2nd, and 3rd modes [16]. Moreover, Hester et al. compared the time domain characteristics of 1st, 2nd and 3rd longitudinal modes in a rocket combustor [17]. In addition, higher mode occurrence characteristics based on the flame-describing function was studied by Noiray et al [18]. Despite the above efforts, studies to identify the cause of multi-mode instability have rarely been undertaken in previous research. Therefore, the present study was conducted to investigate the characteristics and identify the cause of multi-mode instability in the partially premixed combustor.

The other main topic of interest during gas turbine development is instability prediction. Research about instability prediction can be separated into four categories: analytic solutions, lumped network models, large eddy simulation (LES), and experimental approaches. Table 1.1 shows the recent progress in each of these four categories. Experimental measurements, computational approaches, and the combination of experiments and computational fluid dynamics (CFD) are among the various ways that instability predictions are actively investigated. One of the key parameters for instability prediction is finding the relationship between the heat release and external fluctuation.

Flame transfer function (FTF) is the main parameter that must be found before instability prediction, as summarized in Table 1.1, and a lot of research has been put into this function and its diverse applications. FTF is a transfer function that represents the relationships between input and output variables. The equivalence ratio or inlet velocity is commonly selected as the input variable, with the heat release fluctuation of the flame normally selected as the output variable. FTF can be used to study combustor characteristics and to predict combustion instability.

Analytic and computational solutions using the nonlinear G equation during the disturbance were derived and compared to the experimental data by Preetham at GE [19]. Santavicca et al conducted the FTF measurements of turbulent premixed flames. The forced flame response of gas turbine can be quantitatively generalized using the flame shape and Strouhal number [20]. Various results were reported by the Candel group, and one of their experiments was conducted with the swirl premixed combustor [13, 14]. The flame describing function shows local minimum and maximum gain values. These experiments were also well received by LES [21]. However, the previous FTF research used a narrow modulation frequency range and was mainly conducted in a premixed combustor. The present study employed a wide range of modulations (0–1,000 Hz), and the effects of τ_{conv} at the FTF were determined by varying the fuel composition, airflow rate, and the ϕ .

Table 1.1 Categorized combustion instability prediction research.

Category	Year	Affiliation	Research Group	Contents
Analytic solution	2010	University of Leicester	P.D. Williams	Lean premixed FTF was compared with analytic formulation [23]
	2010	GIT	T. Lieuwen	G-equation based analytic Solution [19]
	2011	CNRS	T. Schuller	Analytic model was compared with the experimental data [24]
	2012	MIT	A.F. Ghoniem	Analytic model was compared with the experimental data [25]
Lumped Network Model	2010	Alstom	W. Mohr	Transfer matrix was applied in the real scale swirl gas turbine [26]
	2011	CNRS	S. Candel	Non-linear characteristics of swirl flame was found by acoustic transfer matrix [14]
CFD	2013	Universitat Munchen	W. Polifke	Effects of thermal boundary condition on the flame dynamic characteristics [27]
Experimental Approach	2010	Pennsylvania State University	D.A. Santavicca	Non-linear characteristics of FTF and local FTF [13, 21–24]
	2012	Queen Mary University of London	C. Lawn	Non-linear characteristics of CH ₄ flame [32]

The FTF is defined as the dynamic response characteristics of the heat release perturbation of the flame induced on the velocity perturbation of the fuel and air, and is expressed as the magnitude of the amplification and the time delay. The FTF provides a measurement method for identifying the combustion instability mechanism, and can be used as a flame model in simulating the combustion instability. The open source combustion instability low-order simulator (OSCILOS) is used to model the combustion instability, providing a suitable tool for modeling gas turbine combustors with a very long combustor length compared to the flame length. Accurate experimental data such as flame length, $gain_{FTF}$, and $phase_{FTF}$ are needed to predict the combustion instability frequency accurately. Therefore, various measuring instruments such as high-speed OH planar laser-induced fluorescence (PLIF), a photomultiplier tube (PMT), and hot-wire anemometry

(HWA) are used to improve the accuracy of the experimental data. As the flame transfer function is an experimental value for understanding the dynamic response to flame, it should eliminate the effects of disturbances and internal resonance, but it is not easy to control the acoustic disturbance that occurs in the pre-chamber. Therefore, in this study, we introduce a Fuel line transfer function (FLTF) to obtain the accurate FTF by effectively removing these effects, and propose an FTF. The combustion instability is modeled using this FTF, and it is shown that this produces more accurate predictions of combustion instability.

In summary, the purpose of this paper is to analyze the static characteristics (exhaust emissions), dynamic characteristics (combustion instability and flame transfer function) of SNG fuel composition in LDI gas turbine combustor. For these purposes, the following studies were performed.

1. In Chapter 3, NO_x emission characteristics is similar at the same heat load because of the same Wobbe index based on higher heating values of the fuel compositions. Moreover, NO_x increases with increasing equivalence ratio and heat load. This characteristics investigate that major NO_x mechanism is thermal NO_x. CO emission rapidly peaks near stoichiometric condition and it is affected OH radical in chemical reaction. Carbon dioxide is more effective to NO_x reduction than nitrogen diluent because of its high diluent heat capacity.
2. In Chapter 4, the instability frequency shifted from the first to the seventh mode as the H₂ ratio increased in the H₂/CH₄ mixture. However, 100% H₂ as fuel did not cause combustion instability because it has a higher burning velocity and extinction stretch rate than CH₄. Furthermore, the laminar flame speed influenced the frequency mode shift. These phenomena were confirmed by the flame shapes. The Abel inversion process was applied to obtain the cross section of the flames from averaged OH chemiluminescence images. Stable and unstable flames were identified from the radial profile of OH concentration. The combustor length was

found to not influence frequency mode shift, whereas the H₂ ratio significantly influenced it as well as the flame shape.

3. In Chapter 5, the mode shift is accompanied by shortening flame length and hence decreasing convection time delay between fuel injection and flame location. Flame transfer function (FTF) subject to fuel flow rate modulation is determined over a range of frequency for hydrogen/methane volume ratios of 25:75, 50:50, and 75:25 at a fixed equivalence ratio of 0.55. The input/output function of FTF is the velocity fluctuation of fuel flow at the inlet of combustor/the heat release fluctuation of whole flame, respectively. Due to the difficulty of measuring fuel flow velocity at the inlet of combustor while flame exists, the fuel transfer function (FLTF) is measured and used along with the intermediate flame transfer function (ITF) to determine the FTF. The transfer functions are measured at frequency up to 600 Hz and the FTF above 600 Hz is determined from flame response at the higher harmonic frequency. Results of the FLTF measurement show that an acoustic resonance is formed within fuel injector and the resonance frequency changes as the hydrogen/methane ratio as well as the length of fuel feedline changes. The gain of FTF at a given frequency decrease as the hydrogen content increases and the absolute value of the slope of phase plot which is related to the convection time delay between fuel injector tip and flame location decreases as the hydrogen enrichment ratio increases. Using the measured flame transfer function as input to an open-source code (OSCILOS), the occurrence of instability is predicted and compared with experimental results. Modelling results agree very well with experimental data in predicting the occurrence of unstable combustion, the frequency at which unstable combustion occurs and the acoustic mode inside combustor.

CHAPTER 2

EXPERIMENT AND MEASUREMENT SYSTEMS

2.1 Combustor and Nozzles

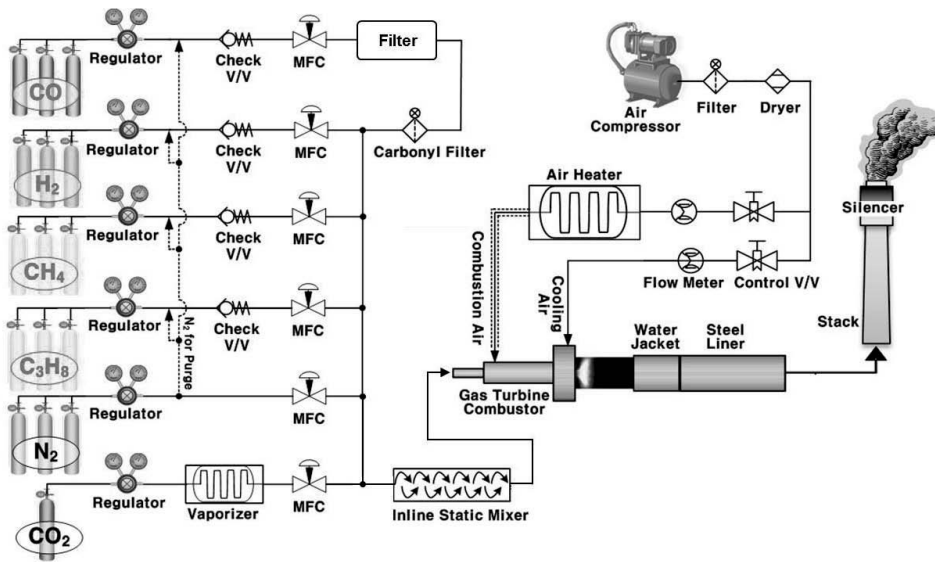


Fig. 2.1 Schematic diagram of the partially premixed gas turbine test facility.

For the purposes of this study, an atmospheric pressure high temperature combustion test facility for a 40 kW-scale gas turbine was installed. As shown in Fig 2.1 this facility consisted of an air compressor, an air heater, a cooling and combustion air feed line, an atmospheric pressure combustor, an external stack with silencer, and a fuel supplying system that can control the flow rate of H_2 , CO , CH_4 , N_2 and CO_2 respectively. Mass flow controller (MFC, Parker Porter 200, uncertainty: $\pm 1\%$ of full range) is used for the control of H_2 , CO , CH_4 , N_2 and CO_2 . The fuel gases were provided from each bottle of high-purity feedstock gases ($H_2 > 99.95 \text{ mol}\%$, $CO > 99.95 \text{ mol}\%$, $CH_4 > 99.9 \text{ mol}\%$). These gases were well mixed through the inline static mixer and injected to the combustor through 14 fuel injection holes within the inner side of swirl vanes at 2.7mm upstream of dump plane

to satisfy the partially premixed flame condition. The reactivity of CO is very high and it can make carbonyl the reaction with the supply line and these carbonyl is directly influences the flame visualization quality, because it will be coated inside the quartz tube. Therefore, for CO supply, carbonyl trapping gas purifier (Entegris, 10MH) was installed upstream of inline mixer. To meet gas turbine relevant conditions, dry air at the temperature of 200°C ($\pm 5^{\circ}\text{C}$) was supplied to the flame through a central annular swirling nozzle. The flow rate of combustion air was also controlled by a MFC (Bronkhorst F-206BI, uncertainty: $\pm 0.8\%$ of full range) and choke orifice is installed at the immediately upstream of the combustor to prevent the perturbation of supplying air by blocking the influence of pressure variation at the upstream flow. Combustion tests were conducted at slightly aviated pressure (1.1~1.2 bar) since 90% area of combustor outlet was blocked by water- cooled plug nozzle to form an acoustic boundary of combustion chamber outlet. The combustion air was supplied to the combustor at the rate of 1100 slpm in a dried condition and the quartz liner cooling air was also supplied at the 900 slpm. A fuel composition is varies according to the test subject.

To examine the combustion characteristics of the high H_2 composed fuel, a 1/3 scaled- down one can dump combustor of a GE7EA gas turbine was designed as model combustor. The partially premixed type combustor was used to minimize the hazard such as the flash back. Fig. 2.2 shows the schematic of the combustion test rig and details of the fuel nozzle. The combustion chamber consisted of two parts. The first part was made from optically accessible quartz, which was cooled by a high-pressure injection of the air. The second part was made from steel and it had water channel to protect the test facility. The cooling water flow rate was fixed as 4.4 slpm (= 73 g/s). The inner diameter and length of the combustion chamber was 130 mm and 1410 mm, respectively. As shown in Fig. 2.2 the fuel–air mixture was supplied through the annularly arranged fourteen swirl vanes of a 45 angle, and fuel was injected within the swirl vanes at 2.7 mm upstream of the dump plane to make a partially premixed flame. The detailed view of fuel-air mixing within the swirl vane is shown in Fig. 2.2 (b) and the direct photo of fuel nozzle is Fig. 2.2 (c). The inner and outer diameter of each swirl vane was 25.5 mm and 40 mm,

respectively, and the swirl number was 0.832, which was calculated via the following Eq. 2.1 [33]:

$$S_n = \frac{2}{3} \left[\frac{1 - (D_{swirl-in}/D_{swirl-out})^3}{1 - (D_{swirl-in}/D_{swirl-out})^2} \right] \tan\theta \quad (2.1)$$

Where $D_{swirl-in}$, $D_{swirl-out}$ and θ are inner diameter of swirler, outer diameter of swirler and swirl vane angle respectively.

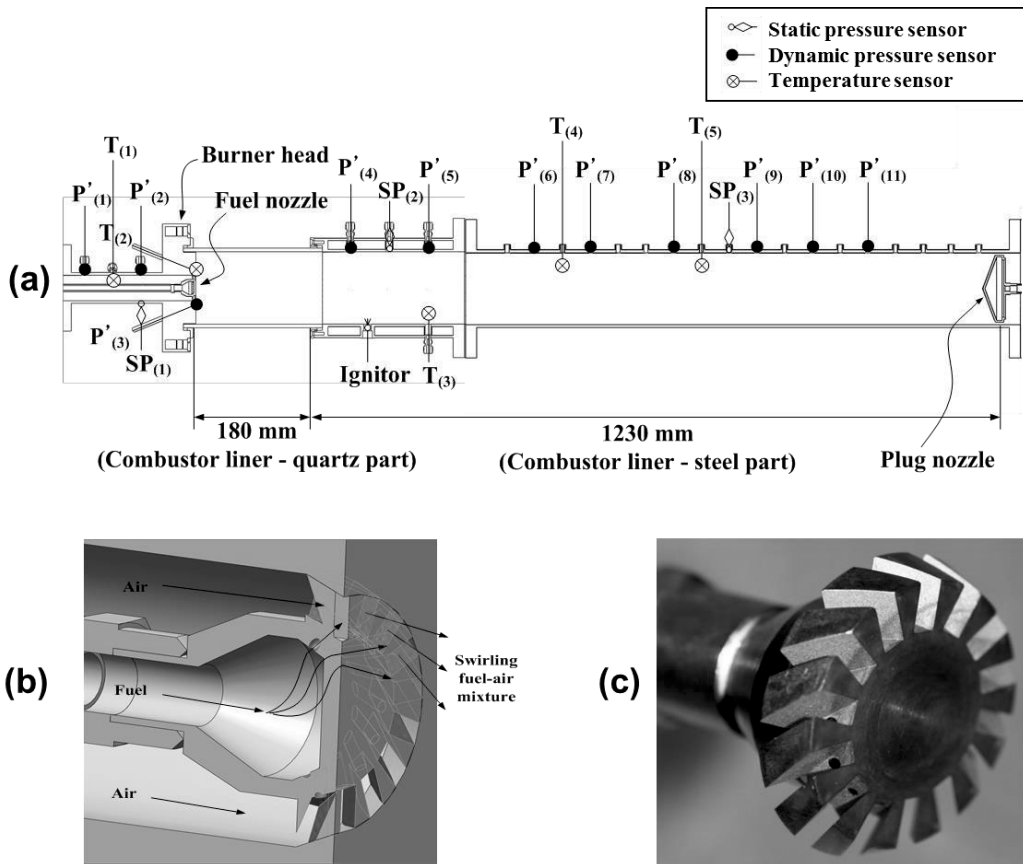


Fig. 2.2 Schematic diagram of measurements sensor location (a) model combustor (b) cross-sectional view of fuel nozzle (c) direct photo of tested fuel nozzle.

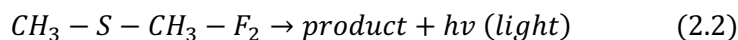
2.2 Flame Imaging

In this study, OH* chemiluminescence images were recorded to measure flame structure. Many other studies used direct photography to identify flame structure; however, images produced by this method are not good indicators of the reaction zone. The OH* chemiluminescence image should be used since OH radicals are good indicators of the reaction zone, which is a high temperature region. Thus, OH* chemiluminescence images were acquired using a ICCD camera (PI-MAX, Princeton Instruments, 512×512 pixel CCD) with a UV-Nikkor lens ($f = 105$ mm; $f/4.5$) and 307.1 ± 5 nm narrow bandpass filter. OH* chemiluminescence images were taken with 1 ms exposure time and 50 images were averaged for obtaining flame structure and observing flame behaviors in various fuel composition. The threshold value used to define the flame was 5% of the maximum intensity of the averaged image.

2.2.1. Chemiluminescence Spectroscopy

In chapter 3, OH* chemiluminescence measurements were conducted to obtain the reaction region. Chemiluminescence, like atomic emission spectroscopy (AES), uses quantitative measurements of the optical emission from excited chemical species to determine analyte concentration; however, unlike AES, chemiluminescence is usually defined as the emission from energized molecules instead of simply excited atoms. The bands of light determined by this technique emanate from molecular emissions and are therefore broader and more complex than bands originating from atomic spectra. Furthermore, chemiluminescence can take place in either the solution or gas phase, whereas AES is almost strictly as gas phase phenomenon. Like fluorescence spectroscopy, chemiluminescence strength lies in the detection of electromagnetic radiation produced in a system with very low background. On top of this, because the energy necessary to excite the analyte to higher electronic, vibrational, and rotational states (from which they can decay by emission) does not come from an external light source like a laser or lamp, the problem of excitation source scattering is completely avoided. If the excitation energy for

analyte in chemiluminescence is produced by a chemical reaction of the analyte and a reagent. An example of a reaction of this sort is shown below:



In gas phase chemiluminescence, the light emission (represented as $h\nu$) is produced by the reaction of an analyte (dimethyl sulfide in the above example) and a strongly oxidizing reagent gas such as fluorine (in the example above) or ozone, for instance. The reaction occurs on a time scale such that the production of light is essentially instantaneous; therefore, most analyte systems simply mix analytes and the reagent in a small volume chamber directly. If the analytes are eluting from a gas chromatographic column than the end of the column is often fed directly into the reaction chamber itself. Since as much of the energy released by the reaction should (in the analyst's eye) be used to excite as many of the analyte molecules as possible, loss of energy via gas phase collisions is undesirable, and therefore a final consideration is that the gas pressure in the reaction chamber be maintained at a low pressure (~ 1 torr) by a vacuum pump in order to minimize the effects of collisional deactivation. It must be stated that the ambiguous specification of "products" in the above reaction is often necessary because of the nature and complexity of the reaction. In some reactions, the chemiluminescent emitters are relatively well known. In the above reaction the major emitter is electronically and vibrationally excited HF; however, in the same reaction, other emitters have been determined whose identities are not known. To the analytical chemist the ambiguity about the actual products in the reaction is, in most case, not important. All the analyst cares about is the sensitivity of the instrument (read detection limits for target analytes), its selectivity-that is, response for an analyte as compared to an interfering compound, and the linear range of response.

2.2.2. Abel Transform

Abel convolution is one of optical diffraction tomography and integral transform, such as onion pilling method and back-projection algorithm. It is useful to transfer a 3-dimensional line-of-sight image to a 2-dimensional profile. The light emission measurement of chemiluminescence cannot capture the fine flame structure, because the signal is integrated through the depth of the flame. Therefore, each image was processed with Abel convolution. With Abel inverted images, the time-averaged flame structure profile can be reconstructed, if the flame shape is axisymmetric.

In mathematics, the Abel transformation, named for Niels Henrik Abel, is an integral transform often used in the analysis of spherically symmetric or axially symmetric functions. The Abel transform of a function $f(r)$ is given by:

$$F(y) = 2 \int_y^{\infty} \frac{f(r)r}{\sqrt{r^2 - y^2}} dr \quad (2.3)$$

Assuming $f(r)$ drops to zero more quickly than $1/r$, the inverse Abel transform is given by:

$$F(r) = -\frac{1}{\pi} 2 \int_y^{\infty} \frac{dF}{dy} \frac{1}{\sqrt{r^2 - y^2}} dy \quad (2.4)$$

In Chapter 3, the OH^* chemiluminescence signal was processed through inverse Abel transform to transfer a 3-D line-of-sight image into a 2-D flame profile and the OH radical is treated as a marker of heat release in a reaction zone.

2.3 Laser Diagnostics

2.3.1. OH-PLIF Measurement

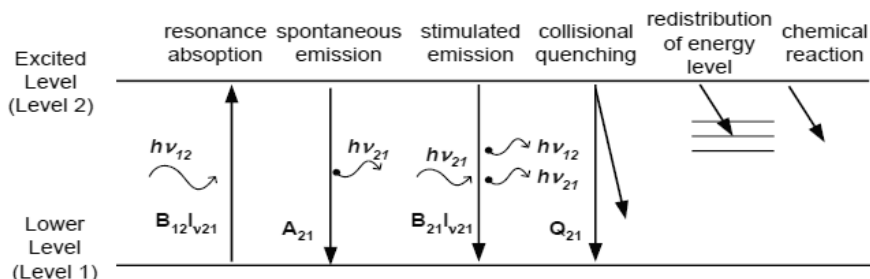


Fig. 2.3 Schematic of relaxation processes emission of photons.

Laser induced fluorescence (LIF) is described as the absorption of a photon by a molecule of radical, followed by an emission of a photon as the molecules undergoes the transition from a higher level energy state to a lower one. Figure 2.3 shows the schematic of energy transfer process. Some of the molecules will relax to the initial state by emission of photon. Several relaxation processes are possible including (a) spontaneous emission, (b) stimulated emission by exterior stimulus, (c) quenching by collision of molecules, (d) redistribution of energy level, and (e) change of molecular component by chemical reaction. However, the rapid or spontaneous emissions of photons are termed as LIF. The frequency of LIF signal can have different value from that of inducing laser beam.

Table 2.1 Formation and destruction of OH radical.

Fast OH formation by two-body reactions (1~5nsec)¹⁾	
$H + O_2$	$\leftrightarrow OH + O$
$O + H_2$	$\leftrightarrow OH + H_{1)}$
$H + HO_2$	$\leftrightarrow OH + OH_{1)}$
Slow destruction by three-body recombination reactions (~20μsec)¹⁾	
$H + OH + M$	$\leftrightarrow H_2O + M_{1)}$

OH-PLIF was used to obtain spatially and temporally resolved images of the reaction zone in various combustors. As described in Table 2.1, the OH radical concentration increases rapidly around the flame in about 20 μ sec and then decomposes slowly in 1 to 5 ms by a 3-body recombination reaction [34]. Thus, near the flame front exists super-equilibrium OH. The OH radical, which is intermediate product of chemical reaction, has a concentration of more ten times than that of O or H radicals. Therefore, the OH radical is found to emit more intensive fluorescence signal than other species when absorbing laser light. Hence, the fluorescence signal of OH radical is widely used as an indicator of flame front in reacting flows.

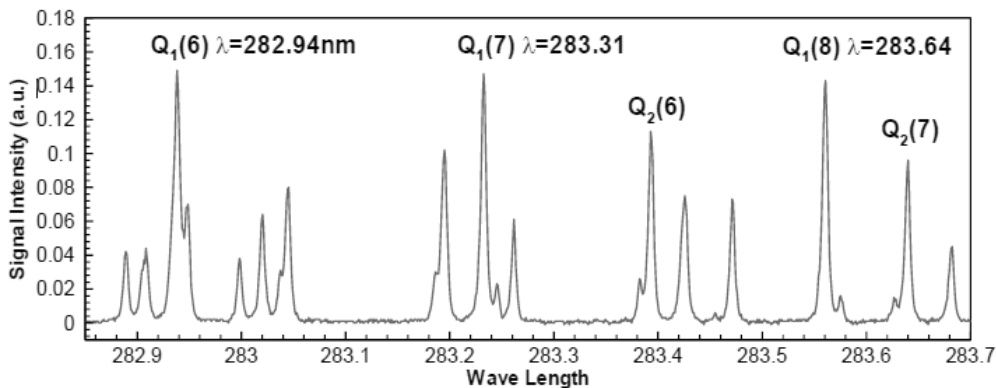


Fig. 2.4 OH excitation spectrum; In this study, Q₁(6) was used for OH PLIF.

To observe the line positions for transition, we scanned the dye laser and recorded the signal at each step. We intended to use Q₁(6) transition of the $A^2\Sigma^+ \leftarrow X^2\Pi$ ($v' = 1, v'' = 1$) band ($\lambda = 282.94$ nm) for the excitation wavelength and to collect the fluorescence signal from the $A-X$ (1, 0) and (0, 0) bands ($\lambda = 306 \sim 320$ nm). Using monochromator and photomultiplier tube (PMT), in conjunction with a test flame in laminar premixed condition, a laser excitation scan was performed over the range of interest from $\lambda = 282.5$ nm to $\lambda = 283.5$ nm with 0.001 nm step. The monochromator was fixed at 315 nm to collect the fluorescence. The signal was multiplied by PMT and recorded through the boxcar averager. At every scanning step, 10 pulses of signal were recorded and averaged. After

scanning the dye laser, the OH excitation spectrum can be obtained as shown in Fig 2.4. Among the peak values of excitation spectrum, we used Q₁(6) as the excitation wavelength of OH radical.

When the location of Q₁(6) line was detected, the fluorescence spectrum could be obtained by recording the LIF signal at each scanning step of the monochromator. Figure 2.5 is OH fluorescence spectrum graph for Q₁(6). Peak value is found at 320nm.

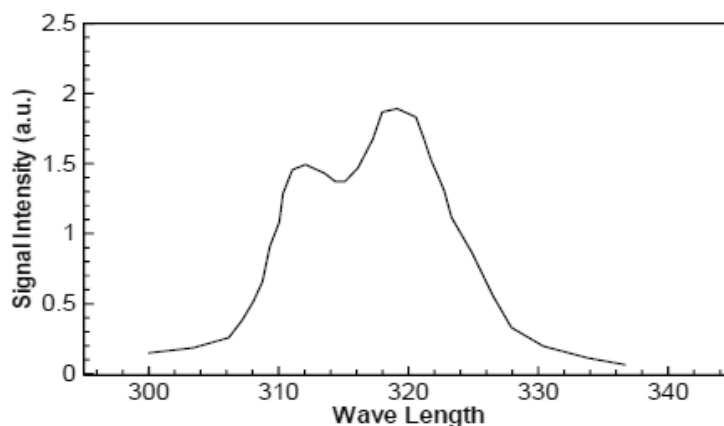


Fig. 2.5 OH fluorescence spectrum for Q₁(6).

PLIF System

For OH PLIF, an Nd:YAG pumped dye laser was turned to Q₁(6) transition of the $A^2\Sigma^+ \rightarrow X^2\Pi$ ($v' = 1, v'' = 1$) band ($\lambda = 282.94$ nm). Q₁(6) transition line is generally used in the measurement of molecular concentration because it has large LIF signal and the dependency for temperature is low. Fluorescence from the $A-X$ (1, 0) and (0, 0) bands ($\lambda = 306 \sim 320$ nm) were collected with a UV-Nikkor 105 mm/f 4.5 lens. Because UV light cannot penetrate the common glass, all the lenses should be made with quartz. The region of interest was focused onto the ICCD camera of Princeton Instrument (PI-MAX 1K). Two filters (WG-305 and UG-11) were used to block scattered signal lights. Transmittance of each filter is shown in Fig. 2.6. The schematic diagram of OH-PLIF system which was used in this study is also shown in Fig. 2.7.

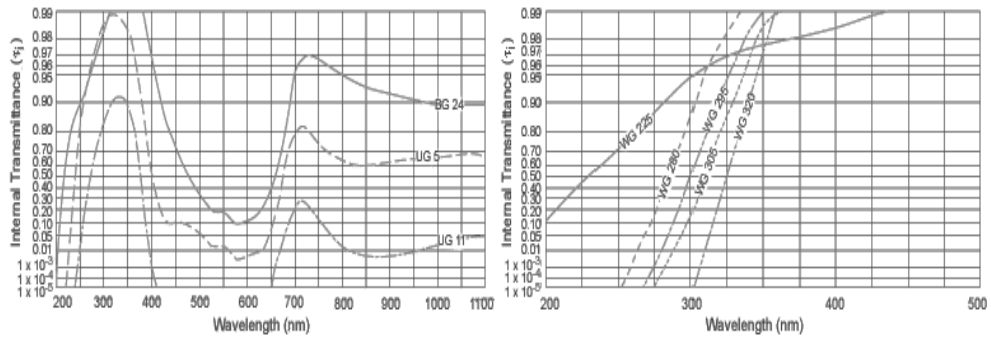


Fig. 2.6 Transmittance of filter (a) WG-305 (b) UG-11.

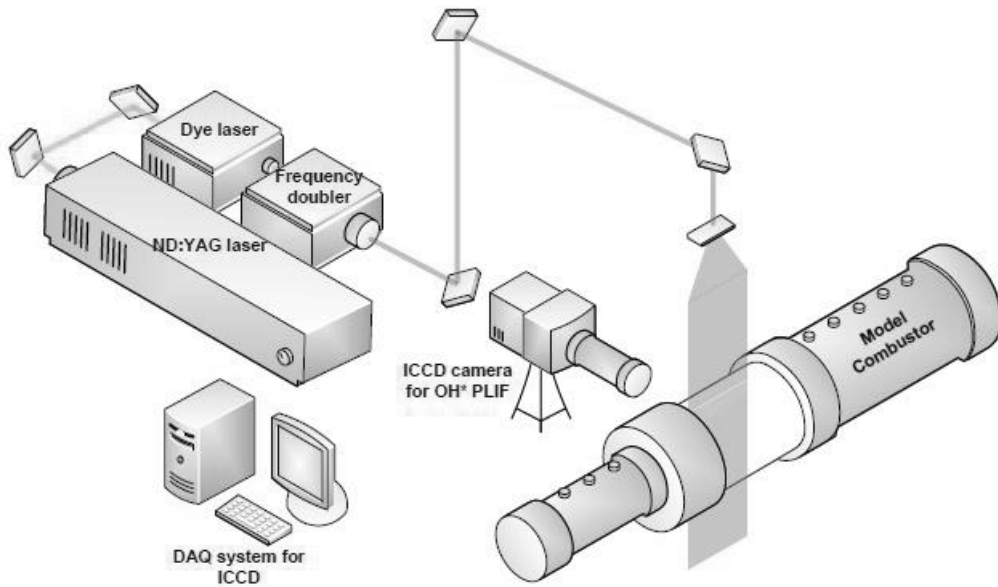


Fig. 2.7 Schematic diagram of OH-PLIF measurement system.

High speed PLIF System

High speed laser measurement widely applied in various research field to find the unknown characteristics of high frequency phenomenon. Many research groups are conducting experimental approach about CH_4/Air flame, Liquid fuel flame and micro

structure of the flame. The detailed information about the research are summarized in Table. 2.2.

Table. 2.2 High-speed PLIF application research summary.

Research Group	Year	Author	Contents
DLR	2013	M. Stohr	Simultaneous measurement of PIV & OH PLIF in CH ₄ swirling flame [35]
DLR	2011	M. Stohr	Blow off characteristics of CH ₄ swirling flame [36]
DLR	2010	I. Boxx	Simultaneous measurement of transient phenomena in a partially premixed swirl flame [37]
CNRS	2012	P. Petersson	Simultaneous high-speed PIV & OH-PLIF about coaxial diffusion flame burner [38]
CNRS	2014	P. Xavier	Cavity flame anchoring characteristics based on high- speed OH-PLIF
University of Cambridge	2011	J.R. Dawson	Near blow-off characteristics of bluff body stabilized CH ₄ flame [39]
University of Cambridge	2012	N.A. Worth	Flame interaction of CH ₄ /air conical bluff-body stabilized flame [40]
AFRL	2013	S. Hammack	Plasma-enhanced flame characteristics of turbulent non-premixed flame [41]
Michigan University	2015	P.M. Allison	CH ₂ O-PLIF measurements in dual-swirl burner [42]
Sydney University	2011	S. Meares	High-speed OH-PLIF imaging of extinction and re-ignition [43]

In this study, the high harmonic instability frequencies were measured and the application of high-speed OH-PLIF is necessary to find the high frequency structural characteristics. High-speed OH-PLIF were set up at the rate of 7 kHz. The 7 kHz OH-PLIF used the laser beam from an Nd-YAG laser (Edgewave, IS-200-L) as the pumping source for the dye laser (Sirah, Credo-Dye-LG-24) and the OH fluorescence signal was measured by an intensifier (HS-IRO), a high speed camera (HSS8), a UV lens (f/2.8), and a bandpass filter (307±10 nm).

2.3.2. PIV Measurements

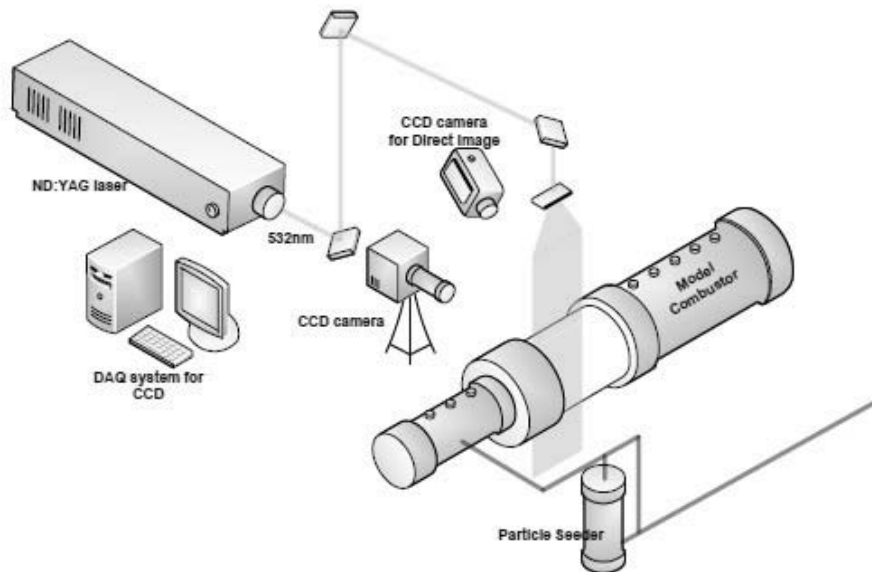


Fig. 2.8 Schematic diagram of PIV measurement system.

A particle image velocimetry (PIV) is the measurement technique, which obtains the velocity vector fields of a flow by comparing consecutive two images. The experimental set-up of PIV system consists of several sub-systems: light source system, detecting system, and particle seeding system as shown in Fig. 2.8. Small particles have to be seeded into flow to perform PIV technique because PIV measures only the velocity of particles by comparing the displacement of the particle images illuminated by the sequential light pulses, not the flow itself.

Generally, a double pulsed Nd-YAG laser is used as a light source and a high speed CCD camera is employed to obtain instantaneous particle images at a measurement plane. There are no specific rules for particle seeding system; however, the size of particle should be determined by considering whether particles can follow the flow well or not. In most cases, it is necessary to add tracer particles into the flow. These particles are

illuminated at the measurement plane of the flow at least twice times within a short interval. The light scattered or fluoresced by particle is recorded either on a single frame or on sequential frames. The displacement of the particle images recorded by the light pulses is calculated through evaluation of the PIV.

To calculate the displacement of the particles grabbed by a CCD camera, it is necessary to divide the image into a grid. The grid is called as an interrogation spot. After setting the interrogation spot size, one interrogation spot of the first images is picked and compared with all the interrogation spot of the second images. The displacement between the interrogation spot of the first image and the interrogation spot of the second image represents one vector of flow field. By conducting this work in all the interrogation spots, whole vectors of flow-field are obtained. This process is called as a correlation.

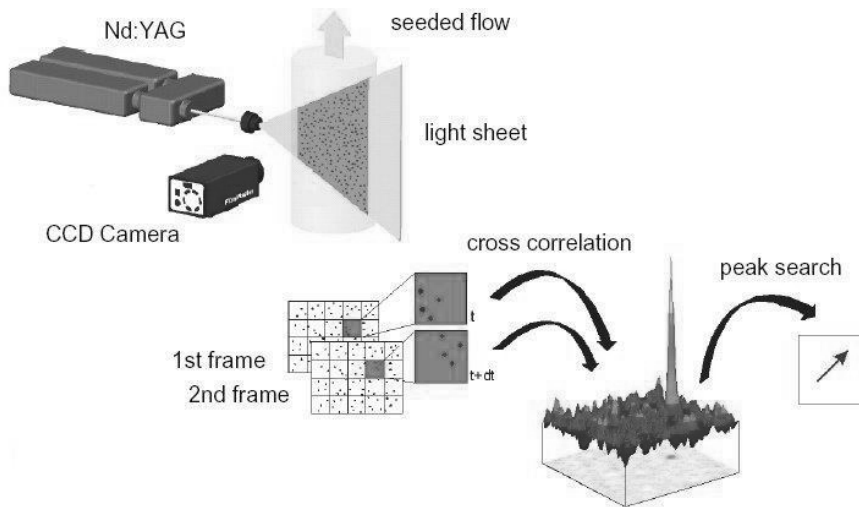


Fig. 2.9 Principle of typical PIV system.

The correlation function is expressed as follows:

$$h(s_x, s_y) = \int_0^{\infty} \int_0^{\infty} f(x, y)g(x + s_x, y + s_y) dx dy \quad (2.5)$$

The expression can become simple as conducting Fourier transformation for a convenience's sake in calculating. Here, F and G are Fourier transformed function of each f and g , and they mean Fourier transform operator.

$$F(h) = F^*(f) \times F(g) = F^* \times G \quad (2.6)$$

$$h = F^{-1}(F^* \times G) \quad (2.7)$$

Equation 2.5 is the same expression of spatial masking in an image processing technique. Thus, it means that a correlation is a kind of masking concepts. According to this concept, the correlation can be called as a process to figure out distribution of the similarity by signal distribution in an image plane. Equation 2.7 makes us use fast Fourier transform (FFT) algorithm which reduces the calculation time drastically. The interrogation spot size of $2n \times 2n$ should be chosen to use FFT algorithm because FFT algorithm is a method by dividing even and odd terms. However, the calculation time becomes short by $\log_2 N/N$ times comparing with direct Fourier transform (DFT) algorithm.

A correlation method is separated into auto-correlation and cross-correlation by the number of functions. Mathematically, auto-correlation is the case; $f(x; y) = g(x; y)$ in Eq. 2.7 and cross-correlation is the case; $f(x; y) \neq g(x; y)$. Experimentally, an auto-correlation is used for the case where the first image at $t = t_1$ and the second image at $t = t_2$ are recorded in one frame (called as a single frame/double exposure mode) and cross-correlation is used for the case where the first image at $t = t_1$ and the second image at $t = t_2$ are recorded in separated frames (called as a double frame/single exposure mode). Comparing with an auto-correlation method, a cross-correlation method has some merits as follows:

1. Directional ambiguity problem can be avoided easily.

2. The algorithm is simple because there is only one peak as a result of correlation.
3. Dynamic range is relatively large.

However, it was difficult to satisfy hardware requirements for cross-correlation. Specially, a time interval was a problem in most cases because the device, which satisfied both high resolution condition and short time interval (microsecond), was very expensive. Nowadays, it becomes relatively inexpensive and popular. Thus, most PIV systems use a cross-correlation method.

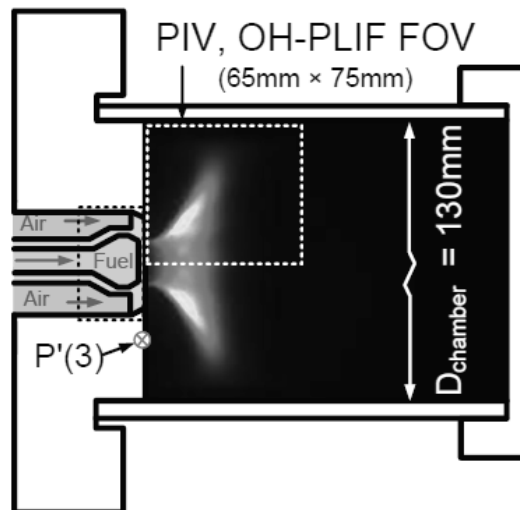


Fig. 2.10 Field of view of PIV and OH-PLIF measurement.

In this study, the scattering signal of seeding particles (ZrO_2 , $1\ \mu\text{m}$) from a sheet beam of the Nd-YAG laser (Continuum, Surelite-II) was measured using a CCD camera (Viewworks, VH-2MC-M42) mounted with a lens ($f/2.8$) and a band pass filter ($532\pm 10\ \text{nm}$). The field of view of the PIV and OH-PLIF was $65\text{mm}\times 75\text{mm}$. The time interval of the PIV was $3\ \mu\text{s}$, and 100 pairs of the instantaneous images were used to calculate the average velocity field. The interrogation spot size was 64×64 pixel, the overlap ratio

was 50%, and Fast Fourier Transform-based cross correlation was applied for post-processing. Fig. 2.10 shows the field of view of PIV and OH-PLIF measurement.

2.4 Flame Transfer Function Measurement

A fuel flow rate modulation device (Siren), a PMT (Hamamatsu, H7732-10), and a hot wire anemometer (Dantec, MiniCTA) were used to measure the FTF. During FTF measurements, the input fluctuation was limited to up to 10% of the mean velocity. A plug nozzle was used to achieve the closed acoustic boundary in the instability tests. However, during the FTF measurements, the plug nozzle was removed to reduce the combustor geometry effects and make the combustor exit as an open boundary condition. Commonly, three kinds of modulation devices have been used during flame-transfer function measurement experiments: acoustic devices, the solenoid valve, and the siren. Previously modulation research (and the devices used) are summarized in Table 2.3.

Table 2.3 Summary of flow modulation device and application.

Modulation device	Author	Contents
Speaker	C.O. Paschereit	Transfer matrices: 2002 [44]
Solenoid valve	A.X. Sengissen	LES: 2007 [45]
	S. Peter	Syngas FFT and CFD: 2007 [46]
Siren	K.T. Kim	FTF measurement, 2010
	W.S. Cheung	FTF measurement: 2003 [47]
	T. Sattelmayer	FTF measurement: 2004

The siren is a modulating device that rotates the disk; the area change of the flow path results in flow-rate modulation. The potential modulation frequency range of a solenoid valve is narrower than we expected and using a speaker at the increased inlet air temperature conditions under which our test was conducted is difficult. Therefore, the siren-type fuel modulation device was selected for this study. Additionally, in contrast with most previous research the fuel line was separately modulated to find the effect of the fuel

flow-rate modulation effects on the flame characteristics. Therefore, for the fuel modulation tests, a siren-type fuel modulation device was installed upstream of the fuel inlet line. The modulation frequency of the siren can be varied up to 1100 Hz. Figure 2.11 shows the FTF measurement system.

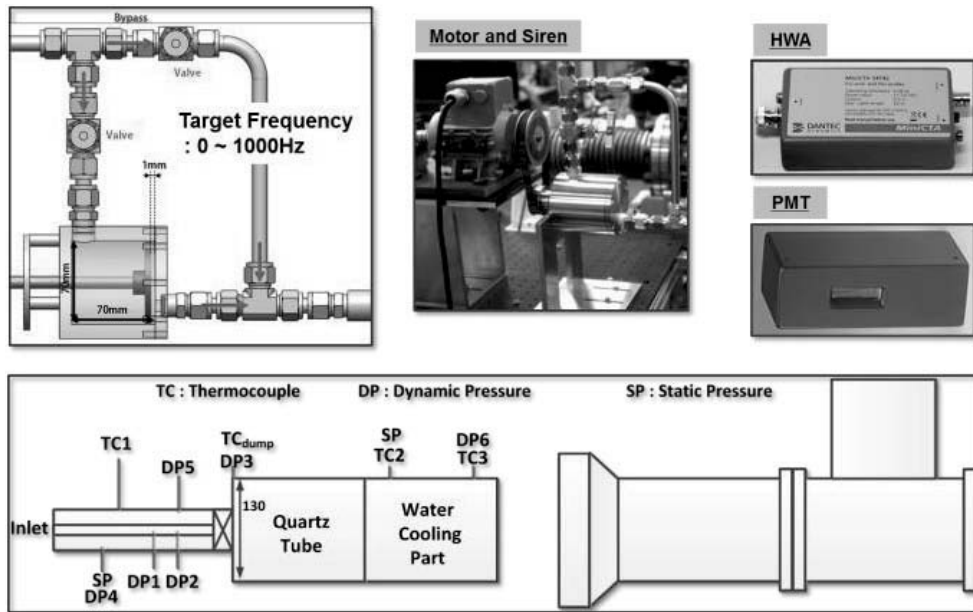


Fig. 2.11 Schematic diagram of the FTF measurement system.

The fuel-modulation amplitude effects on the FTF characteristics were confirmed by the bypass ratio variation in Fig. 2.11. The bypass (shown in Fig. 2.12) was made to control the fuel fluctuation's amplitude. The bypass ratio, which is defined as the bypass flow rate divided by the siren incoming flow rate, was varied from 0% to 75%. Similar FTF gain and phase results occurred with variations of the bypass ratio; in our test condition, therefore, the effects of fuel-modulation amplitude were negligible.

In addition, Hot-wire anemometry was applied to measure the input variable (fuel-velocity fluctuation and heat release); the output variable was measured by PMT. Measurement data were recorded by the Labview-based data acquisition system, with

a sampling rate was 25,000 samples/s.

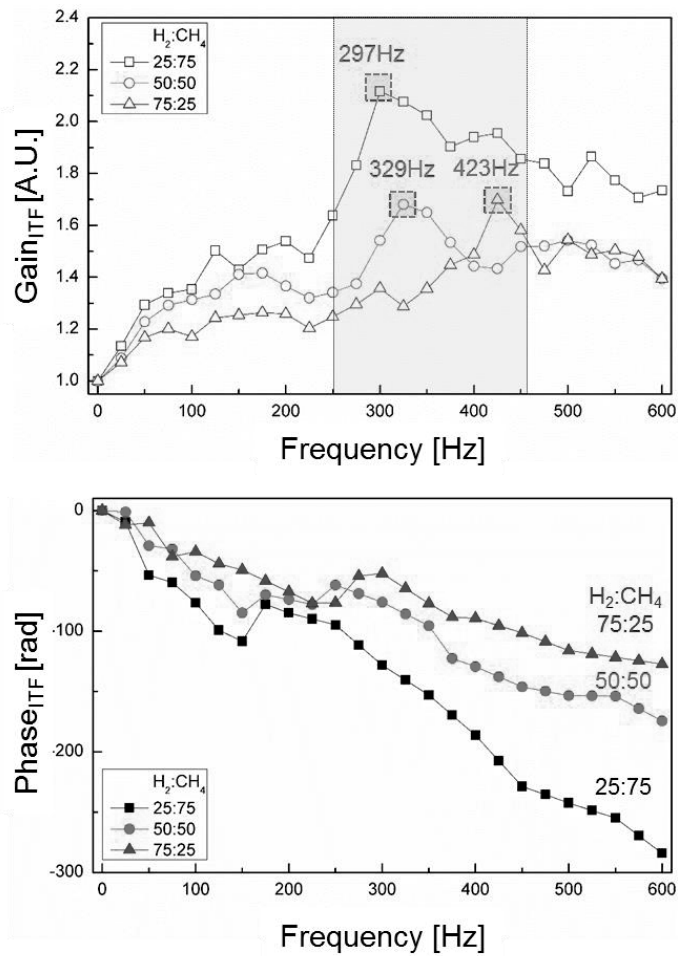


Fig. 2.12 Modulation amplitude effects on FTF characteristics.

2.5 Instability Prediction by 1-D Lumped Network Model

The open source combustion instability low order simulator(OSCILOS)

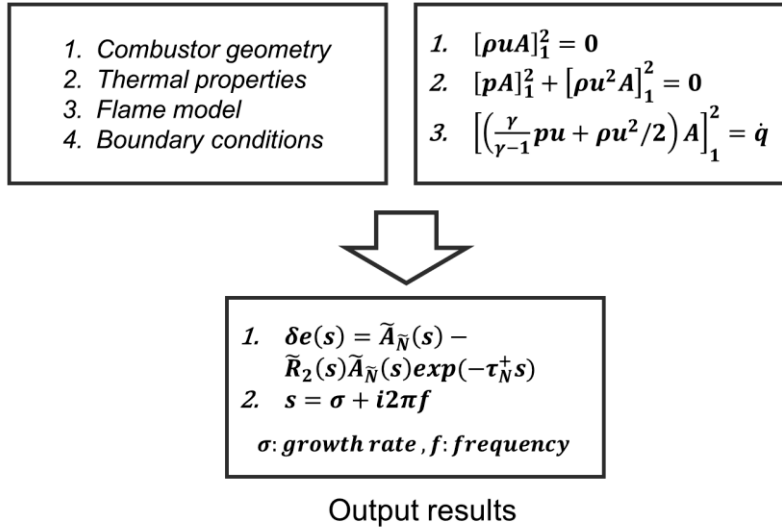


Fig. 2.13 Software structure of OSCILOS.

In the case of a gas turbine, unstable combustion will adversely affect not only the combustor failure but also the downstream part, resulting in a disruption of the power supply system. Therefore, it is important to understand combustion instability characteristics in gas turbine combustor development. In particular, if the combustion instability phenomenon can be analyzed and predicted, it is possible to design a combustor that avoids the conditions in which the combustion instability phenomenon occurs in advance, or to effectively avoid the combustion instability condition that occurs during operation. In order to predict the combustion instability, various attempts have been made. The lower order model [48], the direct method (RANS, LES) [49], the linearized equations in time domain [50] and the Helmholtz solver [51] have been studied to predict the combustion instability. One example of the lower order model is the open source code, OSCILOS, based on the 1D lumped network method. OSCILOS is a code developed by

the A.S. Morgans in Imperial University to predict combustion instability in the frequency domain and time domain. The OSCILOS analysis was carried out through the CFD based flame transfer function and the combustor geometry information, and it was confirmed that the frequency prediction was successful. The OSCILOS analyzes the combustion instability phenomenon based on the 1-D lumped method with the structure shown in Figure 2.13. The combustor length, thermal properties, flame model and boundary conditions are set as input variables and the combustion instability is analyzed in the frequency domain. The 1-D lumped method is based on two assumptions. First, only the longitudinal acoustic waves of the 1-D plane are considered, assuming that the radial perturbation is negligibly smaller than that of the longitudinal acoustic waves. It is also assumed that the length of the flame is relatively short compared to the wavelength of the acoustic wave, so it is assumed to be thin flame. Through these assumptions, the combustion instability prediction is performed as follows. The combustor is divided into a plurality of modules and the thermal properties of each module are continuous with respect to the boundary surface. Finding the thermal properties of each module that meets the governing equations with minimal error, a combination of instability frequencies and growth rates is obtained.

2.5.1. Combustor Geometry

FTF data for the central annular swirling nozzle was obtained using the system as shown in the Fig. 2.2 and combustion instability experiment of the test rig in the Figure 2.2 were performed. The combustor length can be varied from 1160 mm to 1400 mm by changing the position of the plug nozzle. A cooling system is applied during the combustion test to prevent overheating of the combustor due to heat. The quartz installed for flame visualization is cooled by air and the plug nozzle and the combustor are cooled by water. After the combustion tests were completed, the instability of the partially premixed combustor using the 1D lumped method was analyzed and predicted.

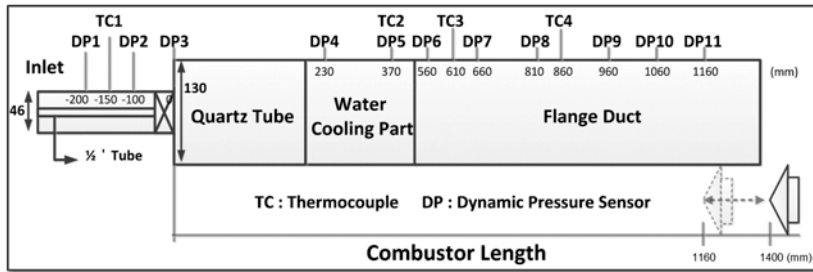


Fig. 2.14 Schematic of the gas turbine combustor.

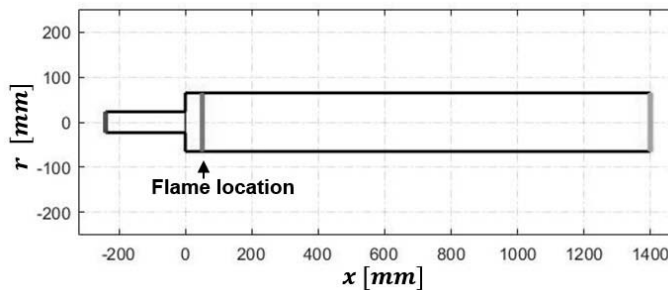


Fig. 2.15 Schematic of the gas turbine combustor modeling.

For the analysis and prediction through the 1D lumped method, the inlet, flame, combustor, outlet and boundary conditions are defined as shown in the Fig. 2.15. The inlet of the rig is set based on the strainer installed to stabilize the flow, and the outlet of the rig is defined as the plug nozzle.

2.5.2. Flame Position

Yoon et al. presented the convection time as a major parameter in the combustion instability mode shifting phenomenon of partially premixed model combustor. Unlike the case of the premixed combustor, the convection time depends on the distance from the dump surface to the flame surface, since the mixing length of the partially premixed combustor is relatively short. The 1-D lumped method was developed for a premixed

combustor, but the combustion instability was analyzed and predicted by controlling the flame position to make a significant change in convection time in the partially premixed combustor.

In this study, it was important to decide how to select the flame position that would have a large impact on the convection time. Two flame lengths, L_{coi} and L_{ub} , obtained through visualization were calculated to select the appropriate flame position for modeling. First, L_{coi} is calculated as the distance from the dump surface to the center of the intensity from the averaged flame image as shown in the Figure 2.16. These OH chemiluminescence images were obtained from an intensified charge-coupled device (ICCD) camera (Princeton Instruments, PI-MAX2), a UV lens (f/4.5), and a filter (WG-305, UG-11). Next, L_{ub} was calculated as the distance from the dump surface to the end of the unburned gas area from the averaged image as shown in the Fig. 2.17. These OH PILF images were acquired with an Nd-YAG laser (Continuum, Surelite-I), dye laser (Continuum, ND-6000), an ICCD camera (Princeton Instruments, PI-MAX2), a UV lens (f/4.5), and a filter (WG-305, UG-11).

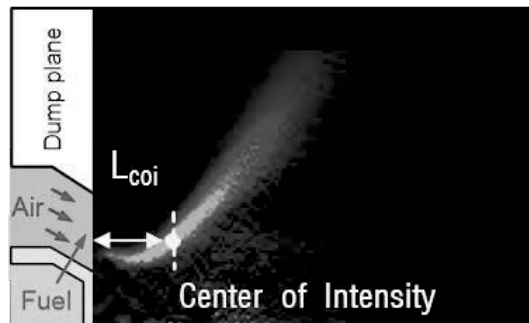


Fig. 2.16 Average flame image measured by the OH chemiluminescence.

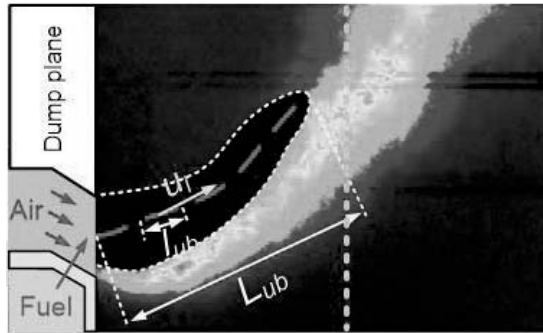


Fig. 2.17 Average flame image measured by the OH-PLIF.

The results of the instability frequency prediction for the 25% H₂, 75% CH₄ fuel composition and 1400 mm combustor length condition are shown in the table 2.4 were used to determine the flame length to be applied to the flame position. Although L_{ub} is about 1% difference from the L_{coi}, it was used for combustion instability analysis and prediction because it had relatively less error. This result is because L_{ub}, the distance from the dump surface to the end of the unburned gas area, is a better representation of the convection time, which is a key factor in the combustion instability characteristics of a partially premixed combustor with a short mixing length.

Table. 2.4 Prediction of instability frequency according to the flame position.

Parameter	L _{coi}	L _{ub}	Experiment
Length [mm]	35	51	-
Frequency [Hz]	568	565	505
Error [%]	-12.5	-11.9	-

2.5.3. Thermal Properties

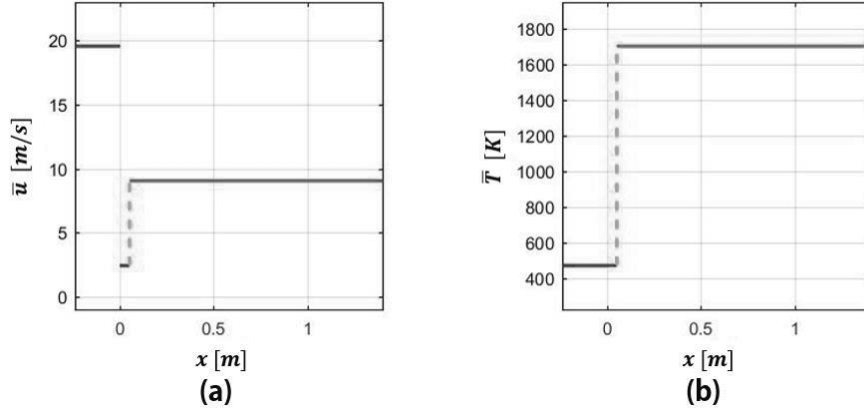


Fig. 2.18 (a) Velocity, and (b) temperature for 25% H₂, 75% CH₄ fuel composition.

The 1-D lumped method code is based on a premixed combustor, so there is no distinction between air and fuel line. Therefore, the thermal properties required for prediction were calculated in advance using the NASA's CEA code. It is set to match the thermal properties obtained from the partially premixed combustor experiment and is used in the prediction in the form of step function as shown in the Fig. 2.18. The origin of the x-axis from the Fig. 2.18 is the dump surface of the combustor.

2.5.4. Flame Model

FTF measurement must be preceded in order to predict combustion instability. The FTF expresses the relationship between the amount of acoustic perturbation and the amount of heat release perturbation. The FTF considered in this study is defined as Eq. 2.8.

$$FTF(s) = \frac{\hat{q}(s)/\bar{q}(s)}{\hat{u}(s)/\bar{u}(s)} \quad (2.8)$$

The ratio of velocity fluctuations is measured by HWA and the ratio of heat release fluctuations is measured by PMT with OH* filter. Based on the measured data, the gain and phase of the FTF are calculated using Eq. 2.9

$$Gain = |FTF(s)| \quad (2.9)$$

$$Phase = \tan^{-1} \left[\frac{FTF(s)_{im}}{FTF(s)_{real}} \right] \quad (2.10)$$

The gain and phase of the FTF were obtained for H₂ fuel composition (25-87.5%, span = 12.5%) which could be measured, and it was input into the following approximate Eq. 2.10 as the flame model.

In fact, more accurate combustion instability analysis requires a FDF that is a function of not only the frequency but also the velocity perturbation. However, due to the limitations of the experimental apparatus, the FTF is used as the flame model in this study.

$$FTF(s) = \frac{b_1 s^{n-1} + b_2 s^{n-2} + \dots + b_{n-1} s + b_n}{a_1 s^{m-1} + a_2 s^{m-2} + \dots + a_{m-1} s + a_m} \quad (2.11)$$

In order to use the FTF results accurately, curve fitting using MATLAB code was applied. To maintain the characteristics of the FTF function measured by the experiment, the y intercept of the gain is held at 1 and the y intercept of the phase is fixed at zero. After curve fitting, the gain and phase of FTF was obtained each fuel composition condition, such as in the 25% H₂ fuel condition in the Fig. 2.19 and are used for combustion instability analysis and prediction.

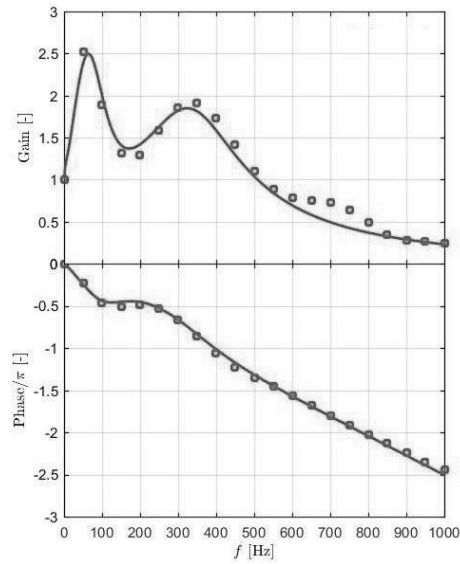


Fig. 2.19 FTF for 25% H₂, 75% CH₄ fuel composition

2.5.5. Boundary Condition

It is necessary to set the boundary conditions to predict the instability characteristic of the partially premixed combustor. The strainer, which is the reference of the inlet, is set to open boundary because it is open about 46% of the total area. In addition, the plug nozzles that make the acoustic boundary while adjusting the length of the combustor are taken as the closed boundary. In addition, boundary conditions of the inlet were applied similar to the experimental conditions, using the reflection coefficients obtained from the combustion experiments.

CHAPTER 3

STATIC (NOX & FLAME STRUCTURE)

CHARACTERISTICS OF SNG COMBUSTION

3.1 Objectives and Test Conditions

Power generation with gasification has been changed from using a fossil fuel combustion in order to meet the regulation of limited emission and improve the efficiency of the system. Gasification has advantage that reduce emission such as nitrogen oxide, sulfur oxide and carbon dioxide in exhaust gas. In addition, low-quality fossil fuel is changed into high value gaseous fuel and these fuel increase the efficiency of the power system. The risk of fire, caused by scattered tiny dust when the coal is crushed, transported and stored, is relatively smaller than gaseous fuel. Furthermore, the structure of conventional boiler furnace is larger than that of gas turbine. However, price is high because of the cost including gasification process and enough study of gas fuel combustion have not been carried out, still [52]. The first Korea Gwangyang SNG project was launched in 2010 by POSCO in Korea. The goal of this project is to generate SNG production 500,000 ton in year and 92MWe power generation in gas turbine system [4].

In order to meet this trend of using substitute fuel, researches of gas turbine power generation using SNG, biogas, syngas, and other substitute gases have been performed steadily. S. Dodo et al. investigated that NO_x emission is allowed to be less 10 ppm in dry low NO_x gas turbine combustor with hydrogen rich syngas fuels [53]. S. Park et al. studied that NO_x emission and the combustion efficiencies of three kinds of SNG with different hydrogen content are almost identical at the same load [54]. The flame length decreases by 3.2% and the flame angle based on the dump plane increases by 4.2% with respect to increase hydrogen content to 3% in volumetric ratio. In addition, pattern factor defines ratio of peak temperature and average temperature. S. Goke et al. carried out flame structure characteristics, stability and NO_x generation mechanism using reactor network

on a rich-quench-lean and premixed combustor with steam dilution. High steam dilution ratio enable to lower risk of flashback for hydrogen-containing fuel [55].

K. Kim et al. studied that V-flame geometry is modified to an M geometry when the flame propagation speed increases in premixed gas turbine combustor [28]. Furthermore natural gas flames with high hydrogen mole fractions can make more stable in terms of combustion dynamics. Flame transfer function (FTF) is defined thermoacoustic network modeling to predict self-induced combustion instability and represented as the normalized ratio of heat release and velocity fluctuations, as shown in Eq. (1)

$$FTF = \frac{Q'(f)/\bar{Q}}{v'(f)/\bar{v}} \quad (3.1)$$

Where, Q is about the heat release rate, V is the mixture velocity in the mixing section, and f is forcing frequency by pulsator such as siren and speaker. Methanation is a chemical process in SNG gasification to make methane from a mixture gas of carbon monoxide and hydrogen or carbon dioxide and hydrogen. CO shift exchange carbon monoxide to carbon dioxide using water or hydrogen. Therefore, gasification process can make various gaseous fuels and use these fuels for different compositions [56]. Dilutions in combustion such as nitrogen, carbon dioxide, and steam are very effective in reducing the flame temperature and thermal NO_x emissions [57]. As well as, these diluents are a byproduct from the gasification process, therefore it is easy to use in SNG power plant.

In this study, NO_x and CO emission characteristics, and combustion instability are investigated for SNG compositions in increasing hydrogen ratio on gas turbine combustor using Abel-inversed OH chemiluminescence images [58]. Nitrogen and carbon dioxide dilution experiments are conducted with increasing from 0% to 200% with respect to the amount of fuel in partially premixed gas turbine combustor.

Table 3.1 Combustor load test condition.

	unit	ref	C1	C5	C10	C15
H ₂	Vol%	0	1	5	10	15
CH ₄	Vol%	100	93.8	88.1	80.9	74.2
C ₃ H ₈	Vol%	0	5.2	6.9	9.1	10.8
WI	MJ/Nm ³	55.3				
Eq	-	0.5~1.0				
Load	kW	25.4/38.1/50.8/63.5				
DR	%	0~200(N ₂ ,CO ₂)				

Table 3.1 is the test condition for this research. C1, C5, C10 and C15 listed in Table 3.1 have hydrogen fuel composition of 1%, 5%, 10% and 15% based on heating value, respectively. Wobbe index (WI) is the parameter comparing the combustion energy output of different composition fuel gases in an appliances. WI expresses higher heating value over square root specific gravity. Furthermore, propane gas is adjusted to maintain the WI of each test conditions.

Equivalence ratio varies from 0.5 to 1.0 in increments of 0.1 by shifting the air flow rate with a fixed fuel flow rate. The power load are 25.4, 38.1, 50.8 and 63.5kW, which is calculated using the lower heating values of the fuel composition and dilution ratio (DR) represented the ratio of the flow rate of diluent and sum of flow rate of the fuel, as shown in Eq. (3.2). Nitrogen and carbon dioxide are used as a diluent in this study and supplied into air feed line from 0% to 200%.

$$DR_{N_2} = \frac{\text{flow rate of } N_2 \text{ [slpm]}}{\text{sum of flow rate of fuel [slpm]}} \quad (3.2)$$

A PI-MAX ICCD camera is used for flame visualization through the quartz section and an OH* band-pass filter is applied on the camera to investigate OH chemiluminescence distribution in the flame zone. Abel deconvolution method is also

used to obtain two-dimensional information from line of sight overlapped images.

3.2 Emission (NO_x and CO) Characteristics of SNG Combustion without N₂ and CO₂ Dilutions

NO_x emission is increased with the equivalence ratio and heat input as shown in Fig. 3.1. These NO_x emissions are effected flame temperature related in the equivalence ratio and heat load. However, there is no great difference NO_x emission compared with the gap of hydrogen content in SNG compositions at the same heat load. This is the effect of the Wobbe index of the above mentioned experimental method. Figure 3.1 is the averaged NO_x emission each heat load. It shows that large NO_x emissions generate on the high heat load condition, therefore diluents such as nitrogen and carbon dioxide need to lower flame temperature.

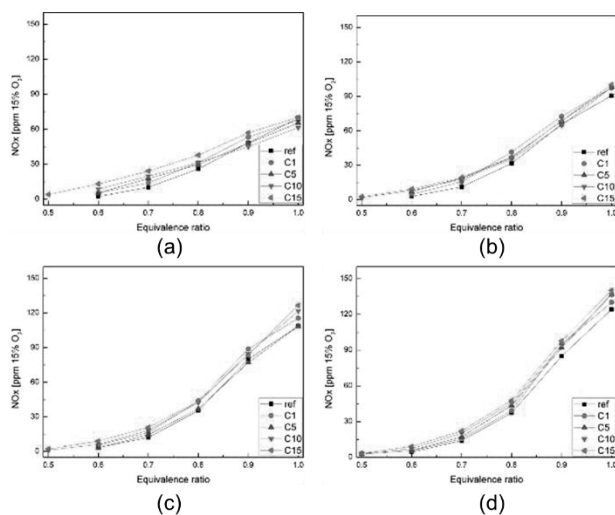
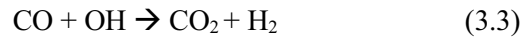


Fig. 3.1 NO_x emission characteristics of SNG combustion without N₂ and CO₂ diluents with hydrogen compositions.

(a) 25.4kW, (b) 38.1kW, (c) 50.8kW, (d) 63.5kW

CO emission is different trend from the NO_x emission. Figure 3.1 is the CO emission characteristics each heat load with respect to the equivalence ratio. CO emissions maintain under 5 ppm@15%O₂ up to stoichiometric condition and then increase at the stoichiometric condition steeply some cases. In methane-air chain reaction, the oxidation of CO is the final chemical reaction of hydrocarbon combustion. The CO-O₂ oxidation is very slow by itself, however small quantities of steam or hydrogen can induce fast reaction by generating hydroxyl radical (OH). Much of the heat release generate in the hydrocarbon fuels reaction. Equation (3.3) is the process of the CO oxidation [59].



The OH radical affects the CO oxidation directly. To investigate a reason of a lot of CO emission in some SNG compositions, maximum OH intensity of the flame images is compared as shown in Fig. 3.1. Dotted circles indicates the conditions where the CO increase steeply. CO emission decreases with increasing heat load because CO chemical reaction is occurred well at the high flame temperature and a lot of OH radical accelerate the CO oxidation. Maximum OH intensity decrease in the region where CO emission increase rapidly. The reduction of OH radical induces CO-O₂ reaction suppression, which CO as the incomplete combustion by-product is emitted to the atmosphere as a state not converted to CO₂. These trends are displayed in ref and C1 fuel composition, which hydrogen ratio is relatively small, that is consisted a high percentage methane relatively. Mixing near the injector does not occur efficiently in the high methane ratio in SNG composition for the heavy methane molecular weight relative to the hydrogen fuel. Poor mixing suppresses the uniform flame and OH generation. Thus, CO emission increases in accordance with these effects.

3.3 NO_x Reduction Characteristics of SNG Combustion with N₂ and CO₂ Dilution

High flame temperature in combustion zone affects adverse effect on exhaust emissions. Dilution is the method to solve the problem. In this study, nitrogen and carbon dioxide are used to lower flame temperature supplying air line and investigate the combustion characteristics of SNG. NO_x reduction is defined the difference between NO_x emission without diluent and NO_x emission with diluent in ppm 15% O₂ shown by the following equation.

$$\text{Diluent reduction [ppm 15\% O}_2\text{]} = (\text{NO}_x \text{ without dilution}) - (\text{NO}_x \text{ with dilution}) \quad (3.4)$$

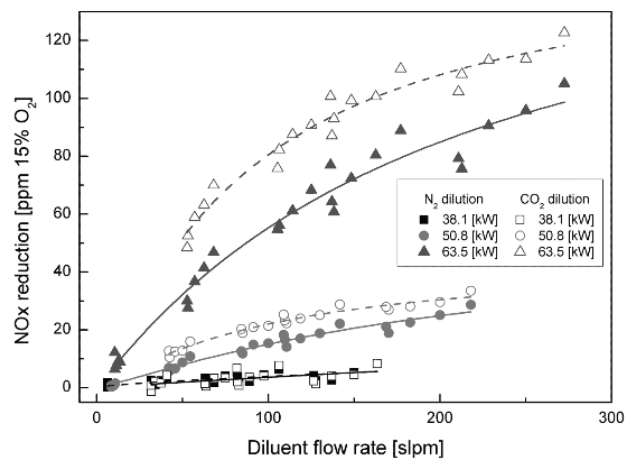


Fig. 3.2 NO_x reduction with diluent of N₂ and CO₂.

Fig. 3.2 is the NO_x reduction with respect to diluent flow rate of nitrogen (circle) and carbon dioxide (blank) on each heat load. The solid line and dotted line are the fitting line of NO_x reduction each experimental condition. NO_x reduction increases logarithmically as diluent flow rate increase and the trend appears in high heat load

definitely. It seems to show carbon dioxide is more effective to reduce NOx emission than nitrogen from Fig. 3.2. However, the NOx reduction in partially premixed gas turbine combustion is related to the diluent heat capacity rather than the kind of diluent gas. Diluent does not have any influence on the chemical reaction. The heat capacity is calculated on diluent mass flow rate and specific heat of the diluent as shown Eq. (3.5).

$$\text{Dilution heat capacity [J/Ks]} = \dot{m}_{\text{diluent}} \cdot C_{p,\text{diluent}} \quad (3.5)$$

Table 3.2 Diluent specific heat on 500K

@500K		N ₂	CO ₂
C _p	[kJ/kg K]	1.07	1.06
	[kJ/mol K]	29.96	45.58

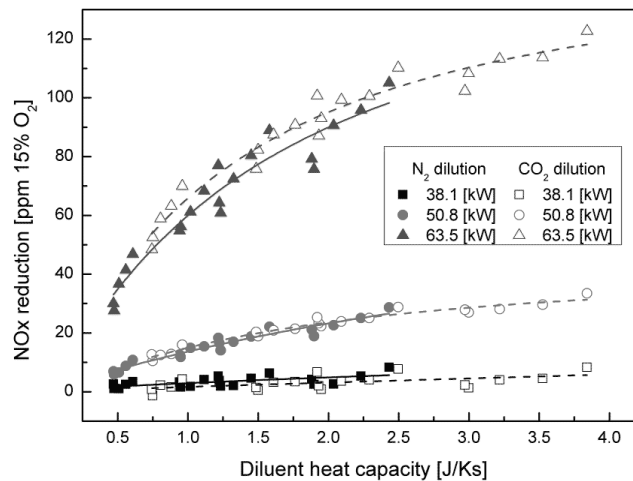


Fig. 3.3 NOx reduction with respect to the diluent heat capacity of N₂ and CO₂.

Table 3.2 is the specific heat of each diluent. High heat capacity of the diluents stores more heat at the same heat load and reduce flame temperature, as a result, NOx emission decrease. Fig. 3.3 shows the effect of diluent heat capacity and demonstrates that NOx

reduction is the function of the diluent heat capacity and heat load. The heat capacity of carbon dioxide diluent is much larger than that of nitrogen at the same mass flow rate, because specific heat of carbon dioxide is large relatively. Therefore, Small amount of carbon dioxide has the similar effect as a large amount of nitrogen diluent.

3.4 Dump Plane Temperature and Flame Structure

Dump plane temperature is measured to investigate the effect on the combustion instability. Combustion instability is defined as higher than 5% fluctuation of static pressure in combustor. In this study, 0.15 psi is selected as the criteria of the combustion instability. Fig. 3.4 is the dump plane temperature with respect to the root mean square (RMS) amplitude of the pressure on combustion zone in 50.8kW without dilution. Dump temperature is formed below the 500°C in stable conditions, however the temperature increases in combustion instability because the flame vibrates back and forth and reach the dump plane.

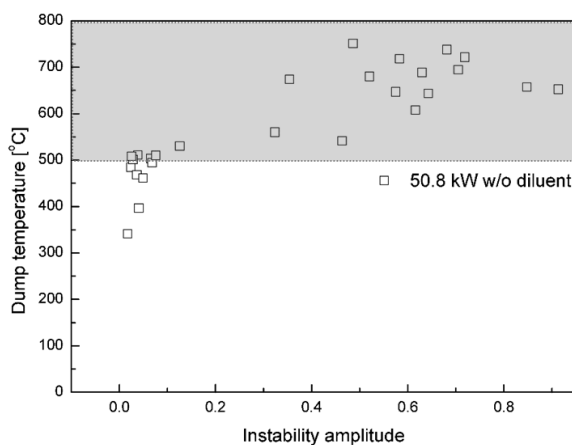


Fig. 3.4 Dump plane temperature on combustion instability.

Table 3.3 is Abel-inversed OH chemiluminescence images of 50.8kW without dilution. All of images show outer recirculation zone and the recirculation zone influence

on the dump plane temperature as well. Flame length decreases with increasing hydrogen ratio of fuel composition from ref to C15. In addition, OH intensity on equivalence ratio 1 is lower than equivalence ratio 0.9 as identified above Fig. 3.4. Although the flame length is shorter, the amount of heat released from the flame is relatively high due to the same heat load [60]. Therefore, OH intensity of high hydrogen content fuel composition is stronger relatively.

Table 3.3 Abel-inversed OH-chemiluminescence images in 63.5kW heat load without dilution.

E.q	ref	C1	C5	C10	C15
0.5					
0.6					
0.7					
0.8					
0.9					
1.0					

CHAPTER 4

HIGH FREQUENCY TRANSITION

CHARACTERISTICS OF SYNTHETIC NATURAL

GAS (H₂/CH₄) COMBUSTION

4.1 Objectives and Test Conditions

Renewable and alternative fuels such as synthetic gas (syngas; composed of H₂ and CO), synthetic natural gas (SNG; composed of H₂ and CH₄), and biomass are promising solutions to global climate issues. In the research field of gas turbines, interest in such energy resources has increased in recent years. Conventional burners use solid fuels such as coal, are inefficient, and emit a large amount of pollutants, including soot, which is the final product of combustion. SNG plants have recently been highlighted as an alternative to conventional burners. An SNG plant converts coal into gaseous fuel while applying the carbon capture and storage (CCS) technique, which eliminates the need to remove carbon and sulphur [61]. SNG as fuel is stable and storable, and leads to fewer emissions because methanation and CO shift remove the CO and CO₂ generated by coal oxidation. The first SNG plant was built in North Dakota, USA, and 15 plants are in operation today [62].

A gas turbine system has many advantages. For example, renewable resources can be used in it, and it is highly efficient (60%) when combined with a steam turbine. Moreover, the duration between the starting of the engine to its attainment of maximum power is relatively short compared with that in a conventional burner. The size of the system is not too large either, i.e., the site for a gas turbine plant need not be vast. However, emissions and combustion instability have recently been identified as problems in gas turbine systems because the operation environment involves a high pressure and temperature.

NO_x and CO are exhaust gas emissions that cause pollution and the destruction of

the ozone layer. NO_x is generated through three mechanisms (thermal, prompt, and fuel NO_x); however, about 80%–90% of the generated NO_x is thermal NO_x, which is generated in high-temperature environments in combustors [8]. NO_x emission irritates the human eye and respiratory system, in addition to destroying plants and causing acid rain. CO is emitted as a colourless and tasteless gas, and is the most common cause of fatal air poisoning in many countries [63]. Therefore, it is important to study the characteristics of such emissions and ways to reduce them.

Combustion instability occurs through interactions between pressure and heat-release oscillation in a combustor. When the oscillation is too high, the combustor's liner and the blade of the turbine can be damaged. Even at a low amplitude of combustion instability, the oscillation may have a high amplitude. Therefore, it is important to investigate the characteristics of combustion for various fuel compositions and combustor geometries.

Many research groups have studied combustion in gas turbines to understand the emission characteristics and combustion instability of fuels having various compositions. Cheng et al. reported that NO_x emissions are linearly dependent on the temperature of the adiabatic flame in low-swirl-injected lab-scale gas turbine combustion. They observed a shift in a lifted low-swirl flame at the exit of the nozzle with increasing H₂ content in the fuel, and the flame was observed to attach onto a dump plane for 100% H₂ fuel [64]. Coppens et al. experimentally studied NO concentration in various flame shapes and found that NO concentration is a function of the equivalence ratio. The Zeldovich thermal NO_x mechanism was found to be dominant in stoichiometric conditions, whereas the Fenimore prompt NO mechanism was dominant for equivalence ratios ranging from 1.3 to 1.4. A high H₂ content of the fuel did not affect NO concentration in lean flames, whereas the NO concentration in rich flames decreased considerably with increasing H₂ content [65].

In the context of combustion instability, Shanbhogue et al. experimentally studied a fixed-swirl-angle combustor at atmospheric pressure and temperature. Combustor transitions to periodic oscillation occurred as the equivalence ratio increased to 0.65 [13].

Dowling and Langhorne et al. pointed out that low-frequency instability of combustion occurs in the afterburner of aero-engines with a high equivalence ratio, and it is called reheat buzzing instability [19, 20]. Figura et al. reported that the centre of heat release is an important factor for predicting combustion instability. The centre of heat release moves with respect to the operation conditions and fuel composition [68]. Lee et al. found that the convection and skewness time are key parameters determining frequency mode shift. They conducted an experimental study in a gas turbine combustor and applied OH PLIF and POD to determine reasons for the frequency mode shift phenomenon [69]. Moreover, many researchers have studied the characteristics of combustion using experimental [23–31], analytic [32, 33], and computational [24, 34, 35] approaches.

This study investigates the characteristics of frequency mode shift for various combustor lengths, heat loads, and fuel compositions (H_2/CH_4 ratio). To investigate reasons for the frequency mode shift, a high-speed camera was used to obtain OH* chemiluminescence images and the Abel inversion process was applied. The laminar burning velocity of the flame was also calculated to investigate the relation between convection time and frequency mode shift [83].

A model gas turbine combustor was manufactured for the experimental study, as shown in Fig. 2.2. The flow rates of fuel and air were controlled using mass flow-rate controllers (MFC; air: Bronkhorst, F-206BI, fuel: Parker, Porter-200), and an air heater constantly supplied heated air at a temperature of up to $200 \pm 3^\circ C$. The fuel consisted of H_2 and CH_4 , which were mixed in the MFCs. The fuel mixture was injected into the combustion zone through 14 holes, each measuring 1.78mm in diameter, in the cross air flow jet pattern. The injection holes were located 2.7mm upstream of the dump plane, which can make partially premixed flame. The swirl vane was angled at 45° , and the swirl number of the nozzle was approximately 0.8. To visualize the flame, a circular quartz tube was installed at the front of the combustor's dump plane. Cooling air ($V_{cooling_air} = 900$ slpm) was injected onto the quartz surface to avoid thermal damage from the flame. A plug nozzle blocked 90% of the combustor's outlet to create an acoustic boundary, and could move back and forth. The combustor's length was defined as the distance between

its dump plane and the plug nozzle because the fuel–air nozzle also had an acoustic boundary. The definition of the combustor length was validated by comparing the frequency of experimental instability to the calculated longitudinal instability mode frequency obtained using this length. Eleven dynamic pressure sensors (PCB 102A05) and five thermo-couples (K type and R type) were used to measure the fluctuating pressure and temperature, respectively, and their positions are shown in Fig. 2.2.

A gas analyser (TESTO 350K) was set up to measure the exhaust emissions of NO_x in dry gas using a drying sampling tube (NO_x sensor; measurement range: 0–4,000 ppm, resolution: 0.1 ppm) and CO (CO sensor; measurement range: 0–10,000 ppm, resolution: 1 ppm). NO₂ is more stable than NO, and NO is continuously converted to NO₂ by reacting with O₂ in the high-temperature combustion zone. Therefore, the measurement of exhaust emissions must be made at the final stage of the combustor to obtain accurate results. For this purpose, the sensing probe of the gas analyser was installed at the rear of the combustor, where the chemical reaction had been completed.

A high-speed ICCD camera (High-speed star 8; 1024 × 1024 pixels, 1 kHz) with an intensifier (High-speed IRO) was used to capture images of the flame through a quartz tube. An f/2.8 UV lens and an OH bandpass filter (307 ± 10 nm) were installed on the camera to obtain chemiluminescence signals of the OH radical. The OH chemiluminescence signal represented the heat-release characteristics of the combustion zone. In other words, this signal could be used to identify the structural characteristics of the flame.

To obtain maps of the combustion stabilities of H₂ and CH₄ (purity; H₂ > 99.5mole%, CH₄ > 99.5mole%) on the model gas turbine combustor, several variations were selected in this study. The combustion air temperature was 200 ± 3°C, and the mass flow rate was 0.02 kg/s (volume flow rate: 1,100 slpm). Thermal loads of 35 kW, 40 kW, and 45 kW were considered to study the relation between thermal load and combustion instability. Since the test was conducted at a lab scale, the test pressure was maintained at 1.1–1.3 atm depending on the fuel composition because of the instantaneous combustion pressure in the combustion zone and the acoustically closed plug nozzle. Moreover, the H₂ and

CH₄ contents were varied, and the H₂ ratio was defined as the ratio of the volumetric flow rate of H₂ to the sum of those of H₂ and CH₄. The fuel compositions varied from 100% CH₄ to 100% H₂. In other words, the H₂ ratio was varied from 0% to 100% in increments of 12.5%. The combustor's length was the main variable in this study because the geometric conditions of the combustor influenced the mode frequency of combustion instability; the length was varied from 1,160 mm to 1,400 mm in increments of 15 mm. Table 4.1 summarizes the experimental conditions. To determine the characteristics of the flame under these test conditions, images of the flame, mode analysis, and CANTERA-MATLAB were used.

Table 4.1 Experimental test conditions.

Parameter	Values
Fuel	H ₂ , CH ₄
Air flow rate	0.02 kg/s (1,100 slpm)
Air temperature	200°C (= 473 K)
Heat load	35 kW, 40 kW, 45 kW
Combustor length	1,160 mm–1,400 mm
H ₂ ratio $[\frac{H_2}{H_2+CH_4}]$	0%–100%

4.2 Experimental Methods

Emissions of exhaust gases such as NO_x and CO were converted from their original values to 15% O₂ correction by using Eq. (4.1) to compare the experimental results.

$$Emission_{ppm @ x\% O_2} = (Emission_{meas.}) \times \left\{ \frac{20.9 - x}{20.9 - 100 \cdot (O_{2,meas.})} \right\} \quad (4.1)$$

Here, $emission_{meas.}$ denotes the emission measured by the gas analyser, and x is the conversion value. The objective of this conversion was to regulate NOx or CO emissions from the gas turbine, heater, and boiler systems [79]. The conversion value was 3% O₂ in the case of the heater and boiler, whereas it was 15% O₂ in the case of the engine and the gas turbine [84].

To analyse the mode frequency, Eq. (4.2), which represents the longitudinal mode frequency in the case of closed boundary conditions, was used to calculate the instability frequency:

$$f = \frac{n \cdot c}{2 \cdot L_c}, \quad n = 1, 2, 3, \dots, c = \sqrt{\gamma \cdot R \cdot T_c} \quad (4.2)$$

γ is the adiabatic index, R is the gas constant, L_c is the combustor length from the dump plane to the acoustic plug nozzle, and c is the speed of sound in the combustion zone. The temperature used in Eq. (4.2) was obtained from the experimental data. The value of T_c was calculated based on the mean value of the temperature measured using the thermo-couple installed from the dump plane to the plug nozzle.

The Abel inversion process was applied to obtain two-dimensional (2-D) images from 3-D accumulated images that were acquired using a high-speed camera. To capture the averaged flame images, the high-speed camera captured images for one second at a rate of 1- kHz with full CCD resolution. The averaged images were calculated using cross-sectional radical information [85].

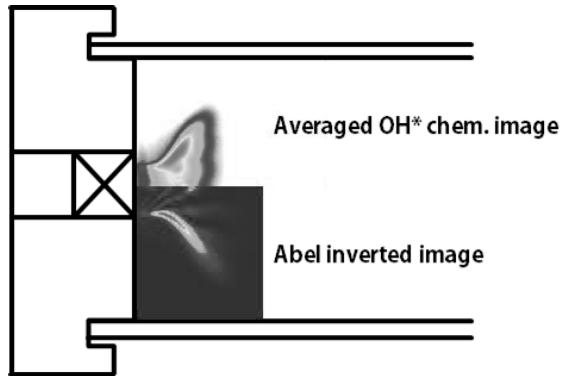


Fig. 4.1 Time-averaged OH chemiluminescence and Abel-inverted image at a heat load of 40 kW, H₂ ratio of 75%, and combustor length of 1,400 mm.

Figure 4.1 shows a time-averaged OH chemiluminescence image and its Abel-inverted image under a heat load of 40 kW, an H₂ ratio of 75%, and combustor length of 1,400 mm.

4.3 Exhaust Gas Emission

The emission index of nitric oxide (eiNO_x) is defined as grams of NO_x emitted per kg of burned gas, which can be used as an indicator of the exhaust gas in various combustion environments. It is important in combustion research to determine the eiNO_x data at the scaling formulation to predict the amount of NO_x emissions because it is the relative value used to compare varying compositions of fuel [86].

$$eiNO_x = \frac{-\int M_{NO_x} \dot{\omega}_{NO_x} dx}{-\int M_{fuel} \dot{\omega}_{fuel} dx}$$

where M denotes the molecular weight of each gas and $\dot{\omega}$ is the production or consumption rate in the combustion zone.

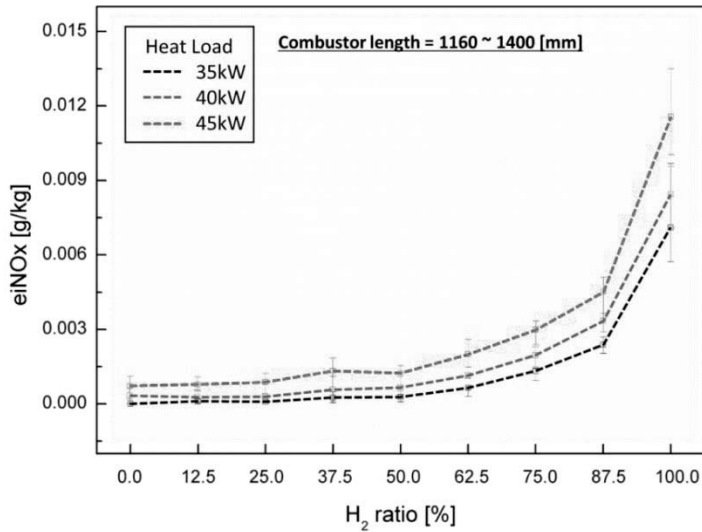


Fig. 4.2 Characteristics of eiNO_x emission with respect to H₂ ratio and heat load.

Figure 4.2 shows the experimental results for heat loads of 35 kW, 40 kW, and 45 kW for different lengths of the combustor. The average emission values at each test condition are represented by the dotted line, and the minimum–maximum values are plotted in Fig. 4.2. Relatively high eiNO_x emissions were observed at a high heat load and high H₂ ratio at the tested combustion temperature. The thermal NO_x mechanism was the major one in NO_x generation in these experimental tests. The adiabatic flame temperature was higher than 1,200°C under all test conditions. The caloric value of the H₂ fuel was greater than that of the CH₄ fuel. In other words, a higher ratio of H₂ resulted in a higher flame temperature. The variation in combustor length from 1,160 mm to 1,400 mm did not influence the characteristics of NO_x emission. According to the mechanism of thermal NO_x (Zeldovich’s mechanism), its temperature and time of residence in the combustion zone determined the characteristics of NO_x emission. That is, the chemical reaction in the combustion zone is important for these characteristics. However, the length of the combustor used in this study was greater than the flame length. The eiNO_x associated with a non-premixed turbulent jet flame is proportional to the global residence time L_F/U_F . However, the fuel-air injector used in the experiments was of a partially premixed injecting type with strong swirl number in

spite of a very short mixing length. The swirl number can be calculated from Eq. (4.4).

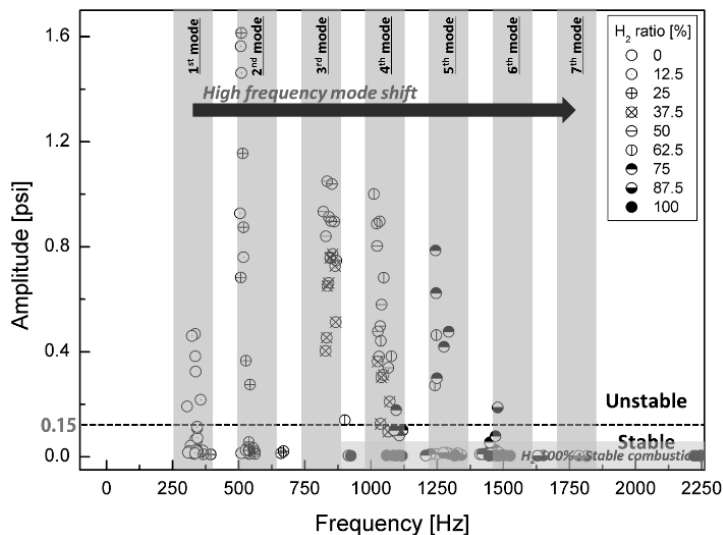
$$S_n = \frac{2}{3} \left[\frac{1 - (D_{swirl-in}/D_{swirl-out})^3}{1 - (D_{swirl-in}/D_{swirl-out})^2} \right] \tan\phi \quad (4.4)$$

D_{swirl_in} , D_{swirl_out} , and ϕ are the inner diameter of the swirler, the outer diameter of the swirler, and the swirl vane angle, respectively. From Eq. (4.4), the swirl number is about 0.83, which is sufficiently high to make a premixed flame. Therefore, eiNO_x was mainly influenced by the flame temperature, which is determined by thermal NO_x (Zeldovich's mechanism), rather than flame length.

In the case of H₂ flame, the flame length was shorter than the CH₄ flame length. When the H₂ ratio was higher, a higher eiNO_x was measured because the eiNO_x strongly depended on the flame temperature, rather than the combustor length, in the experiments. Therefore, the variation in combustor length in this study did not affect the flame shape, length characteristics, and flame temperature. Consequently, the combustor length did not affect the thermal characteristics of the emission of NO_x.

In contrast to the characteristics of the emissions of NO_x, CO emission was less than 3 ppm under all test conditions. CO was generated by incomplete combustion. The equivalence ratio in the test ranged from 0.4 to 0.6. Therefore, if all reactants were well mixed, the amount of CO emission was small. The gas turbine combustor had a partially premixed nozzle with a short mixing length. Nevertheless, the swirled vane intensified swirling flow, and the fuel and air mixed well. Therefore, CO emission was negligibly low for all experimental conditions.

4.4 Mode Shift Phenomenon in Combustion Instability with Respect to the H₂ Ratio



(a)

H ₂ ratio	0%	12.5%	25%	37.5%	50%	62.5%	75%	82.5%	100%
OH* radical									
Flame length	64 [mm]	41 [mm]	34 [mm]	27 [mm]	19 [mm]	18 [mm]	15 [mm]	14 [mm]	12 [mm]

(b)

Fig. 4.3 (a) Mode analysis based on the amplitude of a dynamic sensor, and (b) flame structure with respect to H₂/CH₄ ratio and combustor length at a heat load of 40 kW.

Figure 4.3 (a) shows the maximum amplitude of the fast Fourier transform (FFT) at the third dynamic pressure sensor (DP3), which was placed on the dump plane, where dynamic pressure data were measured for one second. Figure 4.3 (b) shows radial images of the flame's OH chemiluminescence and flame length, which was post-processed by the Abel transform. The combustion instability criterion was defined as a root mean square (RMS)

value of the FFT amplitude higher than 0.15 psi. As per legislation, the criterion of industrial gas turbine combustion instability was an oscillation of static pressure of the combustor liner greater than 3%–5% [87].

The frequency of the theoretical longitudinal instability of the combustor is represented by the grey rectangular area in Fig. 4.3 (a) because the combustor length affected the longitudinal frequency mode. The experimental conditions are denoted by circular marks. The flame length was calculated using the OH* radial images and was defined as the distance between the dump plane and the flame center of OH* intensity. The combustion instability frequency mode shifted from the first to the seventh mode as the H₂ ratio increased from 0% to 100%. However, the amplitude of combustion instability for 100% H₂ fuel was low compared with that for the other test conditions in which CH₄ was included in the fuel. Almost all instability amplitudes of 100% H₂ fuel were under 0.01. Convective time was an important parameter for combustion instability in time-lag analysis. It was also directly influenced by and proportional to the flame's length. If the flame is very short, the convective time is short as well. This process rendered very short the time between a fluctuation in the heat released by the flame and that in its pressure in the combustion zone. Therefore, H₂ with a high burning velocity affected the high-frequency mode shift of combustion instability. The effect of H₂ composition on the frequency of combustion instability has been studied by many research groups. Lieuwen claimed that the mixture velocity of fuel and air at the inlet affected the frequency mode shift [88], and Yoon reported the importance of convective time as a parameter of instability frequency [89]. The total time delay consisted of various delay times (acoustic time, convective time, ignition time, and so on). Higher-frequency transition phenomena mainly depend on the convective time among the delay times. In a conventional premixed combustor, the fuel-air mixing length mainly affects the convective time since the mixing length was greater than the flame length. In contrast, the change of the flame length with H₂ ratio in a partially premixed combustor has a major effect on the convective time because of the very short mixing length ($L_{\text{mixing length}} = 2.7 \text{ mm}$).

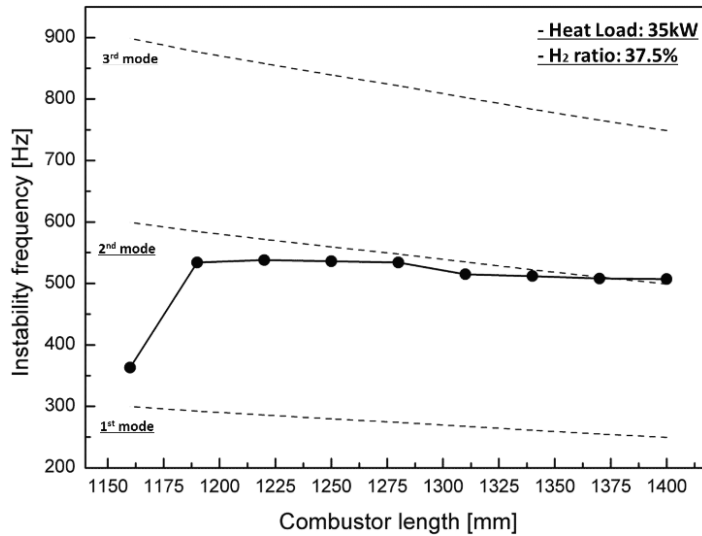
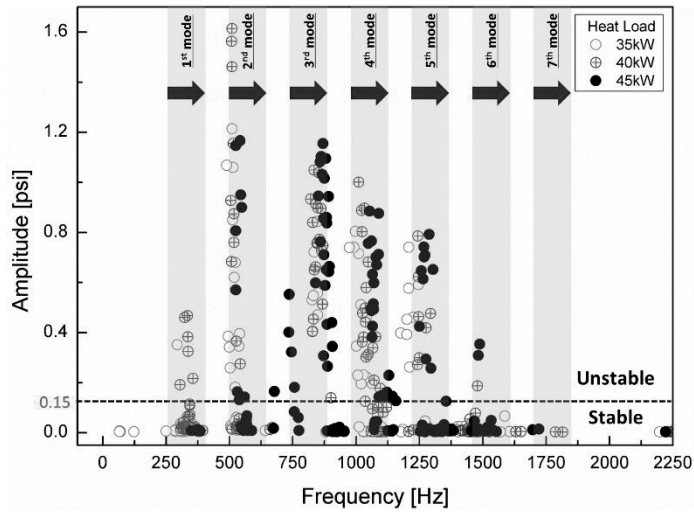


Fig. 4.4 Frequencies of combustion instability for various combustor lengths with a heat load of 35 kW and H₂ ratio of 37.5%.

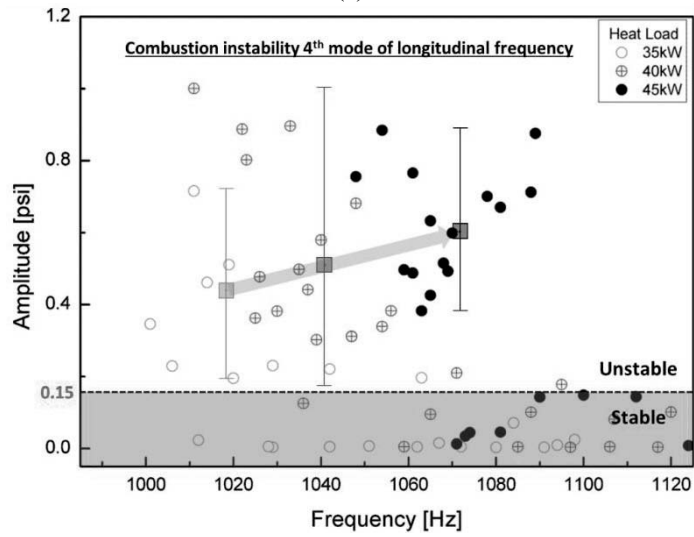
Figure 4.4 shows the frequency of instability during the variation in combustor length from 1,160 mm to 1,400 mm at a heat load of 35 kW and H₂ ratio of 37.5%. The dotted line shows the longitudinal frequency calculated using Eq. (4.2). The theoretically calculated values were overestimated compared with the experimental dataset because the temperature in Eq. (4.2) was used only as the third thermo-couple value in Fig. 2.2. However, the trend of a reduction in frequency in the experimental data was confirmed to be similar to the calculated trend, and the frequency of instability was shown to be the longitudinal mode frequency.

OH-chemiluminescence image acquisition and flame-length calculation were performed as shown in Fig. 4.3 (b) to investigate the effect of convective time of the fuel-air mixture with regard to the H₂ ratio in the partially premixed fuel-air nozzle. In addition, the combustion instability frequency does not shift to a higher mode as the combustor length is changed as in Fig. 4.6, and it is experimentally confirmed that the length of the combustor does not affect the combustion instability and length of the flame.

4.5 Combustion Instability Mode Shift for Different Heat Loads



(a)



(b)

Fig. 4.5 (a) Mode analysis based on the amplitude of a dynamic sensor with respect to the heat load, and (b) a detailed view of the combustion instability of the 4th mode of longitudinal frequency.

Equation (45) is the definition of the Rayleigh criterion, which describes combustion instability:

$$\int_V \int_T p'(x, t) q'(x, t) dt dV \geq \int_V \int_T \sum_i L_i(x, t) dt dV \quad (4.5)$$

where p' is the instantaneous oscillation in the pressure of the combustor, q' is the heat-release oscillation, and L is the loss of acoustic energy through processes such as damping and viscous dissipation [90]. When the value of the right-hand side of Eq. (4.5) exceeds that of the left-hand side, combustion instability occurs. In other words, the increase in the heat load increases the heat-release oscillation in the acoustic field, and can increase the amplitude of combustion instability. On the contrary, combustion instability did not occur at a 100% H_2 ratio, even though a high heating value of H_2 was applied. Hydrogen has a high burning velocity and high extinction rate compared with CH_4 ; that is, a flame containing a high H_2 composition is not easy to extinguish, and thus, the heat-release oscillation was low. Therefore, a 100% H_2 fuel flame was very stable.

Figure 4.5 (a) shows the results of the instability FFT mode analysis under all experimental conditions for heat loads of 35 kW, 40 kW, and 45 kW. In the unstable region, the characteristics of instability frequency were similar at all heat loads in the same longitudinal mode. The increase in heat increased the flame temperature in the combustion zone and q' in Eq. (4.5), which induced a pressure fluctuation (p'). The temperature of the combustion zone increased the speed of sound of the combustion product, which is c in Eq. (4.2). Therefore, the frequency of combustion instability increased at the same harmonic mode as the longitudinal mode. Moreover, the amplitudes of combustion instability increased with respect to the heat load, as shown in Fig. 4.5 (b). The amplitude of combustion instability is related to the coupling between the fluctuation in pressure and that in heat release. Therefore, increasing q' does not necessarily increase p' . However, when the phase between p' and q' was the same under various heat-load conditions, the

amplitude of combustion instability was theoretically proportional to heat release. Therefore, the average amplitude of combustion instability at the same heat-load conditions increased with respect to this increase. The rate of fuel flow was low compared with that of air flow, and heat load was controlled to adjust fuel flow at a fixed rate of air flow. The variation in the velocity of the fuel–air mixture was small for each heat load at the inlet. Therefore, the heat load did not affect the frequency mode shift. Figure 4.6 shows the length and structure of the flame. As mentioned above, when the flame length was similar, the frequency mode shifting of combustion instability did not occur under different heat loads.

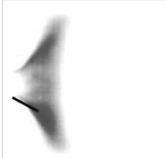
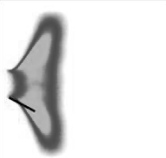
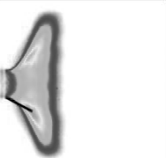
	35kW	40kW	45kW
OH* radical			
Flame length	23.3 [mm]	22.6 [mm]	24.4 [mm]

Fig. 4.6 Length and structure of the flame at varying heat loads (35, 40, and 45 kW).

The laminar flame speed was the velocity at which the flame propagated through unburned reactants in the combustion zone. Flame length was dependent on the speed of the laminar flame and affected convection time ($\tau_{\text{conv}} = L_{\text{flame}} / U$) in time-lag analysis [91]. Figure 4.7 shows the characteristics of calculation of the laminar flame speed using GRI-3.0 in CANTERA-MATLAB code, where it was assumed that the fuel–air mixture was well mixed in the reactor and combustion was complete. The speed of the laminar flame affected the frequency mode shift from the fundamental mode to the sixth mode of longitudinal frequency. When this speed increased, convection time decreased because the flame length decreased. A higher H_2 ratio and heat load increased the laminar flame speed by increasing the temperature of the combustion zone. In other words, the interval between the fluctuation

in the fuel–air mixture in the combustion zone and that in heat release was shorter than the convection time. Therefore, the frequency mode was proportional to the speed of the laminar flame.

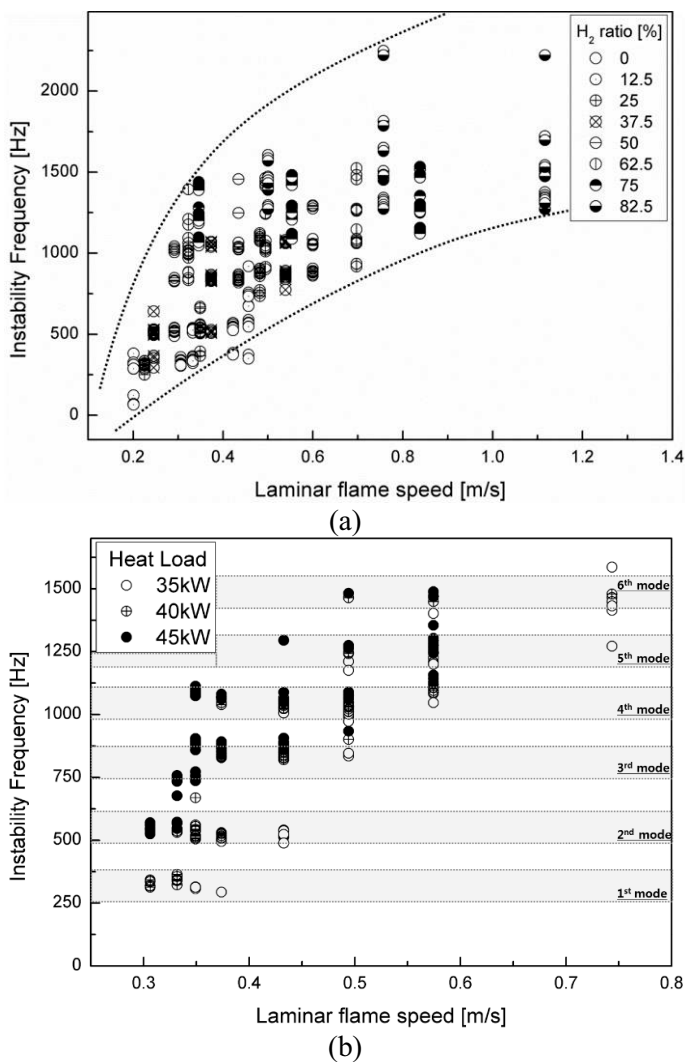


Fig. 4.7 Instability frequency with respect to the speed of the laminar flame for different (a) H₂ ratios and (b) heat loads.

4.6 OH* Chemiluminescence (Flame) Characteristics

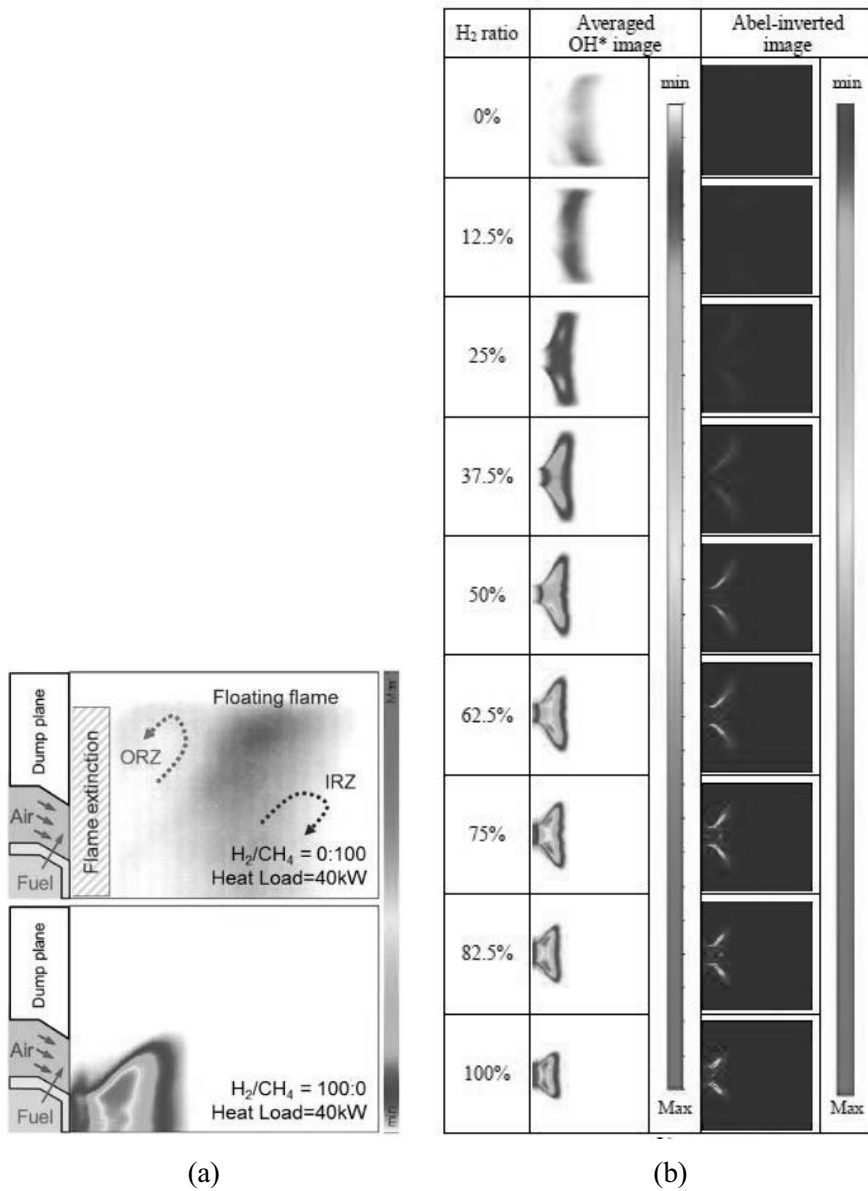


Fig. 4.8 (a) Flame-structure characteristics between CH₄ and H₂ flames
 (b) Time-averaged OH* chemiluminescence and Abel-inverted images
 at a combustor heat load of 40 kW and a length of 1,400 mm.

To investigate the characteristics of the flame, OH chemiluminescence images were acquired by using a high-speed ICCD camera; 500 pairs of instantaneous images were averaged, as shown in Fig. 4.8. Fuel with a relatively high H₂ content had a higher burning velocity than CH₄. That is, a high H₂ ratio rendered the flame short, and it shrunk onto the dump plane (burning velocity; H₂: 289 cm/s, CH₄: 37 cm/s). In addition, the CH₄ flame was more likely to be blown out than the H₂ flame because the CH₄ flame fluctuated near the fuel-air nozzle owing to the low burning velocity. However, the flame was anchored in the dump plane, as shown in Fig. 4.8 (a), by the outer recirculation zone between the long CH₄ flame and the quartz tube wall and the inner recirculation zone. In contrast, the H₂ flame exhibited a wider range of stable flames owing to the increased hydrodynamic and diffusive thermal instability [92]. Moreover, the intensity of OH chemiluminescence was low because of the broad radial distribution, although the heat load was constant. The mixture velocity is an important parameter that influences flame length. The high heating values of H₂ and CH₄ were 12.76 MJ/Nm³ and 37.75 MJ/Nm³, respectively. In other words, the flow rate of the fuel mixture increased with the H₂ ratio. A high H₂ ratio incurred a high mixture injection velocity at the nozzle, and a relatively long flame was formed at higher heat loads. However, in view of flame structure, the effect of fuel flow rate was smaller than that of fuel composition.

The angle between the dump plane and the direction of main flow was defined as the flame angle. To determine the flame angle in accordance with the H₂ ratio, the radial profiles of the OH radical concentration of the flame were acquired at $y = 8$ mm, $y = 11$ mm, and $y = 14$ mm from the dump plane, as shown in Fig. 4.9. At low H₂ ratios such as 0% and 12.5%, the intensity of the OH radical was barely apparent near the dump plane. Further, the maximum value of OH intensity increased with increasing H₂ ratio at $y = 8$ mm and $y = 11$ mm. However, the maximum value of OH intensity decreased rapidly at an H₂ ratio of 100% at $y = 14$ mm because the flame of the 100% H₂ fuel was shorter than that at an H₂ ratio of 87.5%. Therefore, the radial position of the OH radical was lower.

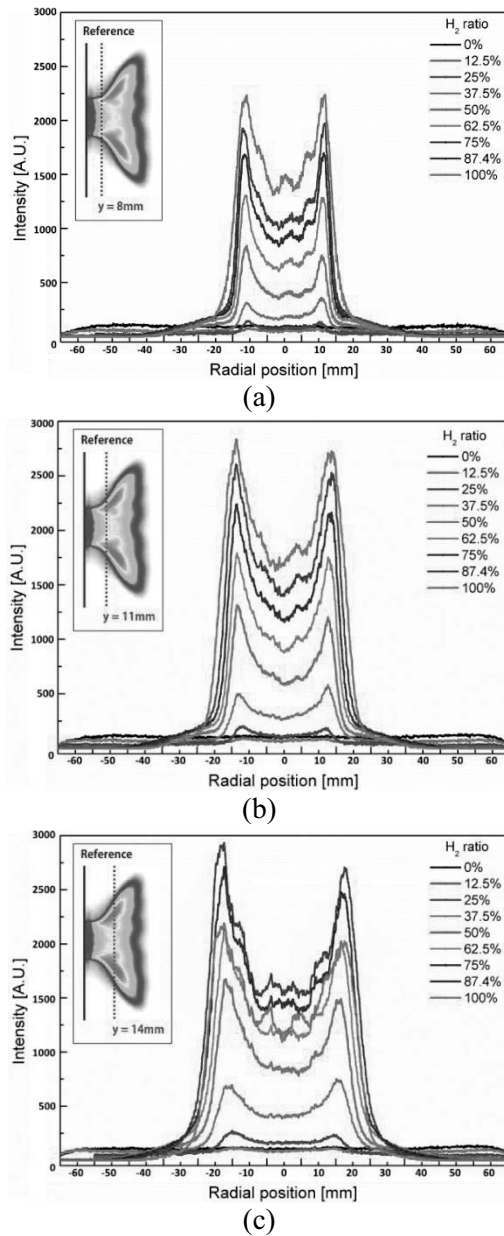


Fig. 4.9 Radial profiles of OH radical concentrations of the flame at a combustor length of 1,400 mm for H_2 ratios of (a) $y = 8\text{ mm}$, (b) $y = 11\text{ mm}$, and (b) $y = 14\text{ mm}$.

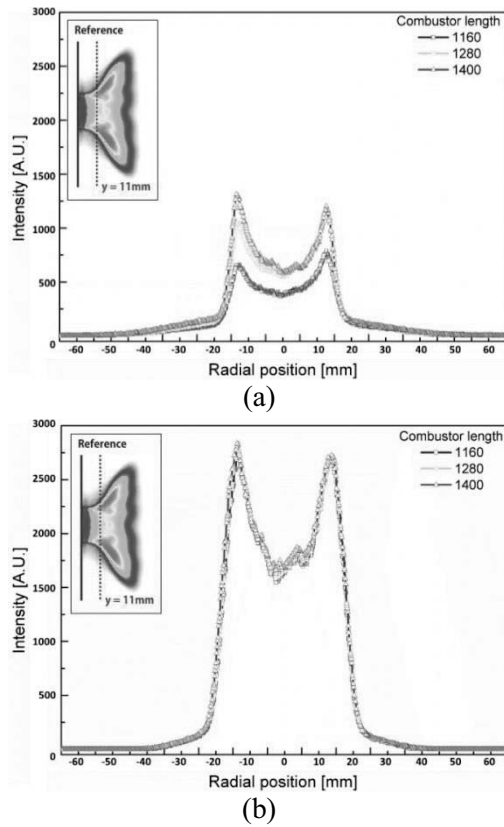


Fig. 4.10 Radial profiles of OH concentration of the flame for different H₂ ratios at $y = 11$ mm from the dump plane. (a) H₂ ratio = 50%, (b) H₂ ratio = 100%.

The variation in flame shapes in accordance with that in combustor length (1,160 mm, 1,280 mm, and 1,400 mm) in the state of combustion instability was analyzed. OH radical profiles were obtained at $y = 11$ mm from the dump plane. A proper distance was selected to obtain the OH radical intensity at which the flame existed under all experimental conditions. Figure 4.10 shows the radial profiles of the characteristics of OH concentration for different combustor lengths: 1,160 mm, 1,280 mm, and 1,400 mm. The OH radical profiles for each length of the combustor in Fig. 4.10 (a) show different shapes, whereas those in Fig. 4.10 (b) show similar characteristics. In terms of the combustion instability phenomenon, the flame strongly vibrated back and forth on the dump plane. On the contrary,

a stable flame formed with similar structural characteristics is shown in Fig. 4.9 (a). To compare the structural characteristics of the flame between stable and unstable conditions, the averaged error was defined as the error between sum of the intensity profiles and the average value of the sum of intensities. This error is shown in Fig. 4.11 with respect to the H_2 ratio.

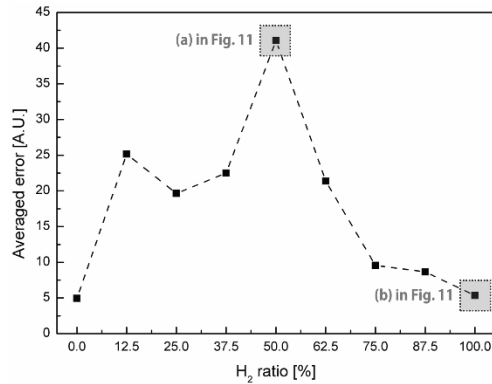


Fig. 4.11 Average error of the radial profiles of OH concentrations of flame for different H_2 ratios at $y = 11$ mm from the dump plane.

A high value of average error implied that the flame shapes were different for different combustor lengths; that is, as the average error was higher than the stable flames. In other words, a lower value of the average error indicated similar OH radical profiles for each combustor length. The average error was low for an H_2 ratio of 0% (similar to that for an H_2 ratio of 100%) because the signal of the OH radical was too low to compare among different combustor lengths. In other words, the distribution of the OH radicals and average error were sufficient to distinguish between a stable state and a state of combustion instability, which is confirmed in Figs. 4.9–4.11.

CHAPTER 5

THERMO-ACOUSTIC INSTABILITY AND FLAME TRANSFER FUNCTION MEASUREMENT

5.1 Background and Objectives

The gas turbines are popular because of the availability of various renewable and alternative fuels such as synthetic gas (composed of H_2 and CO) and synthetic natural gas (composed of H_2 and CH_4) as well as the conventional fuels such as natural gas and diesel fuel. Lean premixed gas turbine combustor has been known to be effective in minimizing pollutant exhaust gases such as NO_x , and is widely used in aviation and industrial energy production systems because they offer relatively high efficiency compared with diffusion burners [93]. However, premixed combustors may cause gas turbine components due to flash-back of flame and combustion instability, problems that have been studied by various research groups for last couple of decades. To date, computational and analytic solutions have been preferred to experimental studies to reduce development cost and time for gas turbine combustor, but highly reliable experimental data are required for numerical design tools to produce accurate values of design parameters. Combustion instability using hydrogen and methane fuel has been the subject of many fundamental studies on substitute natural gas power plants [2, 47-50]. In non-premixed turbulent combustion of methane with a small amount of hydrogen, increase in the ambient pressure increases the temperature of the flame and NO_x emissions, whereas the radial distribution of the temperature and mean mixture fraction decrease with increase in pressure [98]. Hydrogen-enriched methane flame can be utilized in mild combustion due to the stability of the flame [99].

The mechanism of combustion instability, which is known to be sustained by the coupling of acoustics of a system and heat-release fluctuations in the combustion field, is not fully understood [100]. Various parametric studies have been conducted using high-

speed laser diagnostics and other techniques to identify the cause of combustion instability, and numerous experimental/numerical studies have attempted to predict the onset of combustion instability. However, there exist no prediction tools which can be used to predict the combustion instability of a gas turbine combustor. For the prediction of combustion instability in gas turbine combustor, the flame transfer function (FTF) as defined as the heat release response of a flame to the inlet velocity oscillations and/or equivalence ratio fluctuations is a critical information needed to model the self-excited combustion instability [101]. Recent studies on FTFs have led to new research methods based on a flame describing function (FDF) [11, 55, 56] and locally measured FTF [104], as well as conventional FTF [94]. Lacoste et al. investigated the acoustic response of M-shaped and V-shaped methane flames in an AC electric field using a loudspeaker [105]. The shape of the flame did not affect the dynamic response, and it was confirmed that the gain of the FTF with plasma forcing showed a larger response characteristic [59–62]. The FTF can be measured differently with respect to the confinement of the combustion chamber, and the flame deformation and acceleration of the fresh stream flow of reactant have been found to be dominant in the shape of the flame [97].

Lean direct injection (LDI) combustors are used to operate the gas turbine without a rich flame in the combustion zone by directly injecting fuel into combustor, thus reducing NO_x emissions by minimizing the flame temperature and reducing the thermal stress of the combustor by eliminating local hot spots [108]. Tacina et al. experimentally verified the emission characteristics of NO_x with respect to the shape of the center dome and the various recess configurations of the multi-injector in a swirl-Venturi LDI [10]. The velocity distribution and flame stabilization derived from large-eddy simulation (LES) experiments with a liquid-fueled LDI were compared with experimental data, and the size of the bubble caused by vortex breakdown was found to be reduced by the reverse flow in the combustion state [109]. The turbulent flow-field and the dynamic vortex structure generated in the combustion zone were compared in single- and nine-element LDI combustors, and the unsteadiness of the flame was investigated through computational analysis to facilitate the breakup of the droplet [102]. The heat release rate oscillation in

a liquid-fueled LDI combustor is affected by the instantaneous flow rate of the fuel, rather than the droplet size and distribution as well as by the change in the air flow rate [103].

An open-source combustion instability low-order simulator (OSCILOS) has been used to model the combustion instability, providing a useful tool for modeling gas turbine combustors with a very long combustor length compared to the flame length [110]. Studies on longitudinal industrial gas turbine combustors have produced effective predictions of the combustion instability mode at high pressures, and provide a consistent velocity amplitude and mode shape [111]. In a full-scale industrial gas turbine combustor with a high-pressure test cell, the modal frequency was found to be highly consistent with the experimental values for combustion conditions [106].

The objectives of this study are to characterize and predict the onset of the thermoacoustic instability for a lean direct-injection gas turbine combustor running on of hydrogen-enriched methane flames. The effect of fuel composition on combustion instability is parametrically studied and the occurrence of combustion instability is predicted using OSCILOS. Compared with the lean premixed combustors, relatively little research on the combustion instability in LDI gas turbine combustors has been reported. In case of premixed combustor, the measurement of the velocity perturbation at the inlet of the combustion zone as the input function of the flame transfer function is relatively straight forward. However, in LDI combustors, it can be very difficult to measure the fuel flow rate fluctuation at the inlet of combustor while the flame exists, making the direct measurement of the flame transfer function very difficult. Therefore, the flame transfer function is experimentally measured in two stages: the intermediate transfer function (ITF) and the fuel line transfer function (FLTF). The resulting flame transfer function is used as input to the thermoacoustic modeling of combustion instability.

5.2 Description of Experimental and Modeling Approach

5.2.1. Model Gas Turbine Combustor and Instrumentations

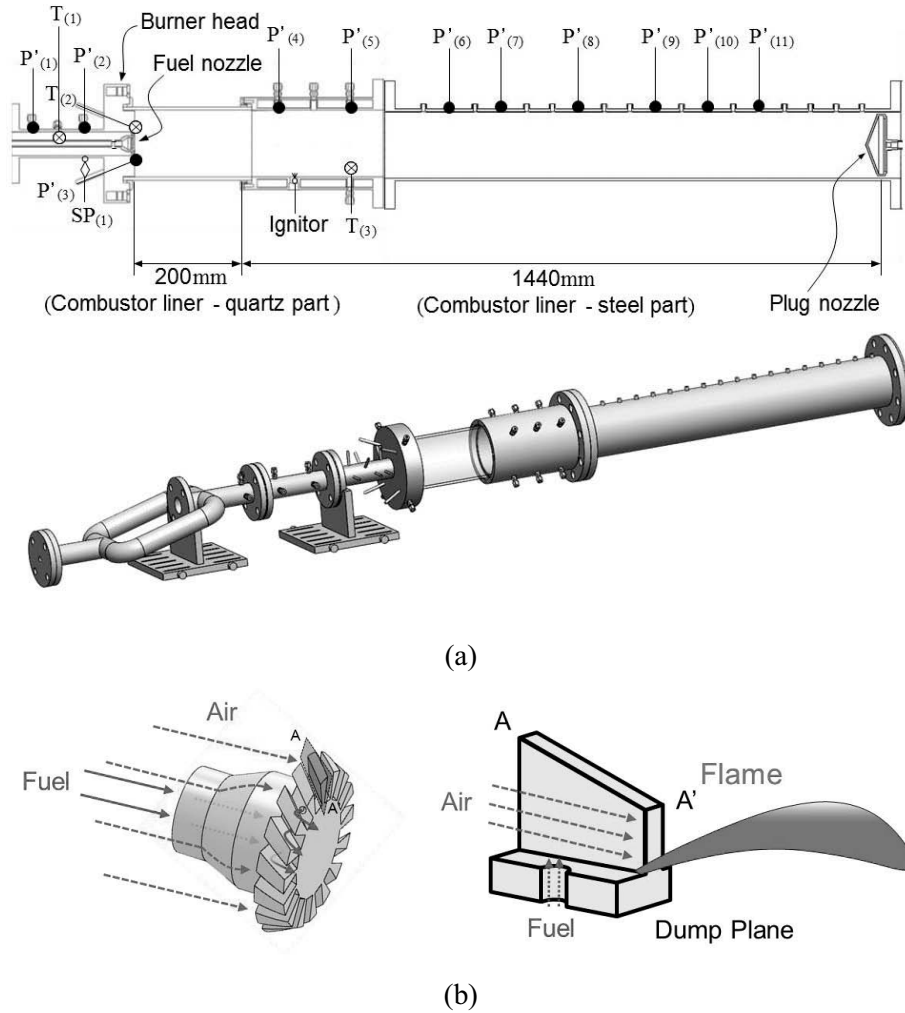


Fig. 5.1 (a) Schematic of model gas turbine combustor and sensor position and (b) lean direct injector (LDI).

A model gas turbine combustor with a direct injection type fuel injector as shown in Fig. 5.1 (a) is used for this study. A plug nozzle was installed to block 90% of the cross-

sectional area, thus forming an acoustically closed boundary that imitates the acoustic environment of the turbine blade in the gas turbine combustor. The length of combustor (from combustor dump plane to plug nozzle) is measured as 1440 mm and the optical access to the beginning section of combustor is provided by a 200 mm long quartz tube. A torch ignitor with H₂-air is installed at the rear end of the quartz tube for ignition. To prevent combustor liner damage during the combustion test, cooling water was supplied to combustor liner jacket. For the dynamic pressure measurement, infinite-length probes are used to prevent interference due to pressure reflection. The lean direct injector (LDI) with a 45° swirl vane is used in this research, and the fuel mixture and the air are supplied in the coaxial direction. The nozzle is designed to have a very large swirl number (Swirl number=0.83) to form a thin flame and to have a mixing length of 2.7 mm upstream of the dump plane of the fuel mixture (Fig. 5.1 (b)). The flame has a very short and thin structure compared to the length of the combustor, and the flame has a V-shape. A total of 11 dynamic pressure sensors (PCB 102A05) are installed before and after dump plane to measure dynamic pressure along the length of combustor. Typically, the pressure data are acquired for 1.0 sec at the data rate of 25,000 samples/sec. An R-type and two K-type thermocouples are installed at three locations to measure the inlet air temperature, combustor liner temperature and flame temperature. In addition, a static pressure sensor is installed in the air feeding line.

The heat release from overall flame is measured using a photomultiplier tube (PMT, Hamamatsu, H7732-10) equipped with an OH bandpass filter (307 ± 10 nm). Flame structure is characterized using OH-PLIF (Planar Laser Induced Fluorescence) using a laser system consisting of a high-speed (up to 7 k-Hz) Nd:YAG laser (Edgewave, IS-200L), a dye laser (Sirah, Credo-Dye-LG-24) and a wave extension system (VC-HS-IRO, 25mm, 10ns, LaVision) and an high-speed (up to 10 k-Hz) intensified charge-coupled (ICCD) camera (High-speed star 8; 1024×1024 pixels) and an intensifier (Highspeed IRO). A UV lens ($f/2.8$) and an OH bandpass filter (307 ± 10 nm) are mounted in the camera to collect emission only from OH radical.

5.2.2. Experimental Conditions

The experimental conditions used to determine the combustion instability characteristics and FTFs under various combustion conditions are listed in Table 5.1. Hydrogen-enriched (25, 50 and 75% by volumetric flow-rate) methane is used as fuel and the air is used as the oxidant. The flow rates of fuel and air are measured and controlled by mass flow-rate controllers (MFC) (for air: Bronkhorst, F-206BI, uncertainty = $\pm 0.8\%$; for fuel: Parker, Porter-200, uncertainty = $\pm 1.0\%$). The temperature of inlet air is set at $200 \pm 3^\circ\text{C}$ and its volume flow rate at 1100 slpm. The equivalence ratio is varied from 0.45 to 0.65.

Table 5.1. Experimental test conditions.

Parameter	Value
Experimental of thermo-acoustic instability	
Fuel	H ₂ , CH ₄
Air flow rate	1,100 slpm (0.18 kg/s),
Air temperature	200°C (= 473 K)
Heat load	40 kW
H ₂ ratio $[\frac{H_2}{H_2+CH_4}]$	25%, 50%, 75%
Equivalence ratio	0.45, 0.50, 0.55, 0.60, 0.65
Combustor length	1,440 mm
Transfer function	
Equivalence ratio	0.55
Combustor length	360 mm (H ₂ :CH ₄ = 25:75) 380 mm (H ₂ :CH ₄ = 50:50) 330 mm (H ₂ :CH ₄ = 75:25)
Fuel modulation frequency	0–600 Hz

5.2.3. Measurement of Flame Transfer Function (FTF)

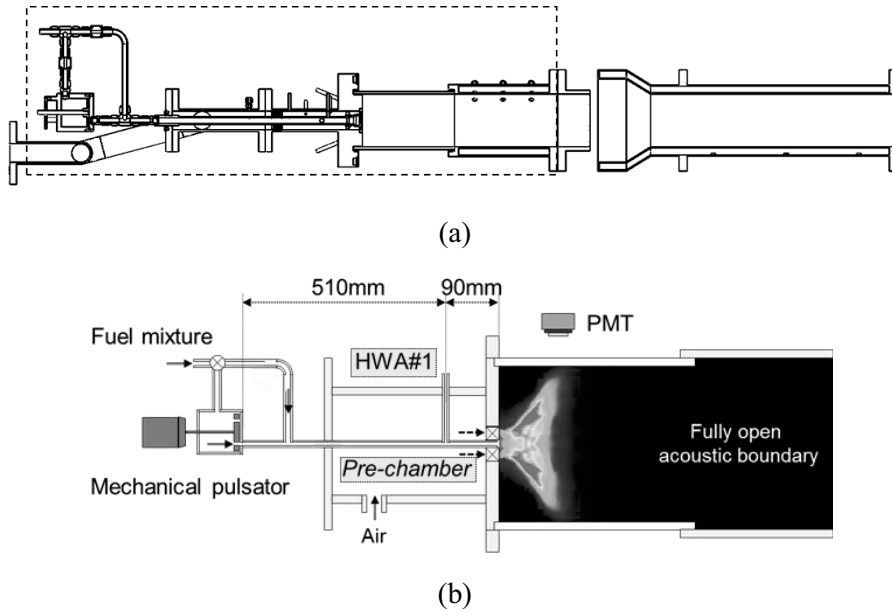


Fig. 5.2. Schematic of experimental setup for flame transfer function.
 (a) open boundary gas turbine combustor, (b) flame transfer function setup.

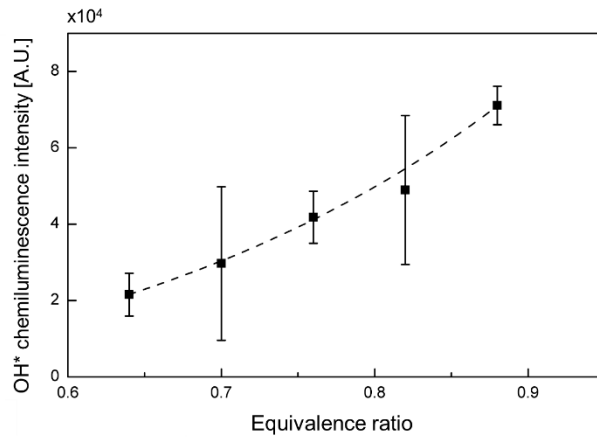


Fig. 5.3. OH* chemiluminescence intensity of the flame with respect to the equivalence ratio for direct injection.

Figure 5.2 shows the model combustor geometry for measuring the flame transfer function. The rear end of the combustor is open to form an acoustic open boundary, thus preventing the acoustic influence of the combustor from affecting FTF measurement. A mechanical pulsator (siren) is used for the modulation of fuel flow and a bypass line is installed to maintain nearly constant fuel flow rate fluctuation (10-12%). The details of the siren can be found in previous publication [51]. The modulation frequency is varied from 0–600 Hz in an increment of 25 Hz. The velocity perturbation (u') of fuel flow is measured by a hot-wire anemometer (HWA) and a photomultiplier tube (PMT) is used to measure the heat release rate (q'). The OH^* intensity of the flame according to the equivalence ratio (plotted in Fig. 5.3) was derived using the OH-PLIF images shown in Fig. 5.6, which demonstrates that the heat release of direct injection is exponential to the OH^* intensity.

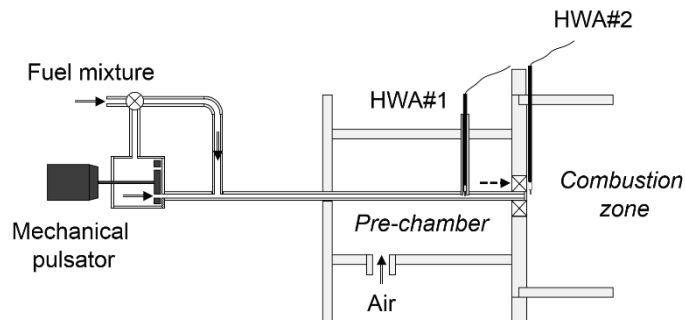
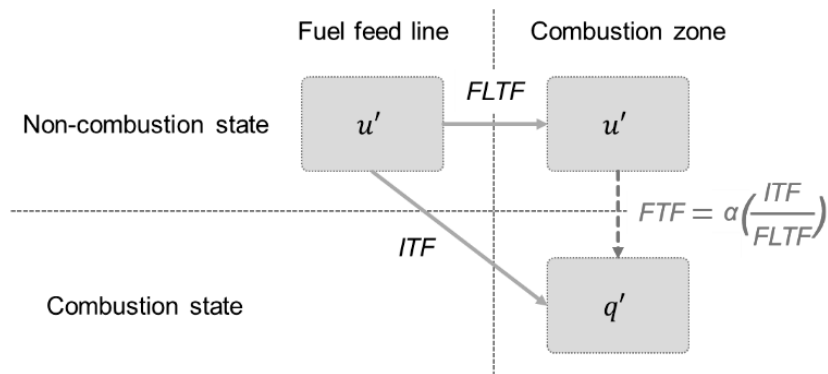
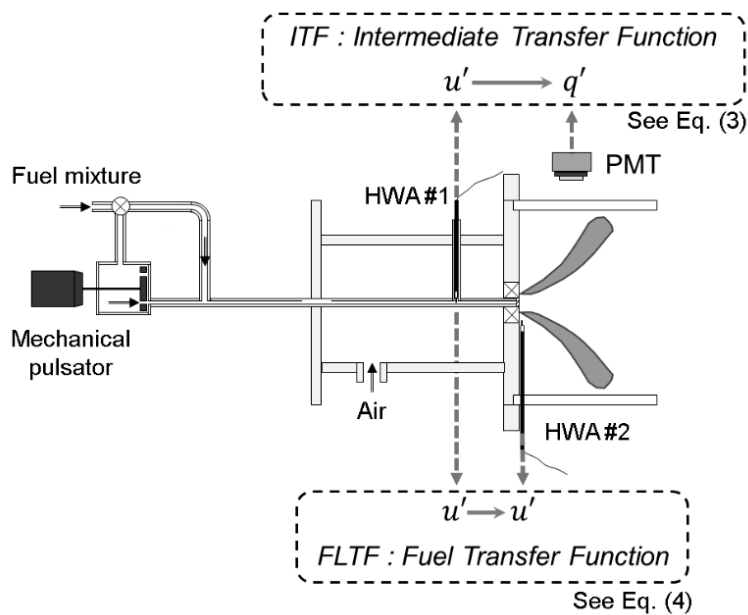


Fig. 5.4. Schematic of experimental setup for fuel transfer function (FLTF).



(a)



(b)

Fig. 5.5. (a) Block diagram and (b) input/output parameters of the relationship between ITF, FLTF and FTF.

The FTF is defined as in Eq. (5.1) where the input/output function of FTF is the velocity fluctuation of fuel flow at the inlet of combustor/the heat release fluctuation of whole flame, respectively.

$$FTF = \frac{q'/\bar{q}}{u'/\bar{u}} = f(n, \tau)_{FTF} = [ne^{i\omega\tau}]_{FTF} \quad (5.1)$$

where the input and output functions of the FTF are the fluctuation in fuel flow velocity at the inlet of the combustor and the heat release fluctuation of whole flame, respectively. Moreover, u'/\bar{u} is measured at the tip of the injector (HWA#2 in Fig. 5.4) and n (gain) and τ (phase delay) are input to the one-dimensional thermo-acoustic model. The block diagram in Fig. 5.5 summarizes how the FTF was determined. Due to the difficulty of measuring fuel flow velocity fluctuation at the tip of injector where the flame is held when it exists, the velocity fluctuation, measured at the injector pre-chamber (HWA#1 in Fig. 5.4), can be used as the input function. However, for an injector across which a relatively large pressure drop occurs, the velocity fluctuations before and after the injector tip cannot be assumed to be the same. Therefore, the response of injector tip to the modulated fuel flow and the FLTF, as defined in Eq. (5.3) below, can be characterized and used for this purpose.

The transfer function using the velocity perturbation in the pre-chamber is defined as the ITF, as in the method of obtaining the FTF in the premixed burner. The FLTF defines the gain and phase by identifying the dynamic response between velocity perturbations through the fuel feeding system caused by the siren in the non-combustion state. The input and output functions of the FLTF are the velocity of fuel flow at the inlet of combustor and the velocity of fuel flow ejected from the injector, respectively, as follows (Fig. 5.5(b)):

$$ITF = \frac{[q'/\bar{q}]_{PMT}}{[u'/\bar{u}]_{HWA\#1}} \Big|_{comb.} \quad (5.2)$$

$$FLTF = \frac{[u'/\bar{u}]_{HWA\#2}}{[u'/\bar{u}]_{HWA\#1}} \Big|_{non-comb.} \quad (5.3)$$

The FTF is defined as the dynamic flame response of the fuel mixture injected from the lean direct injector to the heat release of the flame in the combustion zone. For this purpose, the fluctuation of the fuel mixture velocity in the combustion zone must be measured.

However, it is difficult to measure velocity perturbations in the very high-temperature zone above 1,200 °C. To solve this problem, we propose a method to calculate the velocity fluctuation indirectly in the combustion zone using the ITF and FLTF to obtain the FTF.

The FTF is experimentally measured as the velocity perturbation of the fuel generated from the siren to the heat release fluctuation in the combustion chamber and is expressed as in Eq. (5.4).

$$FTF = \frac{[q'/\bar{q}]_{PMT}}{[u'/\bar{u}]_{HWA\#2}} \Big|_{comb.} \quad (5.4)$$

FTF can be obtained by combination of experimentally measured ITF, FLTF, and the density ratio in fuel feed line and combustion zone (see equation from (5.4) to (5.8)).

$$FTF = \left(\frac{[q'/\bar{q}]_{PMT}}{[u'/\bar{u}]_{HWA\#1}} \Big|_{comb.} \right) \cdot \left(\frac{[u'/\bar{u}]_{HWA\#1}}{[u'/\bar{u}]_{HWA\#2}} \Big|_{comb.} \right) \quad (5.5)$$

$$FTF = ITF \cdot \left(\frac{\Psi_1}{\Psi_2} \right) \left(\frac{[u'/\bar{u}]_{HWA\#1}|_{non-comb.}}{[u'/\bar{u}]_{HWA\#2}|_{non-comb.}} \right) \quad (5.6)$$

$$FTF = ITF \cdot \left(\frac{\Psi_1}{\Psi_2} \right) \frac{1}{FLTF} \quad (5.7)$$

$$FTF = \left(\frac{\Psi_1}{\Psi_2} \right) \frac{ITF}{FLTF} \quad (5.8)$$

Moreover, the relationship of velocity between in the combustion state and the non-combustion state is expressed in the following two equations as the density ratio at the location of HWA#1 and HWA#2.

$$[u'/\bar{u}]_{HWA\#1}|_{comb.} = \Psi_1 \cdot [u'/\bar{u}]_{HWA\#1}|_{non-comb.} \quad \text{where, } \Psi_1 = \left(\frac{\rho_{non-comb.}}{\rho_{comb.}} \right)_{feed\ line} \quad (5.9)$$

$$[u'/\bar{u}]_{HWA\#2}|_{comb.} = \Psi_2 \cdot [u'/\bar{u}]_{HWA\#2}|_{non-comb.} \quad \text{where, } \Psi_2 = \left(\frac{\rho_{non-comb.}}{\rho_{comb.}} \right)_{comb.\ zone} \quad (5.10)$$

The FTF obtained mathematically using ITF and FLTF can be represented as a block diagram as shown in Fig. 5.5(a). To calculate the density of each state and location, the temperature measures at T(1) and T(2) (see Fig. 5.1), where are installed in the feed line and the closest position to the flame, was used.

5.2.4. Combustion Instability Modeling

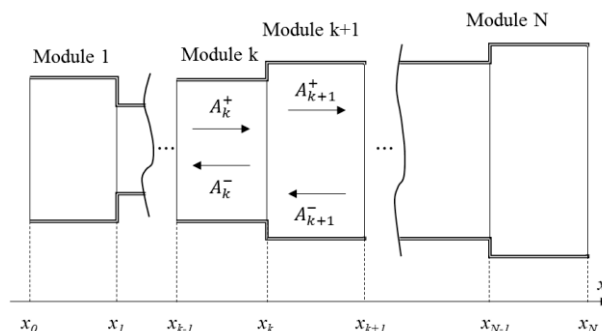


Fig. 5.6. Schematic of the acoustic multi elements for OSCILOS.

The OSCILOS solver is based on low-order network modeling. The thermos-acoustic system can be divided into the briefly constructed elements of each combustor, and each element satisfies the linear wave equation. In addition, an acoustic wave is formulated by the flame model at the point where the flame is located. Using this theory, the frequency at which the resonance mode occurs can be predicted and combustion instability is validated through the positive or negative value of the growth rate.

OSCILOS only models the combustion instabilities in the longitudinal mode; it excludes the transverse or tangential mode, and the flame is assumed to be a thin flame that is burned at a very short length. The combustor is represented by a network of connected modules, as shown in Figure 6, in OSCILOS. A heat source is generated between the inlet and outlet and the heat source separates the reactant and product gases. According to the linear wave equation, the fluid in each module is divided into a mean value and perturbation value. In addition, because the acoustic wave propagates backward or forward in the module, pressure,

velocity, and density in the k-module can be expressed as follows, considering an acoustic wave propagating on both sides:

$$p_k(x, t) = \bar{p}_k + p'_k(x, t) = \bar{p}_k + A_k^+(t - \tau_k^+) + A_k^-(t - \tau_k^-) \quad (5.11)$$

$$u_k(x, t) = \bar{u}_k + u'_k(x, t) = \bar{u}_k + \frac{1}{\bar{\rho}_k \bar{c}_k} (A_k^+(t - \tau_k^+) + A_k^-(t - \tau_k^-)) \quad (5.12)$$

$$\rho_k(x, t) = \bar{\rho}_k + \rho'_k(x, t) = \bar{\rho}_k + \frac{1}{c_k^2} (A_k^+(t - \tau_k^+) + A_k^-(t - \tau_k^-)) - \frac{1}{c_k^2} E_k(t - \tau_k^s) \quad (5.13)$$

Here, A_k^+ and A_k^- are the amplitudes of the acoustic wave in the downstream and upstream, respectively, E_k is the entropy wave amplitude, and the term related to τ is the time delay. Applying Eqs. (5.11) to (5.13) into each multi-module can calculate acoustic waves as a linear system, where the kth module can be expressed as the following global matrix:

$$\begin{bmatrix} \tilde{A}_N^+(s) \\ \tilde{A}_N^-(s) \\ E_N^+(s) \end{bmatrix} = \mathcal{G}_{1 \rightarrow N}(s) \begin{bmatrix} \tilde{A}_1^+(s) \\ \tilde{A}_1^-(s) \\ E_1^+(s) \end{bmatrix} \quad (5.14)$$

where $\tilde{\cdot}$ is the Laplace transform and $s = \sigma + i2\pi f$ indicates the Laplace variable, which can be expressed as growth rate and eigen frequency. The entropy wave disappears in the combustor outlet module. The reflection coefficients R1 and R2 are employed as acoustic boundaries at the inlet and outlet, respectively. The error of the outlet boundary in the last module can be expressed as follows, which expresses a contour map with growth rate and frequency.

$$\delta e(s) = \tilde{A}_N^-(s) - \tilde{R}_2(s) \tilde{A}_N^+(s) \exp(-\tau_N^+ s) \quad (5.15)$$

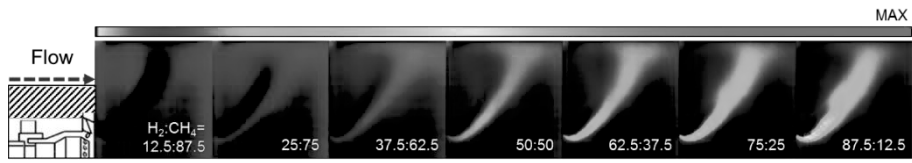
The eigen frequency is determined to be the minimized value of the frequency and growth rate errors at the outlet. OSCILOS requires input to the code, including the chamber dimension, the thermal properties of fluid (air), the flame model and the boundary conditions.

Details of these input parameters are described in section 5.3.3.

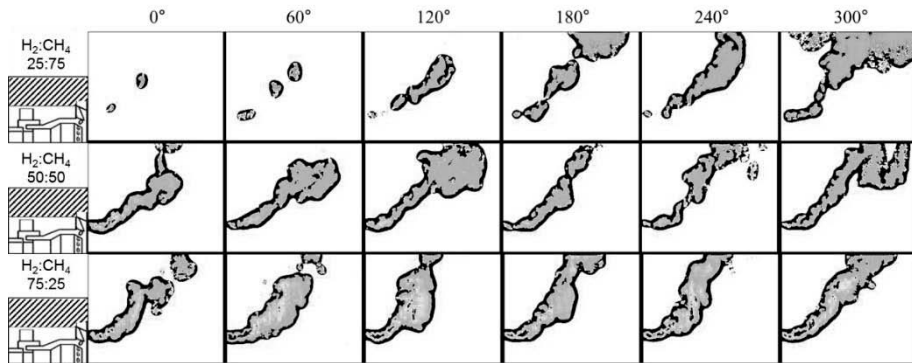
5.3 Results and Discussions

5.3.1. Characterization of Naturally Occurring Combustion Instability

Figure 5.7 (a) shows time-averaged (7000 images for 1 sec) OH-PLIF images at a fixed equivalence ratio of 0.55 as the hydrogen enrichment ratio (volumetric ratio of H_2/CH_4) changes. As the hydrogen enrichment ratio increases the flame length becomes shorter mainly due to the corresponding increase of flame speed. Also, it can be noted that the flame (as marked by the presence of OH radical) in the corner recirculation zone right downstream of dump plane gradually disappears as the H_2 content increases. The phase-locked instantaneous OH-PLIF images in Fig. 5.7 (b) suggests that how the heat release change during combustion instability depends on the hydrogen enrichment ratio: for the case of $H_2:CH_4=25:75$ the fluctuation level of heat release of flame is less than that of the case of $H_2:CH_4=75:25$ and the flame is observed to be disconnected for some phases but as the hydrogen enrichment ratio increases the flame is always anchored at the tip of fuel injector and the fluctuation level of heat release becomes less.



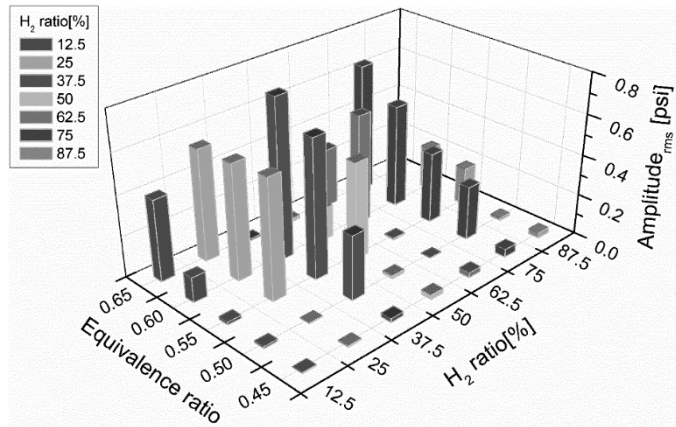
(a)



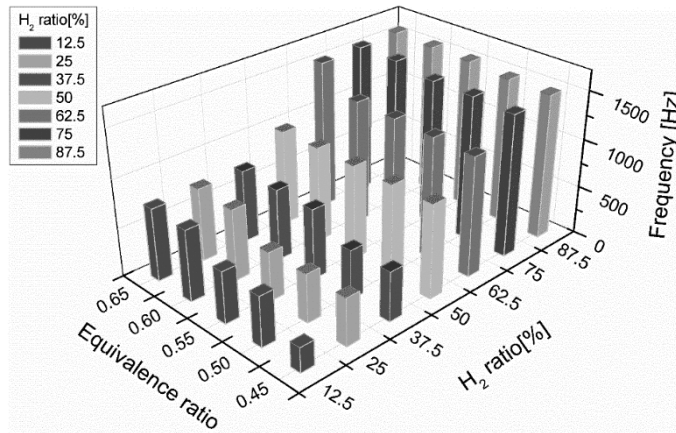
(b)

Fig. 5.7. Flame characteristics

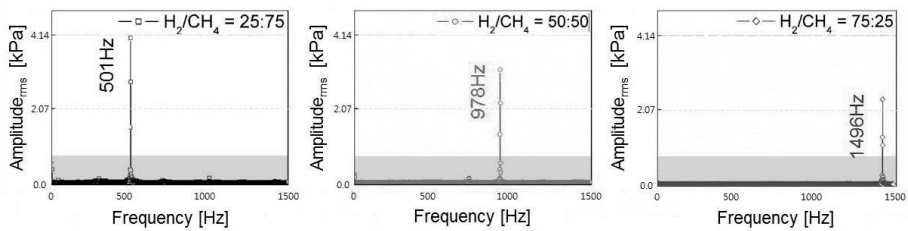
- (a) Time-averaged OH-PLIF images with respect to H_2/CH_4 composition (upper side),
 (b) Phase-locked instantaneous OH-PLIF images for H_2/CH_4 ratios of 25:75, 50:50, and 75:25.



(a)



(b)



(c)

Fig. 5.8. Combustion instability: (a) amplitude, (b) frequency with respect to various parametric conditions, and (c) pressure spectrum for H₂/CH₄ ratios of 25:75, 50:50, and 75:25.

The characteristics of naturally occurring combustion instability are presented in a form of stability map in Fig. 5.8 (a) where the peak-to-peak pressure oscillation levels measured at the dump plane ($P'_{(3)}$) location shown in Fig. 5.1 (a) are plotted as a function of equivalence ratio for various hydrogen enrichment ratios. The particular location is chosen for comparison of representative pressure oscillation level because the dump plane corresponds to pressure anti-node as the hydrogen enrichment ratio as well as equivalence ratio change. However, no general trend on how the amplitude of pressure oscillation changes with respect to the change of either the equivalence ratio or the hydrogen enrichment ratio is observed.

Figure 5.8(b) shows a plot of frequency at which the maximum instability occurs as the equivalence ratio and hydrogen enrichment ratio change. The instability frequency increases as the equivalence ratio or the H_2 -enrichment ratio increases, if the other parameter is fixed. This suggests that the instability frequency is closely related to the flame length: the shorter the flame length, the higher the combustion instability frequency. This is because the shorter the flame length the shorter the convective time delay from the injector to the flame, increased possibility to sustain combustion instability at higher frequency or higher mode. The fundamental mode of the longitudinal wave of the combustor is approximately 250 Hz for a 1440 mm combustor length and a given operating condition. Shown in Fig. 5.8 (c) are the FFT's of pressure measured at the dump plane for a fixed equivalence ratio of 0.55. As the hydrogen ratio increases, the combustion instability mode changes to higher modes, such as 501 Hz, 978 Hz, and 1496 Hz, etc.

5.3.2. Flame Transfer Function (FTF)

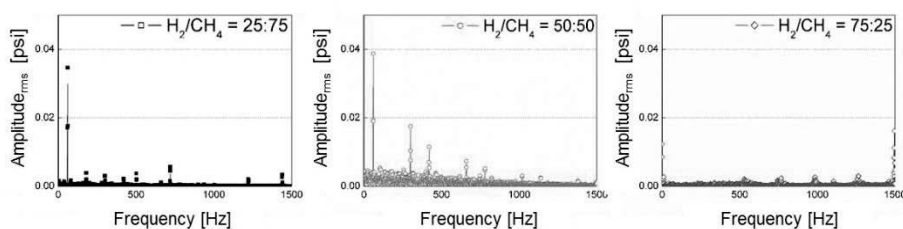


Fig. 5.9. Combustion instability amplitude in acoustically open boundary.

FTF measurements are made for the hydrogen enrichment ratios of 25:75, 50:50, and 75:25 at the flow condition (fuel/air flow rate) where the combustion is observed unstable and whose FFT's of pressure oscillations is shown in Fig. 5.8 (c). In order to minimize the effect of the resonance acoustics on the flame response, the length of combustor is shortened and the combustor exit is kept open. Figure 5.9 shows the combustor pressure spectra, indicating that the maximum amplitude of the resonant pressure fluctuation is less than 0.04 psi (~270 Pa) which is about 0.3% of the mean combustor pressure.

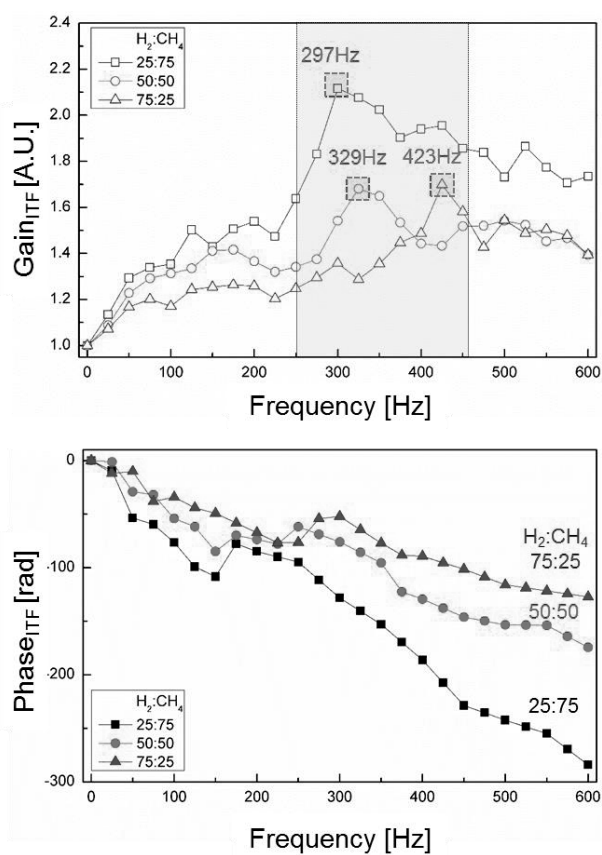


Fig. 5.10. Gain and phase of intermediate transfer function (ITF) with respect to the H₂/CH₄ composition.

As described in section 5.2.3, the fuel transfer function (FLTF) and the intermediate transfer function (ITF) should be measured to determine the flame transfer function (FTF). Figure 5.10 shows the plots of gain (Gain_{ITF}) and phase (Phase_{ITF}) of the intermediate transfer function (ITF). The Gain_{ITF} is always greater than 1.0 and the maximum gain value decreases as the content of hydrogen increases, indicating the higher the hydrogen content the less response of flame to fuel flow fluctuation. Also, the frequency at which the maximum gain is achieved increases as the content of hydrogen increases. The absolute value of the slope of phase plot ($\text{Slope}_{\text{Phase-ITF}}$) decreases as the content of hydrogen increases, suggesting the convection time delay (τ_{ITF}) between the HWA#1 location in Fig. 5.5 (b) where the fuel velocity is measured and the flame front decreases as the hydrogen content increases (hence the flame length is shortened). This is because the convection time delay (τ_{ITF}) between the HWA#1 location in Fig. 5.5 (b) where the fuel velocity is measured and the flame front is related to $\text{Slope}_{\text{Phase-ITF}}$ as follows.

$$\tau_{ITF} = -\frac{\text{Slope}_{\text{Phase-ITF}}}{2\pi} \quad (5.16)$$

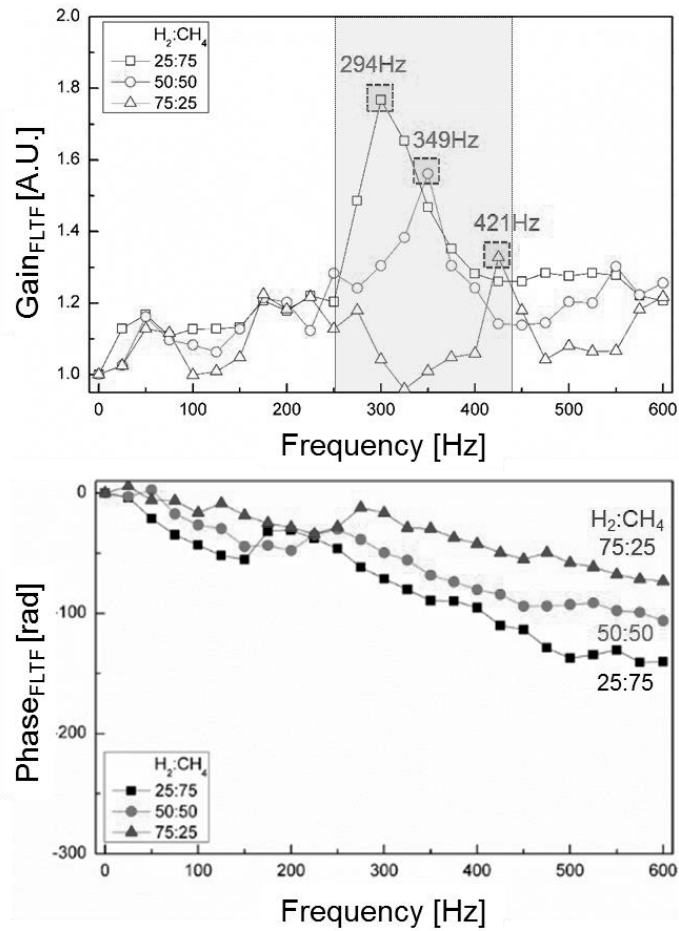


Fig. 5.11. Gain and phase of fuel transfer function (FLTF) with respect to the H₂/CH₄ composition.

Figure 5.11 shows the plots of gain (Gain_{FLTF}) and phase (Phase_{FLTF}) of the fuel transfer function (FLTF) for a fuel injector with the feedline length of 600 mm. Similar to the ITF, the Gain_{FLTF} is always greater than 1.0 and the maximum gain value decreases as the content of hydrogen increases. Also, the frequency where the maximum gain is achieved increases as the content of hydrogen increases and coincides nearly with that of gain_{FLTF}, indicating the gain_{FLTF} is affected by the acoustics of fuel feedline as will be discussed later. The absolute value of the slope of phase plot (Slope_{Phase-FLTF}) decreases as the content of

hydrogen increases, meaning the convection time delay between the HWA#1 in the fuel feedline and HWA#2 at the exit of injector (in Fig. 5.4) decreases as the hydrogen content increases. This is because the total fuel flow rate for fixed equivalence ratio increases as the hydrogen content in fuel mixture increases.

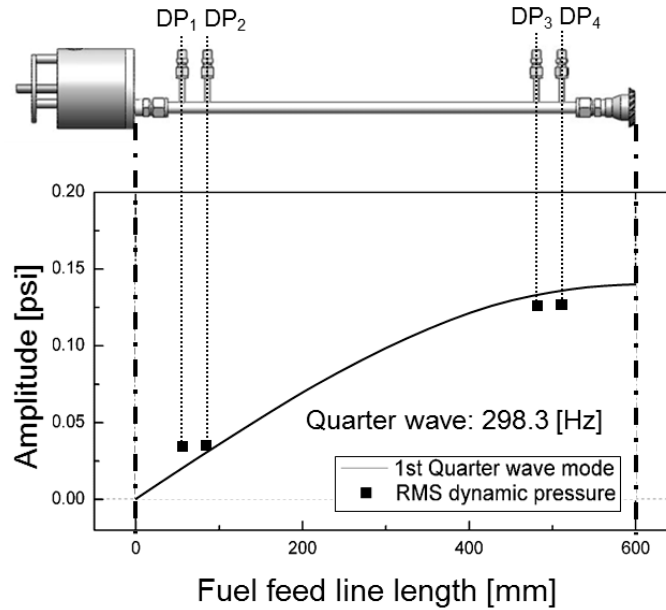


Fig. 5.12. Schematic of the fuel feedline and siren (top) and pressure wave mode shape (bottom).

Table 5.2. Comparison between calculated quarter wave frequency and measured frequency of peak gain_{FLTF} at 600 mm fuel feedline.

H ₂ :CH ₄	Calculated	Measured	Error
25:75	278.3 Hz	294 Hz	5.3%
50:50	348.5 Hz	349 Hz	0.1%
75:25	418.7 Hz	421 Hz	0.5%

To examine the acoustic characteristics of the fuel feedline, two pairs of dynamic pressure sensors are mounted at the exit of siren and injector, as shown in Fig. 5.12. The measurement results for the fuel feedline length of 600 mm are summarized in Table 2. For hydrogen enrichment ratios of 25:75, 50:50, and 75:25, standing waves at 294, 349, and 421 Hz are formed, respectively. These frequencies correspond to the quarter wave resonance frequencies of the fuel feedline and are calculated as follows.

$$\text{Quarter wave frequency} = \frac{c_{fuel}}{4 \cdot (L_{fuel\ feed\ line})} \quad \dots (5.17)$$

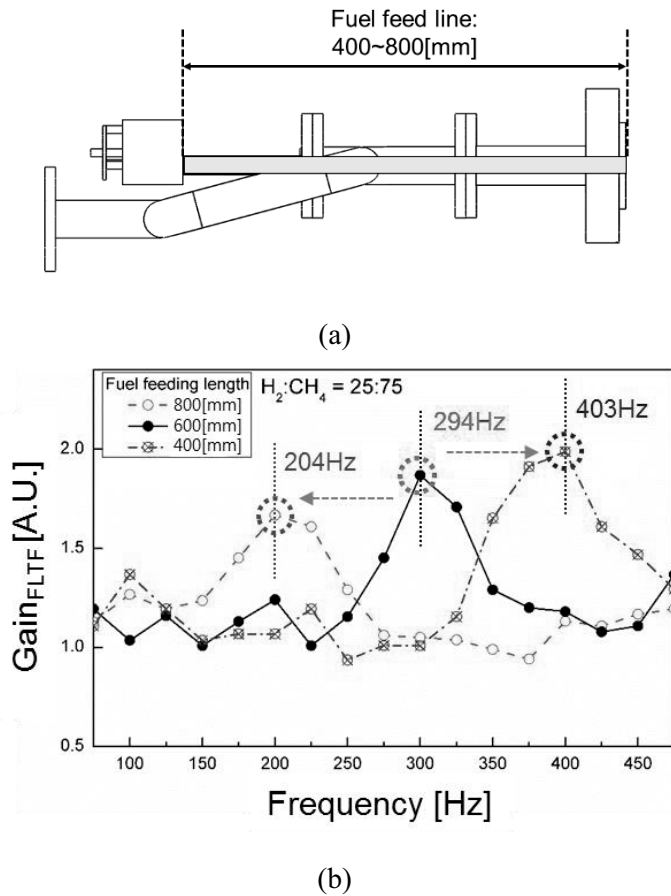


Fig. 5.13. (a) Schematic of FLTF measurement setup and fuel feeding line and (b) the effect of feeding-line length on FLTF gain.

Additional FLTF measurements are made for fuel feedline lengths of 400 mm and 800 mm for the hydrogen enrichment ratio of 25:75. As shown in Fig. 5.13(b), the maximum gain_{FLTF} occurs at certain frequencies for injectors with different feedline lengths. Table 5.3 shows that those frequencies coincide exactly with the calculated quarter-wave resonance frequency for each injector, confirming the acoustics of the fuel feedline play a role in the gain of the ITF and FLTF.

Table 5.3. Comparison between measured and calculated quarter wave frequency with respect to the fuel feedline at $H_2:CH_4=25:75$.

Feed line [mm]	Calculated	Measured	Error
400	417.5 Hz	403 Hz	3.5 %
600	278.3 Hz	294 Hz	5.3 %
800	208.8 Hz	204 Hz	2.3 %

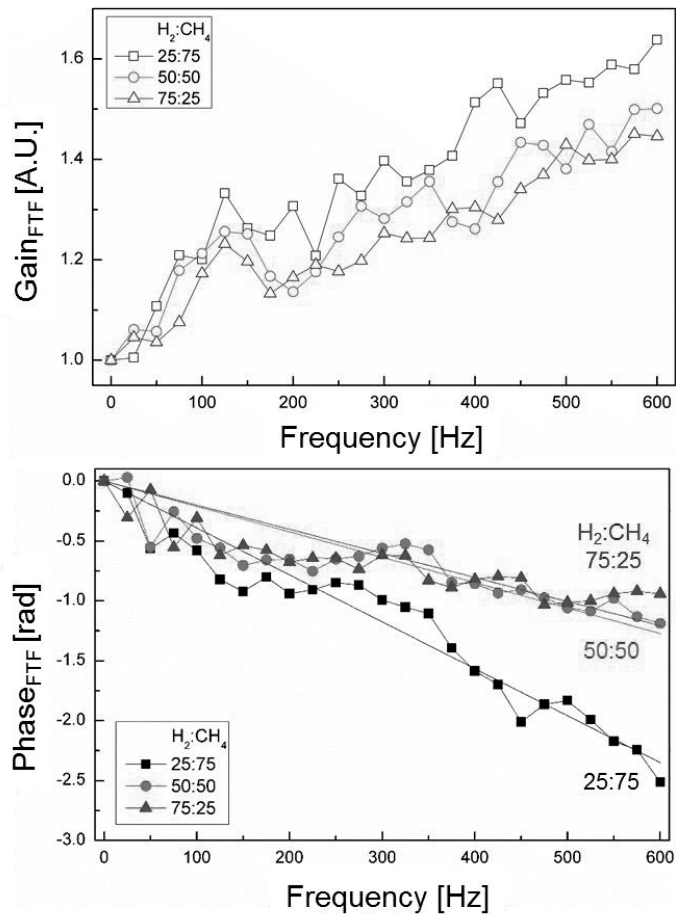


Fig. 5.14. Gain and phase of FTF with respect to the H_2/CH_4 composition.

Table 5.4. Density ratio in the fuel feedline and combustion zone with respect to the fuel composition.

H ₂ /CH ₄	25:75	50:50	75:25
Ψ_1 / Ψ_2	0.72	0.721	0.724

To obtain the FTF considering the velocity fluctuation in the combustion zone and excluding the acoustic effect in the pre-chamber, ITF and FLTF were used to indirectly calculate the velocity in the combustion zone. The density ratio (see Table 5.4) at each location is measured and $gain_{FTF}$ and $phase_{FTF}$ are derived from the equations in Section 5.2.3. Figure 5.14 shows plots of $Gain_{FTF}$ and $Phase_{FTF}$ of the FTF calculated by Eq. (5.8) using the predetermined ITF and the FLTF. $Gain_{FTF}$ gradually increases as the frequency increases, and, for a fixed frequency, a higher hydrogen enrichment ratio flame results in a lower gain. As the hydrogen enrichment ratio increases, the slope of the phase plot decreases because it is related to the convection time delay (τ_{FTF}) as follows:

$$\tau_{FTF} = -\frac{Slope_{Phase-FTF}}{2\pi} \quad \dots (5.18)$$

Table 5.5. Phase slope gradient and time delay of FTF with respect to fuel composition.

H ₂ :CH ₄	Slope [rad·s]	Time delay [ms]
25:75	1.07×10^{-3}	0.170
50:50	8.48×10^{-4}	0.135
75:25	7.00×10^{-4}	0.111

This means the convection time delay between the exit of the injector and the flame location decreases as the enrichment ratio increases. Table 5.5 shows the time delay obtained using the slope of $phase_{FTF}$ for the hydrogen enrichment ratios of 25:75, 50:50,

and 75:25, as calculated by Eq. (5.18). However, there is not much difference in the convection time delay between the hydrogen enrichment ratio of 50:50 and 75:25 mainly because the flame length does not change as much when the hydrogen enrichment ratio increases from 50:50 to 75:25.

5.3.3. Modeling of Thermo-acoustic Instability

To model the combustion instability using OSCILOS, four groups of parameters (i.e. Chamber dimensions and flame location, Thermal properties, Flame model and Boundary conditions) are required as the input to OSCILOS.

- Chamber dimensions and flame location

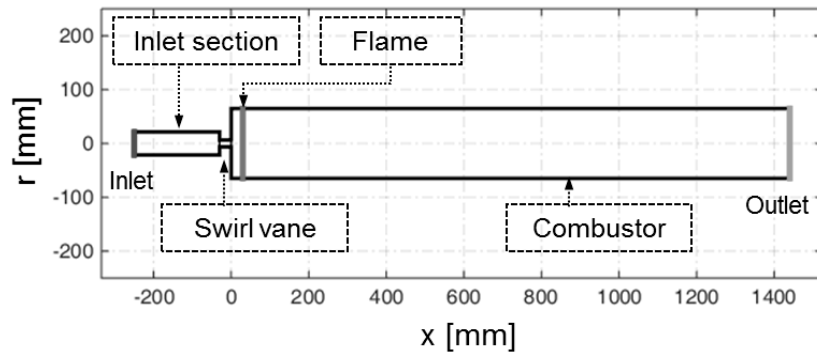


Fig. 5.15. Simplified combustor dimension in OSCILOS.

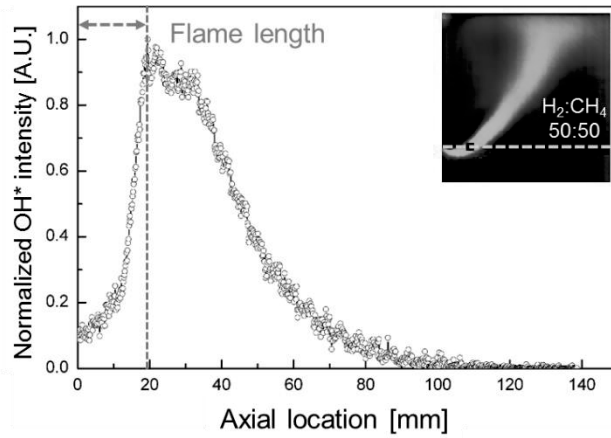
The model gas turbine combustor used in this study is simplified as consisting of inlet section, swirl vanes, flame and combustor section as shown in Fig. 5.15. The equivalent area of swirl vanes is determined by measuring air flow rate and the corresponding pressure drop across swirl vanes as follows [112].

$$A_{equivalent} = \frac{\rho \dot{V}}{\sqrt{2\rho\Delta p}} \quad \dots (5.19)$$

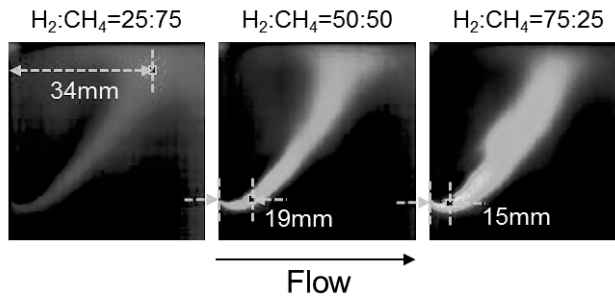
As the length of the flame is relatively short compared to the total length of the combustor, the flame is assumed as a thin flame at an axial location where the normalized OH-PLIF intensity as defined in the following becomes maximum.

$$I_{axial}(x) = \int_{-R}^R I(r, x) dr / I_{max} \quad \dots (5.20)$$

where I_{max} represents the maximum OH-PLIF intensity in an averaged OH-PLIF image. Figure 5.16(a) shows a typical distribution of $I_{axial}(x)$ and the location of its maximum. As shown in Fig. 5.16(b), the location of the flame was measured to be 34 mm, 19 mm, and 15 mm for flames with hydrogen enrichment ratios at hydrogen/methane ratios of 25:75, 50:50, and 75:25, respectively.



(a)



(b)

Fig. 5.16. (a) Axial heat release of the OH-intensity distribution and (b) Flame length with respect to the H₂/CH₄ composition.

- Thermal properties

Table 5.6 lists thermal properties used as input to the OSCILOS. The chamber pressure is set at 1.02 atm (103,351 Pa) since the static pressure is measured between 1.01 atm and 1.03 atm as the hydrogen enrichment ratio changes. The inlet air is set at 200°C (473 K). The mean velocity is calculated by the OSCILOS with the input of mass flow rate of air. The heat release rate of the methane fuel is set to be 40 kW based on the heating value of methane and the equivalence ratio.

Table 5.6. Inlet thermal properties for longitudinal mode in OSCILOS.

Parameter	Value
Pressure	1.02atm (103,351 Pa)
Temperature	200°C (= 473 K)
Mean velocity	4.64 m/s (H ₂ :CH ₄ =25:75) 5.84 m/s (H ₂ :CH ₄ =50:50) 8.08 m/s (H ₂ :CH ₄ =75:25)
Specific heat capacity ratio	Change with temperature
Heat release rate	40kW
Combustion efficiency	1.0
Temperature ratio across the flame	3.81

- Flame model

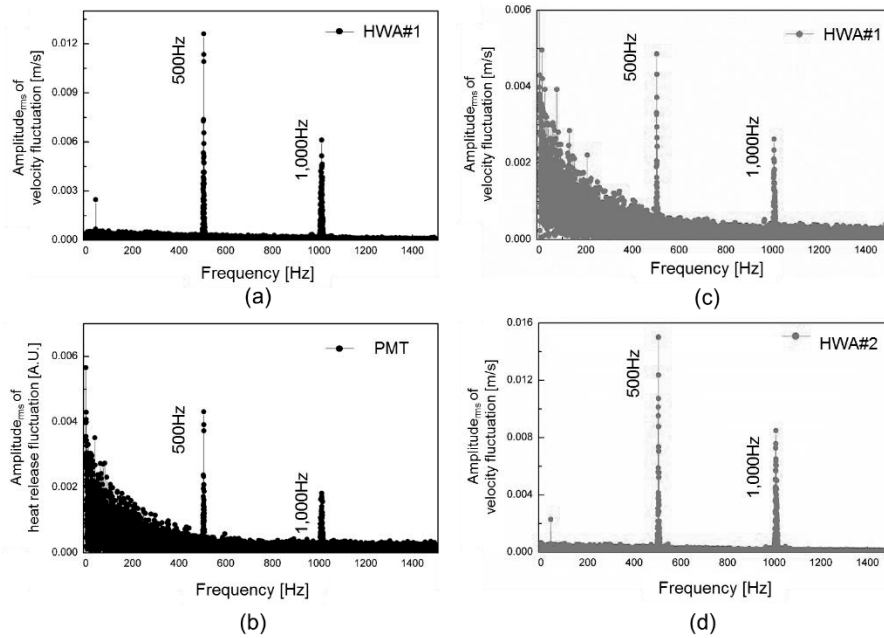


Fig. 5.17. FFT result of raw data by location in high modulation frequency modes using higher harmonic responses of ITF and FLTF at $H_2:CH_4 = 25:75$, 500 Hz fuel modulation:

- (a) velocity fluctuation of ITF measured at HWA#1,
- (b) OH-chemiluminescence fluctuation of ITF measured at PMT,
- (c) velocity fluctuation of FLTF measured at HWA#2, and
- (d) velocity fluctuation of FLTF measured at HWA#2.

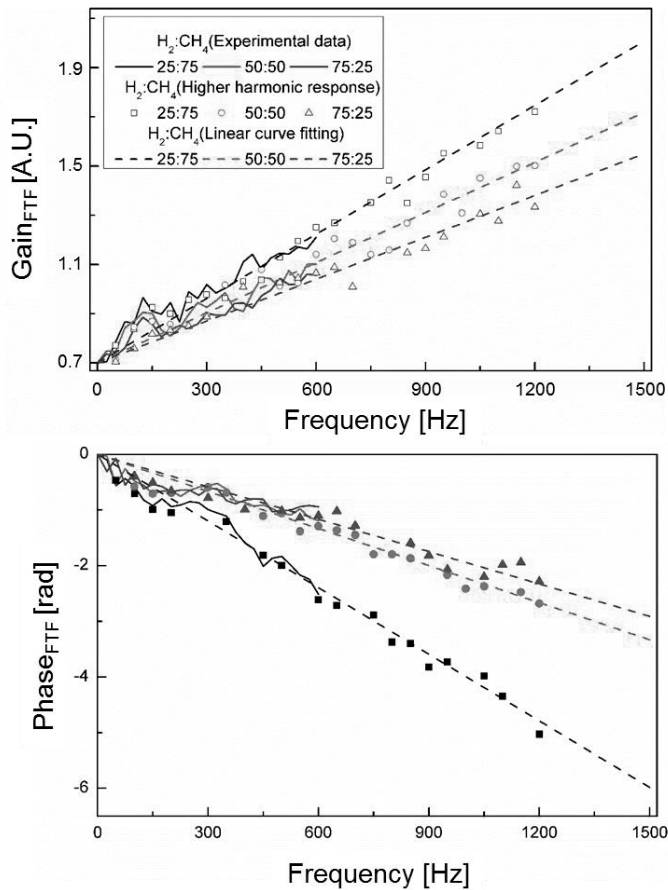


Fig. 5.18. Gain_{FTF} and phase_{FTF} from experimental data (line), higher harmonic response in fuel modulation (dotted line), and linear curve fitting (dashed line).

Figure 5.17 shows the of the velocity perturbation of the fuel in HWA#1. The amplitude of the FFT is high at 500 Hz, which is the same as the rotation of the motor at 500 Hz modulation. Another peak occurs at its harmonics of 1,000 Hz and 1,500 Hz. This is due to the higher harmonic response of the mechanical pulsator (or speaker pulsator), and non-monotonic acoustic characteristics. The response characteristics of the flame due to the modulation of the fuel are obtained by measuring the OH-chemiluminescence using PMT, and peaks at 500 Hz, 1,000 Hz, and 1,500 Hz as the FFT value were obtained from the hot

wire. The ITF obtains the gain and phase for each frequency using the pressure and OH-chemiluminescence oscillation at the peak frequency of the ITF results. In other words, using the velocity and OH-chemiluminescence oscillation of the fuel modulation from 0 Hz to 600 Hz, the FTF up to its harmonic at 1,800 Hz can be mathematically calculated for the 3rd harmonic response. However, in the case of a higher harmonic response, verification is necessary because it has an amplitude that is smaller than the amplitude of the excitation frequency. FLTF is calculated using the higher harmonic response to velocity perturbations in HWA#1 and HWA#2. Figure 5.18 shows the plot of $gain_{FTF}$ and $phase_{FTF}$ of FTF for frequencies up to 1,200 Hz with data points obtained from the flame response at higher harmonic frequencies. Here, the data are linearly fitted from 0 Hz to 1,500 Hz.

- Boundary conditions

The longitudinal instability frequency of the standing wave formed inside the combustor was confirmed through frequency mode analysis. The fundamental mode was calculated to be about 250 Hz, and the combustion instability frequencies of the 2nd (501 Hz), 4th (978 Hz), and 6th (1,496 Hz) modes were measured according to H_2/CH_4 ratio. Because these longitudinal waves should be acoustically closed at both ends, the dump plane and the plug nozzle are modeled as acoustically closed ends.

- Prediction of Instability

Table 5.7 shows the growth rate vs. eigen frequency for flames with the hydrogen enrichment ratios of 25:75, 50:50, and 75:25 at a fixed equivalence ratio of 0.55. For the hydrogen enrichment ratio of 25:75, the most unstable combustion will occur at around 514 Hz. As the hydrogen enrichment ratio increases, the frequency at which unstable combustion occurs is shifted to higher frequencies: 1,013 Hz and 1,478 Hz for the hydrogen enrichment ratios of 50:50 and 75:25, respectively. These results are consistent with the experimental observations in Fig. 5.8(c), and the predicted instability frequencies are within 3.6% of the measured ones (listed in Table 5.8). Figure 5.19 shows the predicted acoustic mode shapes overlaid with measured RMS dynamic pressure along the combustor

length for each condition. The predicted acoustic modes agree very well with the measured acoustic modes. In addition, the results clearly show that the instability occurring at higher hydrogen enrichment ratios corresponds to higher harmonics of the 1L mode (based on combustor length), which is the fundamental mode instability occurring at the hydrogen enrichment ratio of 25:75.

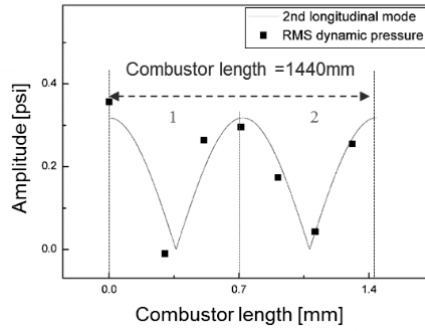
Table 5.7. Estimation results (Eigen frequency and growth rate) of OSCILOS with respect to the H₂:CH₄ ratio using FTF.

H ₂ :CH ₄					
25:75		50:50		75:25	
Frequency [Hz]	Growth rate [rad/s]	Frequency [Hz]	Growth rate [rad/s]	Frequency [Hz]	Growth rate [rad/s]
243.5648	-122.356	267.127	-1.6378	212.5646	-135.1561
311.6543	-85.945	374.3648	34.32	394.1564	6.1864
511.3564	51.331	479.9823	-164.9721	488.156	-56.4984
754.231	-106.1854	712.7364	13.8415	701.1654	-0.6496
1,022.8546	12.4435	922.8101	97.1845	964.0246	12.4464
1297.897	-56.654	1212.6497	-41.5498	1,134.0564	-11.1564
1497.44	-1.0356	1,453.6489	-5.8612	1,493.2011	78.1564

Table 5.8. Comparison between FTF combustion instability frequency prediction and experimental instability frequency.

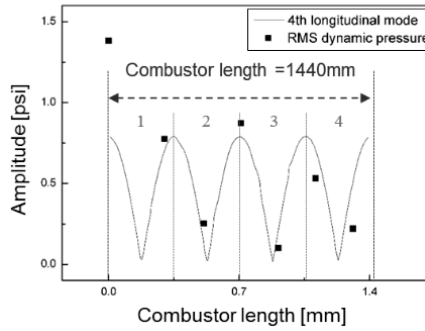
H ₂ :CH ₄	Eigen frequency (FTF)	Experimental instability frequency	Error
25:75	511.3 Hz	501 Hz	2.0%
50:50	992.8 Hz	978 Hz	1.5%
75:25	1493.2 Hz	1496 Hz	0.1%

- Instability frequency= 501Hz



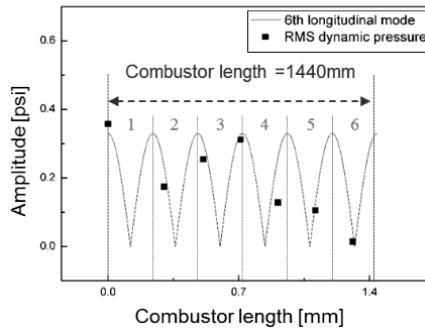
(a)

- Instability frequency= 978Hz



(b)

- Instability frequency= 1496Hz



(c)

Fig. 5.19. Comparison of experimental results and prediction of pressure mode shape.

(a) $H_2:CH_4 = 25:75$, (b) $H_2:CH_4 = 50:50$, and (c) $H_2:CH_4 = 75:25$.

- Combustion instability prediction by using ITF

Geometry and thermal properties of OSCIOS input setting are the same with conditions in the text. Intermediate transfer function (ITF) is defined as flame dynamic response with velocity fluctuation in the pre-chamber. This transfer function is a measurement method that has been conventionally used in the past. Table 5.9 compares the predicted combustion instability frequencies from the experimentally obtained instability frequencies. The predicted instability frequency using conventionally measured ITF underestimates the actual combustion instability frequency. This means that the phaseITF calculates a longer time delay than that of the FTF.

Table 5.9. Estimation results (Eigen frequency and growth rate) of OSCIOS with respect to the H₂:CH₄ ratio using ITF.

H ₂ :CH ₄					
25:75		50:50		75:25	
Frequency [Hz]	Growth rate [rad/s]	Frequency [Hz]	Growth rate [rad/s]	Frequency [Hz]	Growth rate [rad/s]
202.464	-82.554	228.137	-49.5528	240.853	-15.5482
485.73	74.661	480.995	-114.658	498.423	-68.096
666.355	0.7734	700.344	-106.884	720.957	-89.476
899.296	-45.6677	918.033	54.374	938.238	-56.8438
1,048.02	-46.3178	1,048.34	2.59266	1,047.47	30.812
1,200.81	-9.07045	1,228.53	-102.995	1,197.88	-15.5444
1,422.41	-15.2356	1475.33	-95.2498	1456.08	-21.9158

Table 5.10. Comparison between ITF combustion instability frequency prediction and experimental instability frequency.

H ₂ :CH ₄	Eigenvalue frequency (ITF)	Experimental instability frequency	Error
25:75	485.7 Hz	501 Hz	3.1 %
50:50	908.0 Hz	978 Hz	7.2 %
75:25	1047.5 Hz	1496 Hz	30.0 %

5.4 Flame Structure in Flame Transfer Function

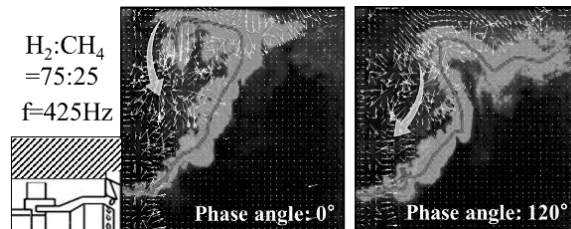


Fig. 5.20. Phase-locked instantaneous velocity field mapped with OH-PLIF images.

To identify the cause of instantaneous reverse flame and sinusoidal flames at the 425Hz modulation, PIV was conducted to determine the velocity field. The sinusoidal flame center line was formulated in the shear layer of the velocity field, as depicted in Fig. 5.20. In the reverse flame at phase angle 0° , the flame tip directed into the dump plane near the quartz tube because the velocity field was headed toward the dump plane in front of the flame center. Moreover, at 120° , the center of the sinusoidal flame tended to move back-and-forth for the tip repeatedly. The flame was winkled in an S-shape by the interaction of these two velocity fields. The flame winking and stretching phenomenon occurred repeatedly in 425Hz fuel modulation.

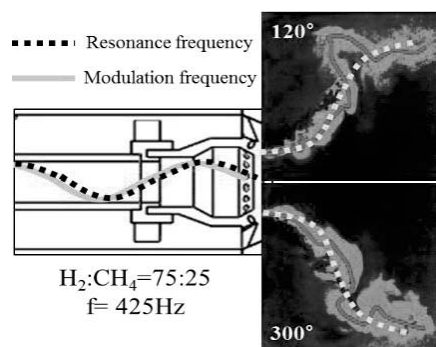


Figure 5.21. Schematic of attribution for fluctuated flame structure.

The strong acoustic fluctuation due to in-phase between resonance frequency and modulation frequency in the fuel feeding line generated the S-type flame at 425Hz modulation. The velocity fluctuation of the fuel with standing wave converted to the heat release fluctuation in a sinusoidal shape, as shown in Fig. 5.21.

In this study, combustion dynamic characteristics and flame response to fuel flow modulation of hydrogen and methane flames combustor were experimentally investigated in a model lean direct injection gas turbine. For this purpose, the fuel transfer function (FLTF) and intermediate transfer function (ITF) was proposed and measured for the hydrogen enrichment ratios of 25:75, 50:50, and 75:25. In addition, flame transfer function was measured using ITF to FLTF, which eliminates the effects of acoustic characteristics in fuel feed line. The gain of the FTF in the LDI gas turbine combustor is proportional to the excitation frequency regardless of the composition of the fuel. The combustion instability frequency according to the H₂/CH₄ ratio was predicted using OSCILOS and the mathematically derived FTF was verified through comparisons with the combustion instability frequency obtained from the experiments. A summary of the results is as follows:

1. Combustion experiments for H₂/CH₄ compositions and equivalence ratios were performed to investigate the combustion instability characteristics, and the flame length was used to confirm that the convection time delay affects the combustion instability to higher longitudinal modes. The FTF was measured to confirm that the gain and phase had different characteristics in the hydrogen flame. The FTF reflects the dynamic response characteristics of the fuel velocity fluctuation to the flame heat release fluctuation. However, in the case of LDI combustors or non-premixed combustor, where there are pressure drop at the injector or resonance frequency in the fuel feed line, the velocity in the fuel feed line cannot use in FTF. Therefore, the FTF was mathematically defined using ITF and FLTF to calculate the velocity in the combustion zone.
2. To understand the cause of the constructive characteristics in ITF, the acoustic

characteristics of the fuel injector were investigated. The peak frequencies of ITF and FLTF were determined by the quarter wave resonance in the fuel feed line. In order to examine the acoustic characteristics of the fuel feedline, dynamic pressure sensors are mounted at the exit of siren and injector and the resonance effect was validated by measuring the FLTF for various fuel feeding line lengths.

3. The combustion instability frequency was estimated from FTF results using the 1-D acoustic solver OSCILOS. The length of the flame and the effective fuel injection area were experimentally calculated, and the flame length was confirmed to be a very important parameter for frequency mode predictions. Gain_{FTF} and $\text{phase}_{\text{FTF}}$ for frequency from 600Hz to 1,200 Hz with data points obtained from flame response at higher harmonic frequencies. Furthermore, the combustion instability frequency was found to be well estimated when using gain_{FTF} and $\text{phase}_{\text{FTF}}$, which are corrected with ITF and FLTF. The predicted pressure mode shape in the combustor geometry are confirmed to be highly accurate with experimentally measured results.

FLTF was defined to calculate FTF in LDI combustor which cannot obtain the direct FTF because it is difficult to measure the velocity perturbation in the combustion zone. In addition, ITF, which is a conventional measurement method measuring the velocity perturbation in the pre-chamber, was measured. As a result, FTF, which can offset the resonance frequency generated in the fuel feed line and indirectly calculate the velocity perturbation in the combustion zone, was calculated. This method can be applied to large-sized pre-chamber combustors in which the acoustic characteristics of the pre-chamber should be excluded, and can be used in dump burners, for which it is difficult to directly measure the velocity fluctuation in the combustion zone. The experimental results for the FTF measurements provide a basic insight into the design of the combustion chamber and fuel-air supply line in a gas turbine operation.

CHAPTER 6

CONCLUSION

Combustion characteristics (NO_x, CO and flame structure) is investigated on partially premixed SNG flame adjusting hydrogen ratio to make each fuel composition with same Wobbe index. Nitrogen and carbon dioxide are used as a diluent and supplied into air feed line from 0% to 200% based on amount of fuel mixture. A summary of the findings are as follows.

From the results, we obtained the following conclusions. Main NO_x generation mechanism is thermal NO_x according to the relation with equivalence ratio and heat. CO emission increases sharply at equivalence ratio 1 and OH-radical affects CO-oxidation directly. NO_x reduction is the function of the diluent heat capacity and heat load and dilution of carbon dioxide is more effective than nitrogen, because the heat capacity of carbon dioxide diluent is much larger than that of nitrogen at the same mass flow rate. Flame fluctuation influence dump plane temperature in combustion instability. All of combustion compositions occur outer recirculation zone. Combustion instability should be avoid in order to prevent combustor liner damage.

Emission characteristics, including the relationship between combustion instability mode transition, combustor length, the characteristics of flame shape, and the OH radical concentration of the flame, were analyzed in this study using an experimental study in various test conditions in a model gas turbine combustor. The length of the combustor did not affect eiNO_x emission. The combustion reaction zone, where the fuel and air were mixed and reacted chemically, was relatively shorter than the length of the combustor used in this study. Therefore, the chemical reaction was complete regardless of this length. It was experimentally confirmed that the NO_x mechanism was thermal NO_x (Zeldovich's thermal NO_x mechanism) because higher NO_x emissions were observed when the H₂ ratio of the H₂/CH₄ mixture and the heat load increased, which influenced flame temperature. Moreover, CO emission was less than 3 ppm, as the equivalence ratio varied from 0.4 to 0.6 in all experimental conditions. The frequency of combustion instability

shifted to a higher longitudinal mode with an increase in the H₂ ratio. The fundamental mode of the longitudinal frequency of the combustor occurred for an H₂ ratio 0% in terms of fuel composition, which thus consisted of only CH₄, and the frequency mode shifted up to the seventh longitudinal mode with an increase in H₂ in fuel composition. This was verified by the theoretical formulation. However, the length of the combustor did not influence mode transition; only a slight frequency change was observed at the same frequency mode. The H₂ ratio changed flame length due owing the relative burning velocities of H₂ and CH₄, and the flame length influenced convection time. To support the results, the speed of the laminar flame was calculated, and it was verified that the frequency of combustion instability was proportional to this speed. Flame length decreased with an increase in the H₂ ratio, which was verified using a 7,000 Hz high-speed camera and the Abel inversion process. Using the images of the flame cross-section, the occurrence of combustion instability was confirmed using the OH radical concentration radial profiles of the flame using the strong vibration of the flame on the dump plane.

1-D acoustic modeling of a gas turbine combustor was used to predict the combustion instability, and an enhanced flame transfer function was proposed to improve the prediction accuracy. For this purpose, the cold-flow transfer function, which reflects the acoustic characteristics of the fuel injector with respect to the hydrogen and methane compositions, was defined and measured. In addition, the ratio of FTF to CTF was mathematically calculated to obtain the enhanced flame transfer function, which eliminates the effects of disturbances. The combustion instability frequency according to the hydrogen/methane ratio was predicted using OSCILOS and the mathematically derived eFTF was verified through comparisons with the combustion instability frequency obtained from the experiments.

Combustion experiments for hydrogen/methane compositions and equivalence ratios were performed to investigate the combustion instability characteristics, and the flame length was used to confirm that the convection time delay transfers the combustion instability to higher modes. The FTF was measured to confirm that the gain and phase had different characteristics in the hydrogen flame. To understand the cause of the constructive

characteristics in FTF, the acoustic characteristics of the fuel injector were investigated. The peak frequencies of each transfer functions were determined by the quarter wave resonance in the fuel feeding line. The reflection coefficients of the siren and fuel injector were calculated to determine the acoustic boundary condition, and the resonance effect was validated by measuring the FLTF for various fuel feeding line lengths.

The FTF reflects the dynamic response characteristics of the fuel velocity fluctuation to the flame heat release fluctuation. However, in the case of LDI combustors, where the volume of the fuel feeding line is relatively large, the internal resonance phenomenon affects the FTF. Therefore, resonance should be eliminated from the FTF measurements. The FTF was mathematically defined using FLTF, and it was confirmed that the excitation frequency that produced the peak gain vanished. The mathematical and physical meaning of the slope of $\text{phase}_{\text{FTF}}$ was found to correspond with the time delay.

The combustion instability frequency was estimated from the experimentally obtained ITF and FTF results using the 1-D acoustic solver OSCILOS. The length of the flame and the effective fuel injection area were experimentally calculated, and the flame length was confirmed to be a very important parameter for frequency mode predictions. Furthermore, the combustion instability frequency was found to be underestimated when using $\text{phase}_{\text{ITF}}$ instead of $\text{phase}_{\text{FTF}}$. Thus, combustion instability modeling using FTF is more effective in predicting the combustion instability frequency.

In conclusion, the FLTF in the non-burning state was derived to obtain the eFTF from the ITF and investigate acoustic effects in the pre-chamber. In addition, the response characteristics of the flame under velocity fluctuations in the combustion field were obtained. This method can be applied to large-sized pre-chamber combustors in which the acoustic characteristics of the pre-chamber should be excluded, and can be used in dump burners, for which it is difficult to directly measure the velocity fluctuation in the combustion zone. The experimental results for the FTF measurements provide a basic insight into the design of the combustion chamber and fuel-air supply line in a gas turbine operation.

REFERENCES

- [1] Y. Yan, L. Dang, Y. Deng, J. Li, J. Zhao, Experimental study of flow dynamics and fuel spray characteristics in Lean Premixed Prevaporized Combustor, *Fuel*, 144, (2015), 197–204.
- [2] Y. S. Chati, H. Balakrishnan, Analysis of Aircraft Fuel Burn and Emissions in the Landing and Take Off Cycle using Operational Data, *6th Int. Conf. Res. Air Transp.*, (2014).
- [3] J. Goldmeer, A. Sanz, M. Adhikari, Gas to Power : The Art of the Possible the Fuel Flexibility of GE Power’s Aero-derivative Gas Turbines, (2019).
- [4] K. M. Tacina, C. Chang, Z. J. He, P. Lee, H. C. Mongia, B. K. Dam, A Second Generation Swirl-Venturi Lean Direct Injection Combustion Concept, *50th AIAA/ASME/SAE/ASEE Jt. Propuls. Conf.*, (2014), 2014–3434.
- [5] C.-M. Lee, C. T. Chang, J. T. Herbon, S. K. Kramer, NASA project develops next generation low-emissions combustor technologies, (2013), 1–17.
- [6] J.-S. Oh, M. Kim, P.-W. Heo, J.-S. Lee, Y.-B. Yoon, GE 7FA+e DLN-2.6 gas turbine combustor: Part i operating condition optimization, (2016).
- [7] L. B. Davis, Dry Low NO_x Combustion Systems for Ge Heavy-Duty Gas Turbines, (2015), 1–9.
- [8] A. E. E. Khalil, A. K. Gupta, Fuel flexible distributed combustion for efficient and clean gas turbine engines, *Appl. Energy*, 109, (2013), 267–274.
- [9] F. Nicoud, T. Poinsot, Thermoacoustic instabilities: Should the Rayleigh criterion be extended to include entropy changes?, *Combust. Flame*, 142, (2005), 153–159.
- [10] H. A. El-Asrag, A. C. Iannetti, S. V. Apte, Large eddy simulations for radiation-spray coupling for a lean direct injector combustor, *Combust. Flame*, 161, (2), (2014), 510–524.
- [11] R. Balachandran, S. R. Chakravarthy, R. I. Sujith, Characterization of an Acoustically Self-Excited Combustor for Spray Evaporation, *J. Propuls. Power*, 24, (6), (2008), 1382–1389.
- [12] G. Billoud, M. A. Galland, C. H. Huu, S. Candel, Adaptive Active Control of Combustion Instabilities, *Combust. Sci. Technol.*, 81, (4–6), (1992), 257–283.
- [13] S. J. Shanbhogue, Y. S. Sanusi, S. Taamallah, M. A. Habib, E. M. A. Mokheimer, A. F. Ghoniem, Flame macrostructures, combustion instability and extinction strain scaling in swirl-stabilized premixed CH₄/H₂ combustion, *Combust. Flame*, 163, (2016), 494–507.
- [14] F. Boudy, D. Durox, T. Schuller, S. Candel, Nonlinear mode triggering in a multiple

- flame combustor, *Proc. Combust. Inst.*, 33, (1), (2011), 1121–1128.
- [15] J. Yoon, S. Joo, J. Kim, M. C. Lee, J. G. Lee, Y. Yoon, Effects of convection time on the high harmonic combustion instability in a partially premixed combustor, *Proc. Combust. Inst.*, 36, (3), (2017), 3753–3761.
- [16] R. A. J. Müller, J. Hermann, W. Polifke, Stability limits and non-linear characteristics of a self-excited combustion instability, *19th Int. Congr. Sound Vib. 2012, ICSV 2012*, 1, (2012), 514–521.
- [17] S. W. Hester, W. E. Anderson, M. Zoltowski, T. W. Feldman, High Frequency Signal Analysis Methods for Acoustic Modal Onset in a Continuously Varying Resonance Combustor, (2014), 1–11.
- [18] N. Noiray, D. Durox, T. Schuller, S. Candel, A unified framework for nonlinear combustion instability analysis based on the flame describing function, *J. Fluid Mech.*, 615, (2008), 139–167.
- [19] Shreekrishna, S. Hemchandra, T. Lieuwen, Premixed flame response to equivalence ratio perturbations, *Combust. Theory Model.*, 14, (5), (2010), 681–714.
- [20] D. Kim, J. G. Lee, B. D. Quay, D. A. Santavicca, K. Kim, S. Srinivasan, Effect of Flame Structure on the Flame Transfer Function in a Premixed Gas Turbine Combustor, *J. Eng. Gas Turbines Power*, 132, (2), (2010), 021502.
- [21] S. Candel, D. Durox, T. Schuller, J.-F. Bourgoquin, J. P. Moeck, Dynamics of Swirling Flames, *Annu. Rev. Fluid Mech.*, 46, (1), (2013), 147–173.
- [22] K. T. Kim, S. Hochgreb, Measurements of triggering and transient growth in a model lean-premixed gas turbine combustor, *Combust. Flame*, 159, (3), (2012), 1215–1227.
- [23] C. M. Coats, Z. Chang, P. D. Williams, Excitation of thermoacoustic oscillations by small premixed flames, *Combust. Flame*, 157, (6), (2010), 1037–1051.
- [24] P. Palies, D. Durox, T. Schuller, S. Candel, Nonlinear combustion instability analysis based on the flame describing function applied to turbulent premixed swirling flames, *Combust. Flame*, 158, (10), (2011), 1980–1991.
- [25] K. S. Kedia, A. F. Ghoniem, An analytical model for the prediction of the dynamic response of premixed flames stabilized on a heat-conducting perforated plate, *Proc. Combust. Inst.*, 34, (1), (2013), 921–928.
- [26] B. Schuermans, F. Gueithe, W. Mohr, Optical Transfer Function Measurements for Technically Premixed Flames, *J. Eng. Gas Turbines Power*, 132, (8), (2010), 081501.
- [27] L. Tay-Wo-Chong, W. Polifke, Large Eddy Simulation-Based Study of the Influence of Thermal Boundary Condition and Combustor Confinement on Premix Flame Transfer Functions, *J. Eng. Gas Turbines Power*, 135, (2), (2013), 021502.

- [28] K. T. Kim, J. G. Lee, H. J. Lee, B. D. Quay, D. A. Santavicca, Characterization of Forced Flame Response of Swirl-Stabilized Turbulent Lean-Premixed Flames in a Gas Turbine Combustor, *J. Eng. Gas Turbines Power*, 132, (4), (2010), 041502.
- [29] T. Yi, D. A. Santavicca, Flame Transfer Functions for Liquid-Fueled Swirl-Stabilized Turbulent Lean Direct Fuel Injection Combustion, *J. Eng. Gas Turbines Power*, 132, (2), (2010), 1–6.
- [30] K. T. Kim, D. Santavicca, Linear stability analysis of acoustically driven pressure oscillations in a lean premixed gas turbine combustor, *J. Mech. Sci. Technol.*, 23, (12), (2010), 3436–3447.
- [31] K. T. Kim, J. G. Lee, B. D. Quay, D. A. Santavicca, Spatially distributed flame transfer functions for predicting combustion dynamics in lean premixed gas turbine combustors, *Combust. Flame*, 157, (9), (2010), 1718–1730.
- [32] S. M. R. Hosseini, C. Gardner, C. Lawn, The non-linear thermo-acoustic response of a small swirl burner, *Combust. Flame*, 159, (5), (2012), 1909–1920.
- [33] A. K. Dhakiya, B. K. Shah, A. S. Mohite, Study of flow through combustion swirler with the effect of diffuser on the recirculation zone, 3, (6), (2012), 68–73.
- [34] J. M. Seitzman, A. Üngüt, P. H. Paul, R. K. Hanson, Imaging and characterization of OH structures in a turbulent nonpremixed flame, *Symp. Combust.*, 23, (1), (1991), 637–644.
- [35] M. Stöhr, C. M. Arndt, W. Meier, Effects of Damköhler number on vortex-flame interaction in a gas turbine model combustor, *Proc. Combust. Inst.*, 34, (2), (2013), 3107–3115.
- [36] M. Stöhr, I. Boxx, C. Carter, W. Meier, Dynamics of lean blowout of a swirl-stabilized flame in a gas turbine model combustor, *Proc. Combust. Inst.*, 33, (2), (2011), 2953–2960.
- [37] I. Boxx, M. Stöhr, C. Carter, W. Meier, Temporally resolved planar measurements of transient phenomena in a partially pre-mixed swirl flame in a gas turbine model combustor, *Combust. Flame*, 157, (8), (2010), 1510–1525.
- [38] P. Petersson *et al.*, Simultaneous high-speed PIV and OH PLIF measurements and modal analysis for investigating flame-flow interaction in a low swirl flame, *16th Int Symp Appl. Laser Tech. to Fluid Mech.*, (2012), 9–12.
- [39] J. R. Dawson, R. L. Gordon, J. Kariuki, E. Mastorakos, A. R. Masri, M. Juddoo, Visualization of blow-off events in bluff-body stabilized turbulent premixed flames, *Proc. Combust. Inst.*, 33, (1), (2011), 1559–1566.
- [40] N. A. Worth, J. R. Dawson, Cinematographic OH-PLIF measurements of two interacting turbulent premixed flames with and without acoustic forcing, *Combust. Flame*, 159, (3), (2012), 1109–1126.

- [41] S. Hammack, S. Kostka, A. Lynch, C. Carter, T. Lee, Simultaneous 10-kHz PLIF and chemiluminescence imaging of OH radicals in a microwave plasma-enhanced flame, *IEEE Trans. Plasma Sci.*, 41, (12), (2013), 3279–3286.
- [42] P. M. Allison, Y. Chen, M. Ihme, J. F. Driscoll, Coupling of flame geometry and combustion instabilities based on kilohertz formaldehyde PLIF measurements, *Proc. Combust. Inst.*, 35, (3), (2015), 3255–3262.
- [43] S. Meares, V. N. Prasad, M. Juddoo, K. H. Luo, A. R. Masri, Simultaneous planar and volume cross-LIF imaging to identify out-of-plane motion, *Proc. Combust. Inst.*, 35, (3), (2015), 3813–3820.
- [44] C. O. Paschereit, B. Schuermans, W. Polifke, O. Mattson, Measurement of Transfer Matrices and Source Terms of Premixed Flames, *J. Eng. Gas Turbines Power*, 124, (2), (2002), 239.
- [45] A. X. Sengissen, J. F. Van Kampen, R. A. Huls, G. G. M. Stoffels, J. B. W. Kok, T. J. Poinsot, LES and experimental studies of cold and reacting flow in a swirled partially premixed burner with and without fuel modulation, *Combust. Flame*, 150, (1–2), (2007), 40–53.
- [46] K. P. Geigle *et al.*, Phase-Resolved Laser Diagnostic Measurements of a Downscaled, Fuel-Staged Gas Turbine Combustor at Elevated Pressure and Comparison to LES Predictions, *J. Eng. Gas Turbines Power*, 129, (3), (2007), 680.
- [47] W. S. Cheung *et al.*, Measurement and Analysis of Flame Transfer Function in a Sector Combustor Under High Pressure Conditions, (2009), 187–194.
- [48] X. Han, J. Li, A. S. Morgans, Prediction of combustion instability limit cycle oscillations by combining flame describing function simulations with a thermoacoustic network model, *Combust. Flame*, 162, (10), (2015), 3632–3647.
- [49] L. Selle *et al.*, Compressible large eddy simulation of turbulent combustion in complex geometry on unstructured meshes, *Combust. Flame*, 137, (4), (2004), 489–505.
- [50] J. Li, A. S. Morgans, Time domain simulations of nonlinear thermoacoustic behaviour in a simple combustor using a wave-based approach, *J. Sound Vib.*, 346, (1), (2015), 345–360.
- [51] C. F. Silva, F. Nicoud, T. Schuller, D. Durox, S. Candel, Combining a Helmholtz solver with the flame describing function to assess combustion instability in a premixed swirled combustor, *Combust. Flame*, 160, (9), (2013), 1743–1754.
- [52] C. Keeler, T. Lynch, POSCO Gwangyang Project for Substitute Natural Gas (SNG), *Gasif. Technol. Conf.*, (2010), 12.
- [53] T. ASAI, S. DODO, M. KARISHUKU, N. YAGI, Y. AKIYAMA, A. HAYASHI, Multiple-injection dry low-NO_x combustor for hydrogen-rich syngas fuel: testing

- and evaluation of performance in an IGCC pilot plant, *Mech. Eng. J.*, 1, (5), (2014).
- [54] S. Park, U. Kim, M. Lee, S. Kim, D. Cha, The effects and characteristics of hydrogen in SNG on gas turbine combustion using a diffusion type combustor, *Int. J. Hydrogen Energy*, 38, (29), (2013), 12847–12855.
- [55] S. Göke *et al.*, Influence of steam dilution on the combustion of natural gas and hydrogen in premixed and rich-quench-lean combustors, *Fuel Process. Technol.*, 107, (x), (2013), 14–22.
- [56] V. Ponc, Some Aspects of the Mechanism of Methanation and Fischer-Tropsch Synthesis, *Catal. Rev.*, 18, (1), (1978), 151–171.
- [57] M. C. Lee, S. Bin Seo, J. Yoon, M. Kim, Y. Yoon, Experimental study on the effect of N₂, CO₂, and steam dilution on the combustion performance of H₂ and CO synthetic gas in an industrial gas turbine, *Fuel*, 102, (2012), 431–438.
- [58] J. Yoon, M. K. Kim, J. Hwang, J. Lee, Y. Yoon, Effect of fuel-air mixture velocity on combustion instability of a model gas turbine combustor, *Appl. Therm. Eng.*, 54, (1), (2013), 92–101.
- [59] J. Lin *et al.*, Remarkable effects of hydroxyl species on low-temperature CO (preferential) oxidation over Ir/Fe(OH)_x catalyst, *J. Catal.*, 319, (2014), 142–149.
- [60] S. Joo, J. Yoon, J. Kim, M. Lee, Y. Yoon, NO_x emissions characteristics of the partially premixed combustion of H₂/CO/CH₄ syngas using artificial neural networks, *Appl. Therm. Eng.*, 80, (x), (2015), 436–444.
- [61] J. Liu, D. Cui, C. Yao, J. Yu, F. Su, G. Xu, Syngas methanation in fluidized bed for an advanced two-stage process of SNG production, *Fuel Process. Technol.*, 141, (2016), 130–137.
- [62] C. R. Vitasari, M. Jurascik, K. J. Ptasiński, Exergy analysis of biomass-to-synthetic natural gas (SNG) process via indirect gasification of various biomass feedstock, *Energy*, 36, (6), (2011), 3825–3837.
- [63] S. T. Omaye, Metabolic modulation of carbon monoxide toxicity, *Toxicology*, 180, (2), (2002), 139–150.
- [64] R. K. Cheng, D. Littlejohn, P. A. Strakey, T. Sidwell, Laboratory investigations of a low-swirl injector with H₂ and CH₄ at gas turbine conditions, *Proc. Combust. Inst.*, 32, (2), (2009), 3001–3009.
- [65] Coppens F.H.V., J. De Ruyck, A. A. Konnov, The effects of composition on burning velocity and nitric oxide formation in laminar premixed flames of CH₄+H₂+O₂+N₂, *Combust. Flame*, 149, (4), (2007), 409–417.
- [66] G. J. Bloxsidge, A. P. Dowling, P. J. Langhorne, Reheat buzz: an acoustically coupled combustion instability. Part 2. Theory, *J. Fluid Mech.*, 193, (1), (1988), 445.

- [67] P. J. Langhorne, Reheat buzz: an acoustically coupled combustion instability. Part 1. Experiment, *J. Fluid Mech.*, 193, (1), (1988), 417.
- [68] L. Figura, J. G. Lee, B. D. Quay, D. A. Santavicca, The Effects of Fuel Composition on Flame Structure and Combustion Dynamics in a Lean Premixed Combustor, in *Volume 2: Turbo Expo 2007*, 2007, 2, 181–187.
- [69] M. C. Lee, J. Yoon, S. Joo, J. Kim, J. Hwang, Y. Yoon, Investigation into the cause of high multi-mode combustion instability of H₂/CO/CH₄ syngas in a partially premixed gas turbine model combustor, *Proc. Combust. Inst.*, 35, (3), (2015), 3263–3271.
- [70] T. García-Armingol, J. Ballester, A. Smolarz, Chemiluminescence-based sensing of flame stoichiometry: Influence of the measurement method, *Measurement*, 46, (9), (2013), 3084–3097.
- [71] V. K. Arghode, A. K. Gupta, Hydrogen addition effects on methane–air colorless distributed combustion flames, *Int. J. Hydrogen Energy*, 36, (10), (2011), 6292–6302.
- [72] F. R. J. Spearman, The Derivation and Use of Aerodynamic Transfer Functions of Airframes, *J. R. Aeronaut. Soc.*, 59, (539), (1955), 743–761.
- [73] A. Osharov, B. Natan, Combustion instability in a small liquid rocket motor, *Aeronaut. J.*, 103, (1023), (1999), 245–252.
- [74] P. D. McCormack, A Driving Mechanism for High Frequency Combustion Instability in Liquid Fuel Rocket Engines, *J. R. Aeronaut. Soc.*, 68, (645), (1964), 633–637.
- [75] Y. W. YAN, Y. P. Liu, Y. C. Liu, J. H. Li, Experimental and computational investigations of flow dynamics in LPP combustor, *Aeronaut. J.*, 121, (1240), (2017), 790–802.
- [76] Y. Karagöz, İ. Güler, T. Sandalcı, L. Yüksek, A. S. Dalkılıç, S. Wongwises, Effects of hydrogen and methane addition on combustion characteristics, emissions, and performance of a CI engine, *Int. J. Hydrogen Energy*, 41, (2), (2016), 1313–1325.
- [77] E. Ahmed, Y. Huang, Flame volume prediction and validation for lean blow-out of gas turbine combustor, *Aeronaut. J.*, 121, (1236), (2017), 237–262.
- [78] S. Daniele, P. Jansohn, J. Mantzaras, K. Boulouchos, Turbulent flame speed for syngas at gas turbine relevant conditions, *Proc. Combust. Inst.*, 33, (2), (2011), 2937–2944.
- [79] J. Ströhle, T. Myhrvold, An evaluation of detailed reaction mechanisms for hydrogen combustion under gas turbine conditions, *Int. J. Hydrogen Energy*, 32, (1), (2007), 125–135.
- [80] V. Theofilis, D. Barkley, S. Sherwin, Spectral/HP element technology for global

- flow instability and control, *Aeronaut. J.*, 106, (2002), 619–625.
- [81] R. Hayes, R. Dwight, S. Marques, Reducing parametric uncertainty in limit-cycle oscillation computational models, *Aeronaut. J.*, 121, (1241), (2017), 940–969.
- [82] Z. Saboohi, F. Ommi, Emission prediction in conceptual design of the aircraft engines using augmented CRN, *Aeronaut. J.*, 121, (1241), (2017), 1005–1028.
- [83] M. Aliyu, M. A. Nemitallah, S. A. Said, M. A. Habib, Characteristics of H₂-enriched CH₄-O₂ diffusion flames in a swirl-stabilized gas turbine combustor: Experimental and numerical study, *Int. J. Hydrogen Energy*, 41, (44), (2016), 20418–20432.
- [84] District South Coast Air Quality Management, Source Test Protocol for Determining Oxygen Corrected Pollutant Concentrations from Combustion Sources with High Stack Oxygen Content, (2011).
- [85] E. W. Hansen, P.-L. Law, Recursive methods for computing the Abel transform and its inverse, *J. Opt. Soc. Am. A*, 2, (4), (1985), 510.
- [86] S. Naha, S. K. Aggarwal, Fuel effects on NO_x emissions in partially premixed flames, *Combust. Flame*, 139, (1–2), (2004), 90–105.
- [87] T. C. Lieuwen, Experimental Investigation of Limit-Cycle Oscillations in an Unstable Gas Turbine Combustor, *J. Propuls. Power*, 18, (1), (2002), 61–67.
- [88] T. Lieuwen, Investigation of combustion instability mechanisms in premixed gas turbines, *Ph.D. Thesis*, (2014).
- [89] J. Yoon, S. Joo, J. Kim, M. C. Lee, J. G. Lee, Y. Yoon, Effects of convection time on the high harmonic combustion instability in a partially premixed combustor, *Proc. Combust. Inst.*, 36, (3), (2017), 3753–3761.
- [90] F. Nicoud, T. Poinsot, Thermoacoustic instabilities: should the Rayleigh criterion be extended to include entropy changes?, *Proceeding Combust. Inst.*, 142, (2005), 153–159.
- [91] J. Park, M. C. Lee, Combustion instability characteristics of H₂/CO/CH₄ syngases and synthetic natural gases in a partially-premixed gas turbine combustor: Part I—Frequency and mode analysis, *Int. J. Hydrogen Energy*, 41, (18), (2016), 7484–7493.
- [92] J. Manton, G. von Elbe, B. Lewis, Nonisotropic Propagation of Combustion Waves in Explosive Gas Mixtures and the Development of Cellular Flames, *J. Chem. Phys.*, 20, (1), (1952), 153–157.
- [93] A. E. E. Khalil, A. K. Gupta, Fuel flexible distributed combustion for efficient and clean gas turbine engines, *Appl. Energy*, 109, (2013), 267–274.
- [94] M. Fiore, A. Viggiano, E. Fanelli, G. Braccio, V. Magi, Influence of piston shape

- and injector geometry on combustion and emission characteristics of syngas in direct-injection spark-ignition engine, *Energy Procedia*, 148, (2018), 392–399.
- [95] N. Patel, M. Kirtaş, V. Sankaran, S. Menon, Simulation of spray combustion in a lean-direct injection combustor, *Proc. Combust. Inst.*, 31 II, (2007), 2327–2334.
- [96] D. Dewanji, A. G. Rao, M. Pourquoi, J. . Van Buijitenen, Investigation of Flow Characteristics in Lean Direct Injection Combustors, *J. Propuls. Power*, 28, (1), (2012), 181–196.
- [97] S. Gersen, H. Darneveil, H. Levinsky, The effects of CO addition on the autoignition of H₂, CH₄ and CH₄/H₂ fuels at high pressure in an RCM, *Combust. Flame*, 159, (12), (2012), 3472–3475.
- [98] T. Komarek, W. Polifke, Impact of Swirl Fluctuations on the Flame Response of a Perfectly Premixed Swirl Burner, *J. Eng. Gas Turbines Power*, 132, (6), (2010), 061503-1–7.
- [99] B. A. Imteyaz, M. A. Nemitallah, A. A. Abdelhafez, M. A. Habib, Combustion behavior and stability map of hydrogen-enriched oxy-methane premixed flames in a model gas turbine combustor, *Int. J. Hydrogen Energy*, 43, (34), (2018), 16652–16666.
- [100] T. P. D. Mejia, . M. M. Brebion, A. Ghani, T. Kaiser, F. Duchaine, L. Selle, Influence of flame-holder temperature on the acoustic flame transfer functions of a laminar flame, *Combust. Flame*, 188, (2018), 5–12.
- [101] A. Albayrak, R. S. Blumenthal, A. Ulhaq, W. Polifke, An analytical model for the impulse response of laminar premixed flames to equivalence ratio perturbations, *Proc. Combust. Inst.*, 36, (3), (2017), 3725–3732.
- [102] K. F. Zohra, A. Mounir, C. Salah, Numerical simulation of CH₄-H₂-AIR non-premixed flame stabilized by a bluff body, *Energy Procedia*, 139, (2017), 530–536.
- [103] L. Ziani, A. Chaker, Ambient pressure effect on non-premixed turbulent combustion of CH₄-H₂ mixture, *Int. J. Hydrogen Energy*, 41, (27), (2016), 11842–11847.
- [104] X. Yu, Y. Du, P. Sun, L. Liu, H. Wu, X. Zuo, Effects of hydrogen direct injection strategy on characteristics of lean-burn hydrogen-gasoline engines, *Fuel*, 208, (2017), 602–611.
- [105] D. A. Lacoste, Y. Xiong, J. P. Moeck, S. H. Chung, W. L. Roberts, M. S. Cha, Transfer functions of laminar premixed flames subjected to forcing by acoustic waves, AC electric fields, and non-thermal plasma discharges, *Proc. Combust. Inst.*, 36, (3), (2017), 4183–4192.
- [106] X. Han, A. S. Morgans, Simulation of the flame describing function of a turbulent premixed flame using an open-source LES solver, *Combust. Flame*, 162, (5), (2015),

1778–1792.

- [107] T. Lieuwen, Modeling Premixed Combustion-Acoustic Wave Interactions: A Review, *J. Propuls. power*, 19, (5), (2003).
- [108] K. M. Holmgren, T. S. Berntsson, E. Andersson, T. Rydberg, The influence of biomass supply chains and by-products on the greenhouse gas emissions from gasification-based bio-SNG production systems, *Energy*, 90, (2014), 1–15.
- [109] R. Gaudron, M. Gatti, C. Mirat, T. Schuller, Impact of the injector size on the transfer functions of premixed laminar conical flames, *Combust. Flame*, 179, (2017), 138–153.
- [110] Y. Afarin, S. Tabejamaat, The effect of fuel inlet turbulence intensity on H₂/CH₄ flame structure of MILD combustion using the LES method, *Combust. Theory Model.*, 17, (3), (2013), 383–410.
- [111] M. Haeringer, M. Merk, W. Polifke, Inclusion of higher harmonics in the flame describing function for predicting limit cycles of self-excited combustion instabilities, *Proc. Combust. Inst.*, (2018), 1–8.
- [112] H. Yu, P. Zhu, J. Suo, L. Zheng, Investigation of Discharge Coefficients for Single Element Lean Direct Injection Modules, *Energies*, 11, (6), (2018).

초 록

에너지 생산량의 증가와 지속적으로 상승하는 배기배출물 규제치에 따라 산업용 및 항공용 가스터빈 연소기에 대한 다각화된 연구가 진행되어오고 있다. 산업용 가스터빈의 경우 화석연료를 대체하기 위하여 기체연료를 이용한 에너지 생산 방법이 활용되고 있으며, 항공용 가스터빈은 연소 효율을 극대화시키기 위한 노력들이 필요하다. 이러한 노력의 일환으로 GE에서는 다양한 연료가 활용 가능한 고성능 가스터빈 개발에 앞장서고 있으며, 연소기 내부의 형태 및 노즐의 다각화를 통하여 연료효율을 높이고자하고 있다. 또한 지멘스는 RDS(Remote Diagnostics Service) 및 최적화 프로세스를 통하여 자체적으로 발생하는 배기배출물 및 연소 불안정에 대한 빅데이터를 이용하여 연소효율을 최적화시키기 위한 연구가 진행되고 있다. 대기환경 측면에서는 국제민간항공기구(ICAO; International Civil Aviation Organization)의 환경규제위원회(CAEP; Committee on Aviation Environmental Protection) 에서 NO_x, CO 등의 주요 대기오염물질에 대한 규제(CAEP/2, CAEP/6 등)을 매년 새롭게 제정하고 적극적으로 적용하고 있다. 최근에는 중소형급 민간항공기 엔진에 대하여 CAEP/8 규제를 시행하였다. 즉, 대기환경 규제를 만족하기 위해서는 연소시스템에 대한 전반적인 기술이 반드시 수반되어야 함을 역설한다. 항공용 가스터빈 엔진의 경우 무게 및 공간에 대한 제약이 많아 대기환경 오염물질에 대한 촉매장치 등의 추가 장치를 설치하기가 매우 어려운 실정이다. 즉 대기오염물질에 대한 저감을 위해서는 제한된 코어엔진 내에서의 친환경 연소기술이 반드시 필요하다. 기본적으로 NO_x 등의 대기환경을 저감하기 위해서는 연소장내에서의 온도가 낮은 상태에서 연소가 이루어져야 하는데, 이를 위해서는 연료-공기의 상대적인 비율인 당량비가 낮은 상태(fuel lean)에서 연소 환경이 이루어져야 한다. 또한 연소장 내에서의 균일한 온도분포가 이루어져야 하기 때문에 일반적으로 확산화염보다 예혼합 화염에서 연소 환경이 형성된다. 하지만 낮은 당량비와 연료와 산화제가 연소기 이전에 섞이는 예혼합 연소기에서는 화염 역화 연상이나 연소불안정과 같은 매우 취약한 형태의 연소가 이루어지기 때문에 이를 제어하기 위한 연구가 활발하게 이루어지고 있다.

연소불안정은 연소장에서의 압력섭동과 동압섭동의 간섭 때문에 일어나는 현상으로 강한 화염의 떨림과 강한 동압섭동이 발생하여, 연소불안정이 강하게 발생하는 경우 연소기 라이너의 소손으로 직결되는 중요한 문제이다. 그렇기 때문에 이러한 연소불안정이 발생하는 연소환경에 대한 예측 및 연소불안정이 발생하였을 때, 이를 저감하는 연구 또한 많은 연구진들에 의하여 진행되고 있다.

화염 전달함수는 가스터빈 연소기라는 블랙박스에 입력 값과 출력 값에 대한 전달함수로 정의가 되며 입력 값은 연료나 공기의 섭동 값(u'), 출력 값은 화염의 섭동(q')으로 계측할 수 있다. 화염 전달함수는 복소수 형태로 표현이 되는데 복소수에서의 실수부는 입력 값이 출력 값에 미치는 증폭 값(gain)을 의미하며 허수부는 시간지연(phase)를 의미한다. 이러한 화염 전달함수는 연소불안정을 예측하는 코드의 입력 값으로 사용이 되며 연소기의 특성을 파악할 수 있는 계측 값으로 활용된다.

본 연구에서는 연소 불안정이 발생하는 연소장치에서의 다양한 연료조성에 대한 연소불안정의 특성과 정적 특성에 대한 연구를 수행하였다. 또한 배기배출물에 대한 특성을 파악하였으며, 비활성기체를 이용한 배기배출물 저감 특성에 대한 연구를 수행하였다. 마지막으로 연소불안정 연구의 일환인 화염전달함수를 계측하고 화염전달함수에서 나타나는 물리적인 특성을 파악하였으며, 연료의 섭동이 아닌 외부 영향에 대한 간섭을 효과적으로 제외한 화염전달함수의 계측 및 계산방법을 제시하였으며, 이렇게 도출해낸 화염전달함수를 이용하여 연소불안정을 모델링하여 실제 발생하는 연소불안정 주파수와 비교하는 연구를 수행하였다.

희석제로 사용되는 질소와 이산화탄소에 대한 NO_x 배출량에 대한 희석 특성을 파악하였다. 저부하에서 고부하까지의 SNG 합성가스에 대한 NO_x 배출특성을 우선 파악하였고, 질소보다 이산화탄소 희석제에 대한 질소산화물 저감에 영향이 더 뚜렷하다는 것을 확인할 수 있다. 이는 투입용량과 비열로 표현되는 열용량의 차이 때문에 발생하는 것으로, 큰 희석제는 연료가 연소될 때 발생하는 열을 흡수할 수 있는 용량이 큼을 의미한다. 단위 몰당 비열이 질소보다 이산화탄소가 더욱 크기 때문에 같은 양의 희석제라 할지라도 화염의 온도를 낮추어주는데 상대적으로 큰 저감 역할을 한다는 것을 파악할 수 있었다.

수소 메탄으로 이루어진 혼합가스의 연소불안정은 수소의 비율이 증가함에 따라

연소기 길이방향에 대한 연소불안정 주파수 값이 커지는 특성을 보인다. 이는 화염의 길이의 특성으로 원인을 파악할 수 있는데, 수소의 비율이 커질수록 화염의 길이 길이가 짧아지고, 짧아진 화염이 화염중심부터 연소기 노즐까지의 연소 전달지연시간을 짧게 만듦으로 연소불안정에 대한 주파수 값을 크게 만드는 역할을 한다. 또한 입열량이 커질수록 연소불안정 주파수가 커지지만 다른 영역대로의 천이가 아닌 같은 영역대에서의 크기가 커지는 것을 확인할 수 있었다. 화염의 종류 화염 전파속도를 계산하여 화염의 길이와 화염전파속도, 그리고 수소비율에 따른 연소불안정의 특성을 실험적으로 확인하였다. 연소불안정이 발생한 화염과 안정적으로 노즐에 붙어있는 화염의 차이점을 파악하여 연소불안정이 발생했을 때의 화염의 떨림 정도를 정량적으로 계산하여 연소불안정이 발생하였을 때 화염의 분포를 척도로 구분할 수 있는 방법을 제시하였다.

마지막으로 연소불안정이 많이 발생하는 수소, 메탄화염의 세가지 경우에 대하여 화염전달함수를 계측하였다. 일반적으로 사용되는 화염전달함수의 계산식을 이용하여 연소기 노즐에서의 속도섭동과 연소장에서의 화염떨림 섭동량을 이용하여 계산을 수행하였고, 연료의 비율에 따라 서로 다른 피크값을 갖는 것을 확인하였다. 이에 대한 원인을 파악하기 위하여 연료라인에서의 전달함수를 구하여 연료공급라인에서의 음향섭동이 화염전달함수에 영향을 미치고 있음을 파악하였다. 실제 화염전달함수는 속도섭동에 대한 화염의 응답특성만을 확인하는 방법이기 때문에 이러한 연료라인에서의 음향섭동을 배제하기 위하여 화염전달함수를 정확하게 구하는 방법을 제시하였으며, 이렇게 구한 화염전달함수가 현재까지 연구되어왔던 화염전달함수의 특성과 비교하는 연구를 수행하였다. 또한 새로운 방법으로 도출된 화염전달함수와 이전의 방법으로 구한 화염전달함수를 비교하기 위하여 연소불안정 모델링을 수행하였고, 새롭게 제시된 방법으로부터 획득한 화염전달함수가 더 높은 정확도를 갖는 것을 확인하였다. 또한 화염전달함수에서 나타나는 화염의 강한 떨림이 연료공급라인에서 발생하는 불안정주파수 및 모드에 기인함을 고속 OH-PLIF 시스템을 이용하여 검증하는 연구를 함께 수행하였다.

상기 연구를 통하여 LDI 연소기에서 다양한 연료조건에 대한 연소불안정 특성을 파악하였으며, 연소불안정이 특성조건에서 높은 주파수로 천이하는 특성을 확인할 수

있었다. 또한 연소불안정을 예측하기 위한 모델링을 수행하였으며, 이를 위하여 정확도 높은 화염전달함수 계측을 함께 수행하였다. 본 논문에서 제시하는 화염전달함수 계측 방법을 이용하여 실제 연소장 전단에서 발생하는 외란에 독립적으로 작동되는 화염전달함수를 구할 수 있으며, 이러한 연구결과는 실제 가스터빈에서 발생하는 연소불안정과 화염전달함수를 계측하는 선행연구자료로 활용될 수 있을 것으로 기대 된다.

중심어: 직접분사 연소기, 연소불안정, 연료 다양성, 고주파 열-음향 불안정, 불안정 모드 천이, 질소산화물, EINO_x, 화염전달함수, OH-PLIF, PIV, 연소불안정 예측, 오실로스 (OSCILOS)

학 번: 2014-30362